FROM THE SUBGLACIAL ENVIRONMENT TO THE COASTAL OCEAN: EXPLORING FEEDBACKS BETWEEN GLACIAL MELTWATER AND TIDEWATER GLACIER DYNAMICS.

by

ALEXANDER O. HAGER

A DISSERTATION

Presented to the Department of Earth Sciences
and the Division of Graduate Studies of the University of Oregon
in partial fulfillment of the requirements
for the degree of
Doctor of Philosophy

December 2022

DISSERTATION APPROVAL PAGE

Student: Alexander O. Hager

Title: From the Subglacial Environment to the Coastal Ocean: Exploring Feedbacks Between Glacial Meltwater and Tidewater Glacier Dynamics.

This dissertation has been accepted and approved in partial fulfillment of the requirements for the Doctor of Philosophy degree in the Department of Earth Sciences by:

Alan Rempel	Chair
David Sutherland	Core Member
Jonathan Nash	Core Member
Josef Dufek	Core Member
Mark Carey	Institutional Representative

and

Krista Chronister	Vice Provost for Graduate Studies

Original approval signatures are on file with the University of Oregon Division of Graduate Studies.

Degree awarded December 2022

DISSERTATION ABSTRACT

Alexander O. Hager

Doctor of Philosophy

Department of Earth Sciences

December 2022

Title: From the Subglacial Environment to the Coastal Ocean: Exploring Feedbacks Between Glacial Meltwater and Tidewater Glacier Dynamics.

Mass loss from the Antarctic and Greenland ice sheets has accelerated in recent decades and is predicted to contribute < 40 cm of mean sea level rise in the 21st Century. However, there is significant uncertainty in projections of ice sheet mass balance arising from unknowns in the dynamic response of tidewater glaciers to ocean forcing. At both the ice-ocean and ice-bed boundaries, glacial meltwater plays a vital role in governing the dynamics of tidewater glaciers, yet many meltwater processes are difficult to observe and are subsequently parameterized with unvalidated approximations in ice sheet models. Here, I employ a suite of numerical modeling experiments and observations to investigate how glacial meltwater at the bed and in the ocean affects the susceptibility of tidewater glaciers in Antarctica, Alaska, and Greenland to enhanced ocean forcing.

It has historically been assumed that the formation of channelized subglacial drainage beneath Antarctic ice sheets is not possible, leading to the use of simplifying parameterizations of subglacial drainage under Antarctic ice sheets. However, recent observations have suggested subglacial channels exist beneath some Antarctic tidewater glaciers and could have a substantial impact on ice shelf ablation and glacier dynamics. In Chapter II, I pair numerical modeling

experiments with observed radar specularity content from Thwaites Glacier, West Antarctica, to demonstrate that enough basal meltwater exists to form subglacial channels, which increase frontal ablation and basal friction beneath Thwaites Glacier.

In Chapter III and IV, I transition to investigating the impact of glacial meltwater on glacial fjord dynamics. Leveraging numerical modeling with hydrographic observations from LeConte Bay, Alaska, I show that the sill-driven mixing and buoyancy forcing of subglacial discharge drives strong seasonal circulation regimes in LeConte Bay and may impede ice sheet models from accurately parameterizing ocean thermal forcing of tidewater glaciers. I then run further modeling experiments to test the accuracy ocean thermal forcing parameterizations in Greenland ice sheet models. By identifying the dominant local controls on local water transformation, I develop simple improvements to existing thermal forcing parameterizations that decrease parameterization error by $< 89\%$.

This dissertation includes previously published and co-authored material.

ACKNOWLEDGEMENTS

I would first like to thank my advisor, Dave Sutherland, who has been an incredibly supportive mentor and has provided me with the resources and critical guidance needed to succeed at my PhD, as well as the freedom to pursue my interests. I would also like to thank Matt Hoffman, who served as my mentor at Los Alamos National Laboratory, and whose support and guidance led to my second chapter. Matt was instrumental in securing funding for me while working with Los Alamos and his enthusiasm for his work made our collaboration very rewarding. I am also quite thankful for the encouragement and contributions of my collaborators, particularly Becca Jackson, who gave me my first lesson in oceanography and provided invaluable direction on my third chapter. I am very grateful for guidance and feedback of each of my committee members, Alan Rempel, Mark Carey, Jonathan Nash, and Joe Dufek, some of whom have served on my committee throughout my entire PhD. A special thanks to the members of the Ocean and Ice Lab, past and present, for their help, friendship, and conversation.

Most importantly, I would like to thank my parents, Drevis and Linda, brother, Kurt, sister-in-law, Sheila, grandma, Donna, and fiancée, Sarah Ruth, for their unwavering love, support, and encouragement throughout my PhD. I am confident this dissertation would not have happened without them.

Finally, I would like to acknowledge the Friday Harbor Laboratories Estuarine and Coastal Fluid Dynamics course and the McCarthy International Glaciology Summer School, who provided the educational foundation and inspiration for my entire dissertation. Funding for this work came from the National Science Foundation and the Department of Energy.

TABLE OF CONTENTS

LIST OF FIGURES

Figure Page

Figure Page

LIST OF TABLES

Table Page

CHAPTER I

INTRODUCTION

Mass loss from the Antarctic and Greenland ice sheets has accelerated in recent decades (e.g., Bevis et al., 2019; Harig and Simons, 2015; Rignot et al., 2011; Seo et al., 2015; Velicogna et al., 2014) and is predicted to contribute up to 40 cm of mean sea level rise in the 21st Century (Goelzer et al., 2020; Seroussi et al., 2020). In Antarctica, mass loss results from warmer ocean temperatures enhancing the submarine melting of ice shelves and tidewater glacier termini, while in Greenland, mass loss is the product of both increased ocean and atmospheric warming (Slater and Straneo, 2022; Smith et al., 2020). However, there is significant uncertainty in projections of ice sheet mass balance stemming from unknowns in the dynamic response of ice sheets to ocean forcing, as well as simplifying parameterizations of critical small-scale processes (e.g., Goelzer et al., 2020; Seroussi et al., 2020). For example, subglacial hydrology has long been known as a primary control on glacier dynamics due to its influence on basal sliding (e.g., Iken and Bindschadler, 1986; Kamb, 1987; Kamb et al., 1985); yet, ice sheet models cannot resolve subglacial drainage processes and instead rely on unvalidated assumptions to parameterize subglacial water pressures (e.g., Asay-Davis et al., 2016; Cornford et al., 2020; Leguy et al., 2014; Nias et al., 2018; Yu et al., 2018).

At the ice-ocean boundary, the submarine release of glacial runoff drives turbulent melting of glacier termini (Slater et al., 2015; Xu et al., 2012) and ice shelves (Nakayama et al., 2021; Wei et al., 2020), as well as alters ocean circulation and near-glacier water properties (Carroll et al., 2015, 2017; Jackson and Straneo, 2016; Slater et al., 2018). Submarine melting of icebergs further modifies near-glacier ocean temperatures (Davison et al., 2022,2; Kajanto et al., 2022) and is expected

to reduce the thermal forcing of tidewater glacier termini. Again, such processes are too small-scale to be resolved in ice sheet models and their neglect creates large sources of uncertainty when predicting future sea level rise (Goelzer et al., 2020).

In this dissertation, I track the movement of glacially-sourced meltwater from the subglacial environment to the coastal ocean and determine its influence on ice dynamics and ocean thermal forcing of tidewater glacier termini, with the ultimate goal of understanding how glacial meltwater can impact uncertainty in projected ice sheet dynamics. In Chapter II, I use the MPAS-Albany Land Ice model (MALI) to determine possible configurations of the subglacial drainage network beneath Thwaites Glacier, West Antarctica, which has enough ice to raise global sea level by 65 cm (Rignot et al., 2019) and is currently undergoing unstable retreat catalyzed by enhanced submarine melting of its terminus and ice shelf (Hoffman et al., 2019; Joughin et al., 2014; Milillo et al., 2019; Rignot et al., 2014; Seroussi et al., 2017). Recent observations have suggested basal frictional melting could generate enough meltwater to form widespread subglacial channels beneath Thwaites Glacier (Schroeder et al., 2013), which if true, could augment submarine melting of the terminus and ice shelf, while simultaneously increasing basal drag. However, subglacial channels have historically been thought not to exist in Antarctica and subsequent observations of Thwaites Glacier have put the existence of subglacial channels into doubt Smith et al. (2017). Here, I pair MALI simulations with previously observed remote sensing data to asses the likelihood that subglacial channels exist beneath Thwaites Glacier, and determine their potential influence on glacier stability. I also compare modeled effective pressures in my simulations with those parameterized within ice sheet models. This chapter was

previously published in *The Cryosphere* and was co-authored with Dr. Matthew Hoffman, Dr. Stephen Price, and Dr. Dustin Schroeder.

In Chapter III, I move from the glacier bed to the ocean to investigate the role of subglacial discharge – the sum of subaerial meltwater, basal friction meltwater, and rainfall – in driving seasonal fjord circulation and heat transport in LeConte Bay, a glacial fjord in southeast Alaska. In particular, this chapter focuses on the relationship between turbulent upwelling of subglacial discharge plumes and the mixing of subglacial discharge at bathymetric sills. By pairing numerical modeling experiments using the Massachusetts Institute of Technology general circulation model (MITgcm) with a suite of shipboard and mooring observations collected throughout 2016–2017, I show that seasonal changes in subglacial discharge buoyancy forcing and the sill-driven mixing of glacial freshwater drive substantial seasonal differences in fjord circulation and near-glacier water properties in LeConte Bay. It is expected that similar behavior occurs in silled fjords throughout southeast Alaska, Patagonia, and Greenland. This work was previously published in *The Journal of Geophysical Research: Oceans* with contributions from co-authors Dr. David Sutherland, Dr. Jason Amundson, Dr. Rebecca Jackson, Dr. Christian Kienholz, Dr. Roman Motyka, and Dr. Jonathan Nash.

Chapter IV builds more directly from Chapter III and employs idealized MITgcm experiments to investigate how glacially-sourced meltwater affects near-glacier water properties and quantifies the associated uncertainty in parameterizations of ocean thermal forcing used in Greenland ice sheet models (e.g., Slater et al., 2020). In these experiments, I test how subglacial discharge, glacier submarine meltwater, iceberg submarine meltwater, sill-driven mixing,

and the bathymetric obstruction of offshore water all affect water transformation within glacial fjords. Most ice sheet models do not account for any of these local mechanisms when prescribing ocean thermal forcing at tidewater glacier termini, and instead rely on far-field water properties to drive frontal ablation (Goelzer et al., 2020; Slater et al., 2020). Chapter IV thus assesses the accuracy of such a simplification and presents an updated framework that reduces thermal forcing parameterization uncertainty by up to 90% in our experiments. The updated thermal forcing parameterizations are shown to greatly decrease error in ice sheet model frontal ablation rates. This chapter is intended to inform future generations of ice sheet models and will be submitted to *Geophysical Research Letters* with my advisor, David Sutherland, as a co-author.

CHAPTER II

PERSISTENT, EXTENSIVE CHANNELIZED DRAINAGE MODELED BENEATH THWAITES GLACIER, WEST ANTARCTICA

This chapter was previously published as:

Hager, A. O., Hoffman, M. J., Price, S. F., Schroeder, D. M.(2022). Persistent, extensive channelized drainage modeled beneath Thwaites Glacier, West Antarctica, *The Cryosphere*, 16, 3575-3599, doi: 10.5194/tc-16-3575-2022

Author Contributions: Alexander Hager and Matthew Hoffman conceived of the study and designed the simulation plan. Alexander Hager conducted the model simulations, developed and carried out the analysis, wrote the majority of the manuscript, and created the figures. Matthew Hoffman also assisted with analysis and writing of the paper, designed and implemented the MALI subglacial hydrology model, and created the Thwaites model domain. Stephen Price established funding for the research, provided experience in ice sheet modeling, and gave extensive guidance throughout the research process. Dustin Schroeder contributed his expertise in radar specularity analysis and interpretation, which was critical for comparison with model results. All authors contributed to editing the manuscript and discussing methodology.

2.1 Introduction

Subglacial hydrology is a leading control on basal friction and frontal ablation rates of tidewater glacier termini, yet the morphology of subglacial drainage systems beneath the Antarctic Ice Sheet poorly characterized. Subglacial water can either flow through a highly pressurized, distributed network of bedrock cavities (Kamb, 1987; Walder, 1986), sediment canals (Walder and Fowler, 1994), films (Weertman, 1972), and porous till (Clarke, 1987), or efficiently drain through

arborescent channels melted upward into basal ice (Röthlisberger, 1972). Water flow through a distributed system creates low effective pressures contributing to fast basal sliding (Kamb, 1987; Walder, 1986), whereas channelized drainage increases effective pressures (Hewitt, 2011; Röthlisberger, 1972; Schoof, 2010) and local submarine melt rates at the ice-ocean boundary (Slater et al., 2015). To date, most models of basin or ice sheet-scale Antarctic subglacial drainage have focused on hydropotential mapping (e.g., Carter and Fricker, 2012; Le Brocq et al., 2013; Livingstone et al., 2013; Smith et al., 2017; Stearns et al., 2008), and have only recently distinguished between conduit types under Antarctic glaciers (Dow et al., 2020; Wei et al., 2020). However, a growing body of work suggests a variety of drainage styles may be important in Antarctica, with obvious relevance to ice sheet dynamics.

In Antarctica, shallow hydropotential gradients and the lack of significant surface melt has led to the conventional paradigm that subglacial water fluxes are too small to permit stable channelized drainage beneath the ice sheets (e.g., Alley, 1989; Carter et al., 2017; Walder and Fowler, 1994; Weertman, 1972). This assumption has led to the use of purely distributed subglacial hydrology models (e.g., Alley, 1996; Le Brocq et al., 2009), or simplifying approximations of effective pressure in large-scale Antarctic ice sheet models (e.g., Asay-Davis et al., 2016; Cornford et al., 2020; Leguy et al., 2014; Nias et al., 2018; Yu et al., 2018). However, channelized drainage under Antarctic ice sheets has recently been inferred through observations of ice shelf basal melt channels (Drews et al., 2017; Le Brocq et al., 2013; Marsh et al., 2016), radar specularity content (Schroeder et al., 2013), and subglacial hydrology models (Dow et al., 2020; Wei et al., 2020). In the absence of surface meltwater, subglacial channels must be sustained through

basal melting, and the presence of basal melt channels under ice shelves suggest that their grounded counterparts must persist stably for decades or centuries (Le Brocq et al., 2013; Marsh et al., 2016).

Thwaites Glacier contains enough ice to raise sea level 65 cm (Rignot et al., 2019), and may currently be undergoing an unstable retreat, likely triggered by increased melting of its ice shelf and terminus (Hoffman et al., 2019; Joughin et al., 2014; Milillo et al., 2019; Rignot et al., 2014; Seroussi et al., 2017). Ice flux from Thwaites Glacier increased 76% between 1976–2013 (Mouginot et al., 2014), coinciding with thinning rates of up to 10 m yr^{-1} and a surface acceleration of 100 m yr^{-1} near the grounding line (Gardner et al., 2018; Helm et al., 2014; Pritchard et al., 2009). While bed topography primarily regulates Thwaites Glacier retreat, uncertainty in basal friction laws, ice flow models, and ice shelf melt parameterizations could affect mass loss projections for this century by up to 300% (Yu et al., 2018). As a prominent control on both basal friction and submarine melting, subglacial hydrology has the potential to be a critical component of Thwaites Glacier dynamics, yet the configuration of its drainage network is poorly understood.

Using a recent survey of radar specularity content, Schroeder et al. (2013) hypothesized that channelized subglacial drainage is pervasive within 75 – 100 km of the Thwaites Glacier grounding line. However, subsequent satellite detection of subglacial lakes led to the interpretation that such channels may only be ephemeral, forming only during lake drainage events (Smith et al., 2017). Here, we pair remote sensing with the 2-dimensional subglacial hydrology model implemented within the MPAS-Albany Land Ice Model (MALI) (Hoffman et al., 2018), to provide a more complete picture of the likely configuration of the Thwaites Glacier subglacial

drainage system. We run a suite of 138 modeling simulations, then compare our results with the observed radar specularity content of Schroeder et al. (2013) to define a subset of scenarios as possible representations of reality. Results from this subset are then collated with ice shelf basal melt rates and common parameterizations of basal friction to explore the significance of channelization on submarine melt rates and ice dynamics.

2.2 Methods

2.2.1 Model Framework. Here, we use only the subglacial hydrology component of MALI, which contains both distributed and channelized flow components, and operates on an unstructured, two-dimensional Voronoi grid. Velocities and fluxes are calculated on the edge midpoints of each cell, and all other variables are located at cell centers. Channel segments connect the centers of neighboring cells. The distributed system is treated as a macroporous sheet that is designed to resemble the bulk flow of water through cavities on the lee-sides of bedrock bumps (Flowers, 2015; Flowers and Clarke, 2002; Hewitt, 2011), but may also reasonably describe flow through other porous media, such as till or till canals (Flowers, 2015; Hewitt, 2011; Hoffman et al., 2016). The distributed system discharge is given by:

$$\vec{q} = -k_q W^{\alpha_1} \left|\nabla\phi\right|^{\alpha_2} \nabla\phi \tag{2.1}$$

where k_q is the conductivity coefficient of the distributed system, W is the water thickness, and α_1 and α_2 are $\frac{5}{4}$ and $-\frac{1}{2}$, respectively, to resemble a Darcy-Weisbach flow law. The hydropotential, ϕ, is defined as:

$$\phi = \rho_w g Z_b + P_w. \tag{2.2}$$

where ρ_w is the water density, g is the gravitational acceleration, Z_b is the bed topography (Figure 2.1a), and P_w is the distributed water pressure. It is assumed all basal cavities remain filled, and thus water thickness is a function of cavity opening from basal sliding over bedrock bumps and creep closure:

$$\frac{dW}{dt} = c_s \left|\vec{u}_b\right| (W_r - W) - c_{cd} A_b N^3 W \tag{2.3}$$

where c_s is a bed roughness parameter, $\vec{u}_b$ is the ice basal sliding velocity (Figure 2.1b), W_r is the maximum bed bump height, c_{cd} is a creep scaling parameter for the distributed system, and A_b is the temperature-dependent ice flow rate parameter for basal ice. The effective pressure, N, is defined as the difference between the ice overburden and water pressures: $N = \rho_i g H - P_w$, for ice thickness H and ice density ρ_i.

The channelized system formulation resembles that of Werder et al. (2013), where channel discharge is given by:

$$\vec{Q} = -k_Q S^{\alpha_1} \left|\nabla\phi\right|^{\alpha_2} \nabla\phi \tag{2.4}$$

where k_Q is the channel conductivity coefficient. Channel cross-sectional area, S, is a function of creep closure, and melting/freezing due to the dissipation of potential energy, Ξ, and pressure-dependent changes to the sensible heat of water, Π:

$$\frac{dS}{dt} = \frac{1}{\rho_i L}(\Xi - \Pi) - C_{cc} A_b N^3 S. \tag{2.5}$$

Here, L is the latent heat of melting and C_{cc} is a creep scaling parameter for channels. Ξ includes dissipation terms for both the distributed and channelized systems, so that:

$$\Xi = \left|\vec{Q}\frac{d\phi}{ds}\right| + \left|l_c q_c \frac{d\phi}{ds}\right| \tag{2.6}$$

where s is the along-channel spatial coordinate, and q_c is the discharge in the distributed system within a distance, l_c, from the channel. Using this formulation,

channels may only develop if there exists sufficient discharge in the distributed system for melting to overcome creep closure. In our experiments, we disabled the pressure-dependent melting/freezing term, Π, to avoid nonphysical instabilities arising from intricate bed topography. The implications of neglecting this term are discussed in Section 2.4.3.

Closing the system of equations requires the conservation of water mass within the combined distributed and channelized subglacial drainage systems, and a conservation of energy equation for the production of basal meltwater. Conservation of mass is written as:

$$\frac{dW}{dt} = -\nabla \cdot \vec{q} - \left[\frac{\partial S}{\partial t} + \frac{\partial Q}{\partial s}\right] \delta(x_c) + \frac{m_b}{\rho_w}, \tag{2.7}$$

where $\delta(x_c)$ is the Dirac delta function applied along the locations of the linear channels and m_b is the production of basal meltwater (Figure 2.1d). Conservation of energy is written as

$$m_b L = G + \vec{u}_b \cdot \vec{\tau}_b \tag{2.8}$$

for basal shear $\vec{\tau}_b$ and geothermal flux G.

Time derivatives are discretized using an explicit forward Eulerian method that fulfills advective and diffusive Courant-Friedrichs-Lewy (CFL) conditions for the distributed system, and advective CFL conditions for the channelized system. Model outputs are written at one month intervals and all reported results are averaged over five years of model time to smooth any minor oscillations remaining in the system.

2.2.2 Thwaites Model Domain. We ran the majority of our simulations on a variable resolution domain of Thwaites Glacier that has a 4 km cell spacing over the fast flowing regions and coarsens to 14 km at the interior

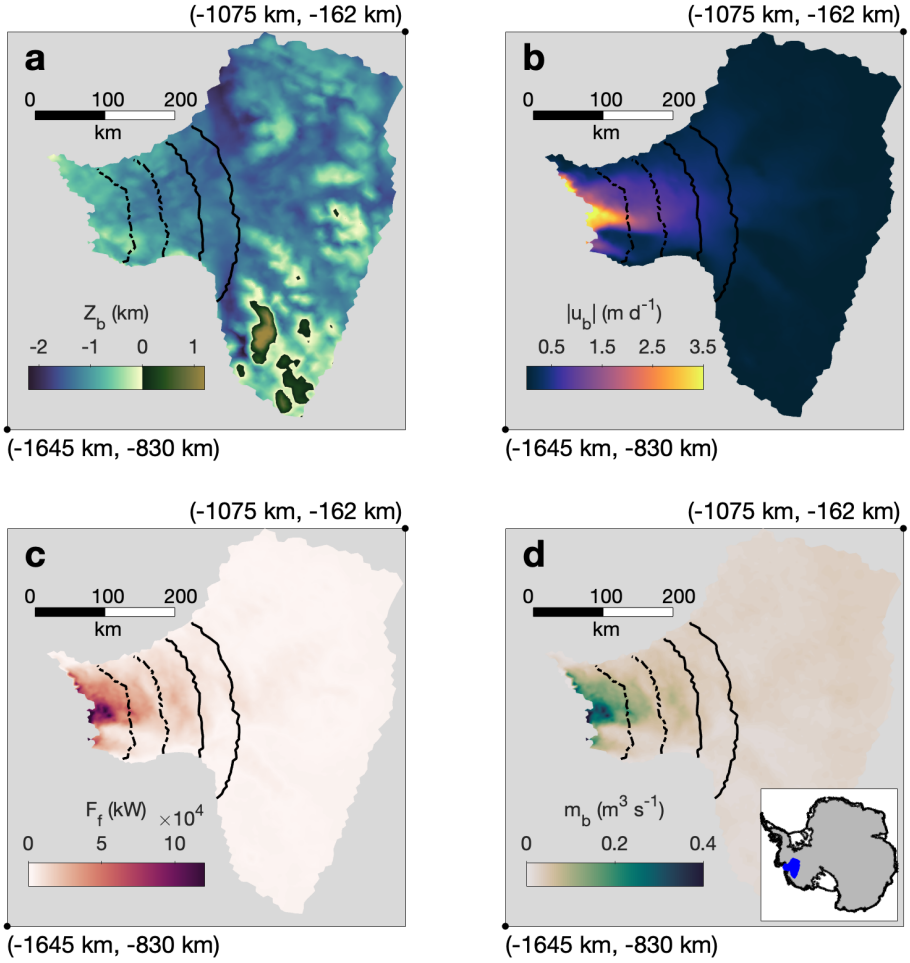

Figure 2.1. **a)** Bed topography (Z_b), **b)** basal sliding speed ($|\vec{u}_b|$), **c)** basal friction heat flux (F_f), and **d)** the production of basal meltwater (m_b) used as inputs for the subglacial hydrology model. Transects spaced every 50 km from the terminus (used for determination of flux steady-state and in Figure 2.6) are shown as black lines, with the dotted lines spanning the transition zone of Schroeder et al. (2013). The locations of map corners are given in Standard Antarctic Polar Stereographic coordinates. The inset in **d** depicts the location of Thwaites Glacier (blue) within Antarctica.

ice divide, for a total of 4267 grid cells. An additional simulation was performed with a higher resolution mesh that uses 1 km cell spacing in fast flowing regions, coarsening to 8 km at the interior ice divide, for a total of 75500 cells. The bedrock and ice geometry were interpolated onto the model mesh using conservative remapping from the BedMachine Antarctica v1 ice thickness and bed elevation

dataset (Morlighem et al., 2020). However, a maximum bed elevation of 1200 m and a ice thickness of 550 m was imposed over Mt. Takahe (>250 km from the terminus) to avoid instabilities arising from steep bed topography. The resulting thickness gradients were then smoothed by running only the ice dynamics and geometry evolution portions of MALI for 15 years. The geothermal flux was interpolated from the 15 km resolution dataset of Martos et al. (2017). The ice sliding velocity ($\vec{u}_b$) and basal shear stress ($\vec{\tau}_b$) fields required by the subglacial hydrology model follow the methods used by Hoffman et al. (2018) to generate a present-day initial condition, where a basal friction parameter is optimized in order to minimize the misfit between modeled and observed ice surface velocity (Perego et al., 2014).

Within the subglacial hydrology model, no flow lateral boundary conditions were applied at the ice-covered lateral boundaries of the model domain. At the glacier grounding line, a Dirichlet boundary condition on the hydropotential (ϕ) was applied equal to the hydropotential of seawater at each grid cell seaward of the grounding line,

$$\phi_o = \rho_w g Z_b - \rho_o g Z_b, \tag{2.9}$$

where $\rho_o = 1028$ kg m^{-3} is the density of ocean water. Note this boundary condition results in hydropotential values close to zero but spatially varying as ocean pressure varies along the grounding line with the thickness of the ocean water column. Additionally, inflow from the ocean to the subglacial drainage system is disallowed if the hydropotential underneath the grounded ice falls below the ocean hydropotential. This condition can occur due to a spatially variable, ocean-lateral boundary condition and the assumption of constant density within the subglacial drainage system, which in combination with subglacial channelization, can locally

result in the modeled unstable inflow of ocean water. The model was spun-up with channelization disabled and a k_q value of 1.5×10^{-3} $m^{7/4}$ $kg^{-1/2}$ to allow water pressures to equilibrate at > 90 % overburden pressure. All other simulations were then initialized from the steady-state solution of this run.

2.2.3 Parameter Sweep and Sensitivity Analysis. Four primary yet poorly constrained parameters exist in equations 2.1, 2.3, and 2.4: k_q, k_Q, W_r, and c_s. While some theoretical and observational basis exists for the values of these parameters, the appropriate values are uncertain and likely vary by glacier basin. A few recent studies have addressed this uncertainty by using inversion techniques to infer values of hydraulic parameters (e.g., Brinkerhoff et al., 2021,1; Irarrazaval et al., 2021; Koziol and Arnold, 2017). Here, we used an ensemble approach and compared results to multiple limiting criteria to identify the most realistic parameter combinations. Our ensemble consisted of 113 different channel-enabled simulations and 25 simulations disallowing channelization. All runs were within a plausible parameter space based on observations and theory, as described below.

Observations of jökulhlaups suggest the typical Manning roughness, n, of subglacial channels ranges from 0.023 – 0.12 $m^{-1/3}$ s (Bjornsson, 1992; Clarke, 1982, 2003; Nye, 1976). We can translate these Manning roughness values to the equivalent channel conductivity range of 0.03 – 0.17 $m^{7/4}$ $kg^{-1/2}$ using (Werder et al., 2013):

$$k_Q{}^2 = \frac{1}{\rho_w g n^2 (\frac{2}{\pi})^{2/3} (\pi + 2)^{4/3}}. \tag{2.10}$$

However, jökulhlaups do not provide an exhaustive range of roughness characteristics for channel flow, and dye-trace breakthrough curves have indicated that n values for low-discharge, high-friction subglacial channels could be as low as

$n = 0.68$ m$^{-1/3}$ s (Gulley et al., 2012), or $k_Q = 0.006$ m$^{7/4}$ kg$^{-1/2}$. On the other extreme, the Manning roughness of a smooth brass pipe is 0.009 m$^{-1/3}$ s (Chow, 1959), or $k_Q = 0.44$ m$^{7/4}$ kg$^{-1/2}$, which we consider a generous upper end-member for k_Q. We therefore ran our model with k_Q ranging from 0.005 – 0.5 m$^{7/4}$ kg$^{-1/2}$ to encompass the full set of plausible values.

Because k_q may be chosen to portray porous flow through cavities in till or bedrock, we selected k_q values to be within the appropriate range of till or greater. Estimates for the hydraulic conductivity, κ, of subglacial till ranges widely from 10^{-12} – 5×10^{-4} m s^{-1} (Fountain and Walder, 1998), which can be converted to an equivalent distributed conductivity coefficient in our model via (Bueler and van Pelt, 2015):

$$k_q = \frac{\kappa}{\rho_w g W^{1/4} \left|\nabla\phi\right|^{-1/2}}. \tag{2.11}$$

Using a characteristic W of 0.1 (see below) and $|\nabla\phi|$ of 100 Pa m^{-1} (approximated from our model domain), we estimate the conductivity coefficient of subglacial till in our model would be 10^{-15} – 10^{-6} m$^{7/4}$ kg$^{-1/2}$, which should span our lower limit for k_q. In practice, however, simulations with $k_q < 1.5 \times 10^{-5}$ m$^{7/4}$ kg$^{-1/2}$ were over-pressurized and did not reach steady-state. Although no proper upper bound exists for k_q, we attempted to limit our k_q parameter sweep to values that kept the average water pressure $> 90\%$ flotation, which typically occurred for $k_q \leq 5 \times 10^{-3}$ m$^{7/4}$ kg$^{-1/2}$ across different bed roughness combinations. This choice was based off of near flotation water pressures observed at Ice Stream B (Engelhardt and Kamb, 1997) and estimated for Pine Island Glacier (Gillet-Chaulet et al., 2016), which we assume are similar to those beneath Thwaites Glacier.

In theory, W_r represents the characteristic bed bump height (decimeter-scale), while c_s represents the characteristic meter-scale bed bump spacing (Figure

2.2). Typical values used for W_r and c_s are $\sim$ 0.1 m (e.g., de Fleurian et al., 2018; Dow et al., 2020; Hewitt, 2011; Schoof, 2010; Schoof et al., 2012; Werder et al., 2013) and $\sim$ 0.5 m^{-1} (e.g., de Fleurian et al., 2018; Dow et al., 2020; Hoffman and Price, 2014; Schoof et al., 2012; Werder et al., 2013), respectively. We tested the sensitivity of our results to these parameters by running the model with 6 different combinations of W_r = 0.05 m, 0.1 m, 0.2 m, and 1.0 m and c_s = 0.25 m^{-1}, 0.5 m^{-1}, and 1.0 m^{-1}, holding one at the default value of W_r = 0.1 m or c_s = 0.5 m^{-1}, and varying the other parameter. We spaced k_q and k_Q samples at consistent intervals, and stopped sampling conductivity parameter space when runs failed to reach steady-state or were under-pressurized ($<$ 90% flotation). As a result, we conducted a different number of runs for each bed parameter combination, ranging between 9 – 29 channel-enabled simulations with k_q and k_Q values within their plausible ranges (Appendix A).

Additionally, for each pair of bed roughness parameters, we ran 4-5 simulations with channelization disabled across a similar range of k_q values (25 runs total). These were used as counter-examples to explore the impact of subglacial channel drainage under Thwaites Glacier.

By design, the parameter sweep forces our model to operate at the limit of its ability to remain stable, and thus some runs failed to reach a true steady-state. This occurred for two main reasons: either local numerical instabilities developed in the channel model, or the domain became over-pressurized so that the adaptive timestep became impractically small to meet the pressure CFL condition. We thus found it useful to define two separate steady-state criteria that allowed us to identify which information was usable from each run, and categorized runs as either reaching a pressure steady-state or a flux steady-state. Pressure steady-state

was defined as $\langle \frac{\partial N_{ij}}{\partial t} N_{ij}^{-1} \rangle \leq 0.5\%$, where $\langle \rangle$ denotes an average over all grounded grid cells j and time steps i over 5 years of model time. Flux steady-state was attained when the area-integrated version of equation 2.7 upstream of a specified cross-glacier transect was met within 0.5% when averaged over 5 years. Transects were defined every 50 km within 200 km of the grounding line (Figure 2.1). Runs that failed to reach flux steady-state did not represent steady systems where the subglacial discharge realistically balanced the production of meltwater, and so it was not possible to accurately assess the relative fraction of channel discharge to distributed system discharge. Therefore, we report results regarding water thickness and water pressure from pressure steady-state runs, but only report discharge results from runs that also reached flux steady-state at each transect.

We use this approach because water pressure and thickness fields from pressure steady-state runs strongly resemble their flux steady-state neighbors in parameter space, yet the channel model fails to reach equilibrium in some runs due to local channel instabilities that do not affect area-averaged water pressure or water thickness. We thus have confidence that pressure steady-state runs still yield useful information about water pressure and thickness. In some cases, instabilities could be avoided by changing the englacial porosity, which acts as a buffer between meltwater production and the subglacial system but does not affect the steady-state configuration. As our goal was to explore as much of parameter space as possible, runs were continually restarted until either reaching flux steady-state, forming an unpreventable numerical instability, or becoming computationally untenable to keep running. Simulations that did not reach either steady-state criteria were discarded. The sensitivity of our results to our steady-state criteria is discussed in Appendix A.

2.2.4 Model Comparison with Observed Specularity Content.

All simulations that reached a pressure steady-state were compared with observed radar specularity content from Thwaites Glacier (Schroeder et al., 2013) to further narrow the range of viable parameter combinations. Specularity content determined from airborne ice-penetrating radar is commonly used for detecting subglacial water bodies beneath ice sheets (e.g., Dow et al., 2020; Schroeder et al., 2015,1; Young et al., 2017,1), and has recently been used to validate a subglacial hydrology model of Totten Glacier, East Antarctica (Dow et al., 2020). Although our methods differ, we rely on the same concepts that make specularity content a useful tool for subglacial hydrology model validation.

Ponding within the subglacial drainage system creates flat, reflective surfaces that cause bright specular returns, as opposed to bedrock, which has a lower dielectric contrast to ice, and whose rough texture scatters energy (Schroeder et al., 2015). Similarly, the curved surface of less uniform conduits such as channels or rough linked cavities scatters energy uniformly in all directions, creating areas of low specularity content, despite the presence of water (Schroeder et al., 2013). High specularity content, therefore, unequivocally depicts flat-surfaced water bodies in an inefficient distributed system, while low specularity content can either represent a distributed system below its capacity (bedrock cavities are smaller than their maximum size allowed by bed roughness), or the existence of water in rougher, more variably shaped conduits, such as channels. However, by comparing specularity content with a numerical model, we are able to determine which of these two features is responsible for creating the weakly specular regions beneath Thwaites Glacier.

To compare specularity content with our model output, we first averaged the specularity content from the North-South and East-West radar transects from Schroeder et al. (2013) onto a 5 km grid. We then defined a water thickness to bump height ratio, R_{wt}, which indicates the degree to which modeled conditions would produce flat and extensive interfaces between water and ice at the glacier bed, and therefore highly specular surfaces:

$$R_{wt} = \frac{W}{W_r}. \tag{2.12}$$

For $R_{wt} \gtrapprox 1$, distributed water thickness nears or exceeds bed bump height, thus creating a flat, highly-specular surface of water. However, for $R_{wt} \ll 1$ bedrock geometry determines the roughness of the lower interface, and the location is considered rough-surfaced and non-specular (Figure 2.2). Additionally, with a proper value of k_q, R_{wt} can also parameterize till saturation, with low and high R_{wt} indicating under-saturated (non-specular) till and saturated (specular) till, respectively. For easy comparison, R_{wt} was calculated for each model grid cell, then interpolated onto the same 5 km grid as the specularity content data. Note that a spatially uniform W_r is likely unrealistic but is an assumption commonly used in subglacial hydrology models. As applied here, Equation 2.12 is used as a relative metric of how close to maximum size a linked cavity system is, and this interpretation would apply to both uniform or spatially variable bump heights.

Measured specularity content and modeled R_{wt} both represent broad, flat areas of pooled water at high values, but should not be expected to covary when their values are low, due to nonlinearities in the measurements and model formulations, as well as ambiguity in the physical representation of low specularity content. This makes comparing the two difficult, and a simple spatial correlation unlikely to work as a comparison method. Instead, we rely on binary masks that

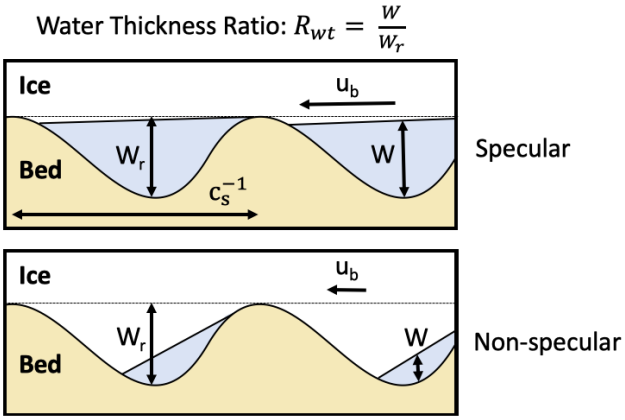

Figure 2.2. Schematic of a specular and non-specular distributed system, as defined by the water thickness ratio, R_{wt}. Physical representations of bed roughness parameters are included.

map where specularity content and R_{wt} are high/low, as determined by their value being above/below a threshold value. Unfortunately, this method requires choosing thresholds for what is considered high for each quantity, which we address by creating a population of masks for each variable, each using a different threshold within a reasonable range.

Specularity content depends on the geometry of ice thickness, survey geometry, radar processing, and subglacial water geometry (Haynes et al., 2018; Schroeder et al., 2015,1; Young et al., 2016). As a result, specularity content can be interpreted as the relative amount of the bed that is covered by flat subglacial water bodies, which gradually transitions from non-specular to specular with the addition of water. Therefore, the classification of high or low specularity content is determined relative to a specific survey, and we base the threshold value used for creating specularity masks on the cumulative distribution of specularity within our dataset (Figure B.2). As masks are sensitive to the exact choice of threshold, we created 11 specularity masks with thresholds, S^{crt}, ranging from 0.15 – 0.25 at evenly-spaced intervals of 0.01, which selects for the greatest $\sim$ 5 – 20% of

our specularity data. Similarly, we assume specular surfaces require cavities that are near maximum size (Figure 2.2), so there must be a range of R_{wt} near 1 that could plausibly represent high specularity. Again, we account for this range by creating 6 masks of R_{wt} using thresholds, R_{wt}^{crt}, between 0.95 – 1.0 at intervals of 0.01. The resultant 66 combinations of specularity content and R_{wt} masks were then compared using two criteria:

1. The masks were divided into four zones based on Schroeder et al. (2013): a near-terminus non-specular zone thought to have channelized flow, a lower specular zone approximately at the transition zone of Schroeder et al. (2013), an upper specular zone where ponding is thought to occur, and an upper non-specular zone likely containing little basal water (Figure 2.3). The specularity content and R_{wt} masks had to agree for a majority of the cells within each zone.

2. The two masks needed to have an overall correlation coefficient of ≥ 0.35, which was empirically tuned to select for similar patterns between masks when paired with the first criterion.

Model runs that had at least one R_{wt} mask meet these comparison criteria with at least one specularity mask were deemed data-compatible and used for further analysis. By admitting runs that satisfy the comparison criteria for even a single set of masks out of the 66 compared, we make the selection highly inclusive so that conclusions about extent of channelization consider the widest range of parameters compatible with specularity observations. Hereafter, runs that additionally met flux steady-state criteria will be referred to as data-compatible FSS runs. See Appendix B for more information about these comparison criteria, as well as a flow chart illustrating the comparison process (Figure B.1).

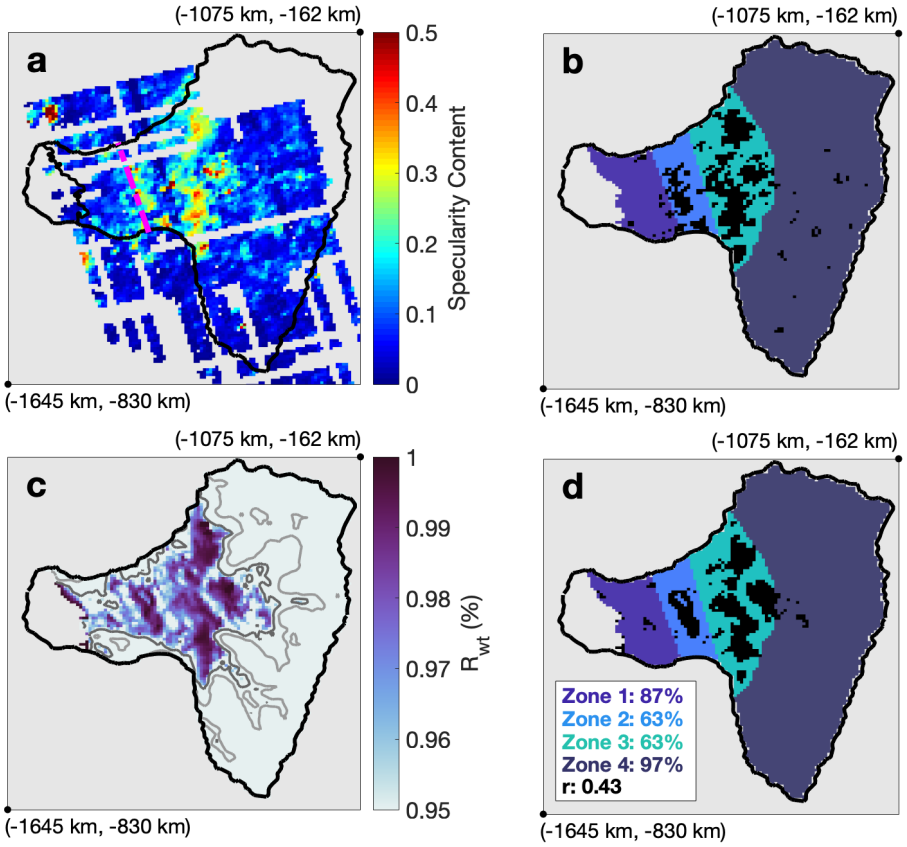

Figure 2.3. An example comparison of catchment-scale features identified with binary masks (black) of observed specularity content and modeled R_{wt}. **a)** radar specularity content (Schroeder et al., 2013) and **c)** R_{wt} for a data-compatible flux steady-state model run, together with their coinciding binary masks, **b)** ($S^{crt} = 0.19$) and **d)** ($R_{wt}^{crt} = 0.98$), respectively. The pink dashed line in **a** marks the transition between highly-specular, distributed drainage and channel-dominated drainage, as hypothesized in Schroeder et al. (2013). The four zones used for comparison between specularity content and R_{wt} are color-coded in **b** and **d**. Light and dark gray lines in **c** are the 50% and 90% R_{wt} contours, respectively. The percent match between masks within each zone and the overall correlation are given in **d**. The locations of map corners are given in Standard Antarctic Polar Stereographic coordinates.

2.3 Results

2.3.1 Channel-Enabled Parameter Sweep.

2.3.1.1 Model Tuning and Correspondence with Specularity

Content. Of our 113 channel-enabled runs, 39 met our pressure steady-state

criterion, while 23 of those also met our flux steady-state criterion across all transects. 20 pressure steady-state runs, including 13 flux steady-state runs, had at least one R_{wt} and specularity mask combination that met our comparison criteria, and were therefore considered possible representations of reality. Each of these runs showed a strong resemblance between R_{wt} and specularity content masks (Figure 2.3). Average water pressures in data-compatible runs were between 91-96% flotation, and in general, runs that did not correspond with specularity content had water pressures outside of this range.

All 66 combinations of S^{crt} and R_{wt}^{crt} masks yielded successful comparisons for some sets of parameters, although successful pairings varied with model parameters. Across all runs, comparison success rate exponentially increased with higher values of R_{wt}^{crt}, with R_{wt}^{crt} of 0.99 or 1.0 accounting for 60% of all matches. Conversely, masks with $R_{wt}^{crt} = 0.95$ only accounted for 4% of the 713 successful mask combinations. The few runs that had successful matches with an R_{wt}^{crt} of 0.95 also had successful matches using higher R_{wt}^{crt} thresholds, indicating this choice of lower bound does not influence our results. Match success rate was not sensitive to S^{crt}, and each threshold value was responsible for 7–10% of successful matches.

Data-compatible runs either had k_q values of 1.5×10^{-4} or 5×10^{-4} $m^{7/4}$ $kg^{-1/2}$ (Figure 2.4), with the only exceptions occurring when $W_r = 0.05$ m or $W_r = 1.0$ m, in which data-compatible k_q values reached 1.5×10^{-3} and 5×10^{-5} $m^{7/4}$ $kg^{-1/2}$, respectively. The range of k_q in data-compatible runs is above that of pure glacial till, and is consistent with a bed composed of both till and bedrock, as is thought to be the case for Thwaites Glacier (Joughin et al., 2009; Muto et al., 2019a,1). For the channelized conductivity values, all data-compatible runs had k_Q values of 0.005 – 0.1 $m^{7/4}$ $kg^{-1/2}$, coinciding with the expected range given by dye-

trace breakthrough curves and Jökulhlaup observations (Bjornsson, 1992; Clarke, 1982, 2003; Gulley et al., 2012; Nye, 1976). No runs with $k_Q = 0.5$ m$^{7/4}$ kg$^{-1/2}$, outside of our brass pipe upper limit, reached either steady-state criterion. Typical channel velocities in our data-compatible runs do not exceed the typical observed Jökulhlaup range of 0.6 – 2.7 m s^{-1} (Magnusson et al., 2007; Werder and Funk, 2009, Figure 2.4), which provides an additional loose constraint on the validity of our channel model, although currently no observations of subglacial flow velocities exist from Antarctica.

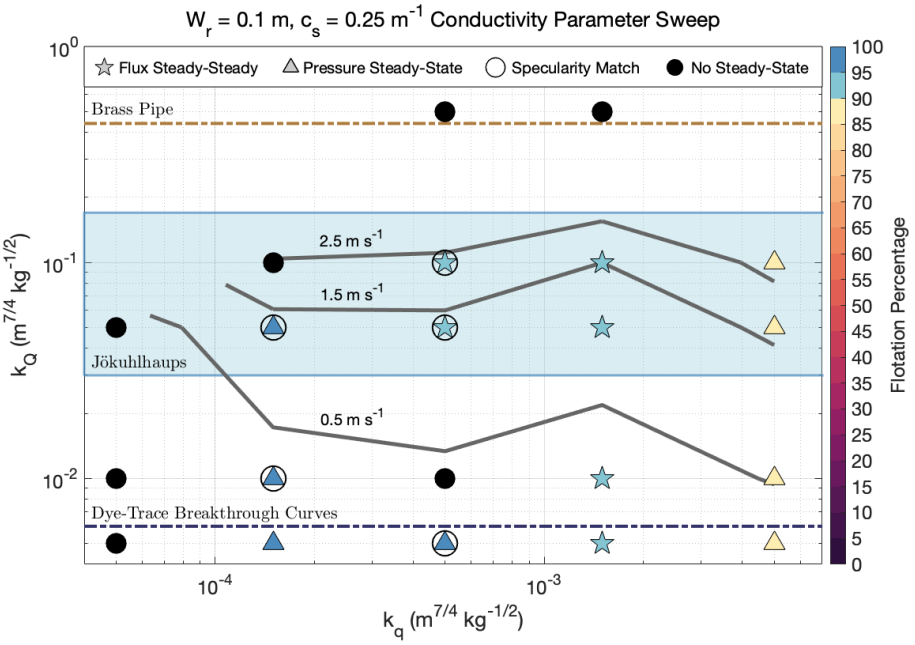

Figure 2.4. The conductivity parameter sweep for bed roughness parameters $W_r = 0.1$ m and $c_s = 0.25\ m^{-1}$. Stars represent runs that reached flux (and pressure) steady-state, triangles symbolize pressure steady-state simulations, and filled black circles depict runs that did not reach either steady-state criterion. Symbols for steady-state runs are color-coded by the average flotation percentage of grounded ice. Circles around stars or triangles indicate runs that matched observed specularity content, and are considered data-compatible. Gray lines are 95^{th} percentile channel velocity contours for channels with $\vec{Q} > 5$ m^3 s^{-1}. k_Q limits determined from a brass pipe and dye-trace breakthrough curves are plotted as brown and dark-blue dashed lines, respectively, and the blue shaded area represents the typical observed Jökulhlaup k_Q range.

2.3.1.2 Extent of Channelization in Data-Compatible Simulations.

Subglacial channels were ubiquitous in all data-compatible FSS runs. In most of these runs, channels with discharges over 5 m^3 s^{-1} extended at least 150 km from the glacier terminus, with some channels reaching farther than 200 km (Figure 2.5). The initiation of these channels generally coincided with the upper specular zone observed in Schroeder et al. (2013). However, channel discharge between 150 - 200 km was divided between 2 to 4 small channels, each with an individual discharge of less than 20 m^3 s^{-1}. At 150 km from the terminus, distributed discharge was still the dominant mode of drainage, with average channelized and distributed discharges of 27 $\pm$ 18 and 42 $\pm$ 19 m^3 s^{-1} ($\pm$ indicates standard deviations), respectively, across data-compatible runs.

A transition occurs between 50–100 km from the terminus from a distributed-dominated to a channel-dominated system, coinciding with the region where Schroeder et al. (2013) hypothesized channelization begins under Thwaites Glacier. In our model, all data-compatible runs had formed at least one channel transporting $>$ 10 m^3 s^{-1} by 100 km from the terminus, and by 50 km, these channels had grown and converged into 1-2 primary channels, each draining up to 50 m^3 s^{-1} of water. Our 50 km transect is the first at which channelized drainage slightly outweighs distributed drainage, with discharges of 55 $\pm$ 21 and 47 $\pm$ 20 m^3 s^{-1}, respectively (Figure 2.6). Consistent with Joughin et al. (2009), basal friction melting is the primary contributor of melt in our model, and the 50–100 km transition to channelized flow coincides with a substantial increase in basal friction melt rate (Figures 2.1, 2.5, and 2.6) .

Channelized discharge grows rapidly within 50 km of the terminus. By the point at which water reaches the grounding line, channelized drainage accounts for

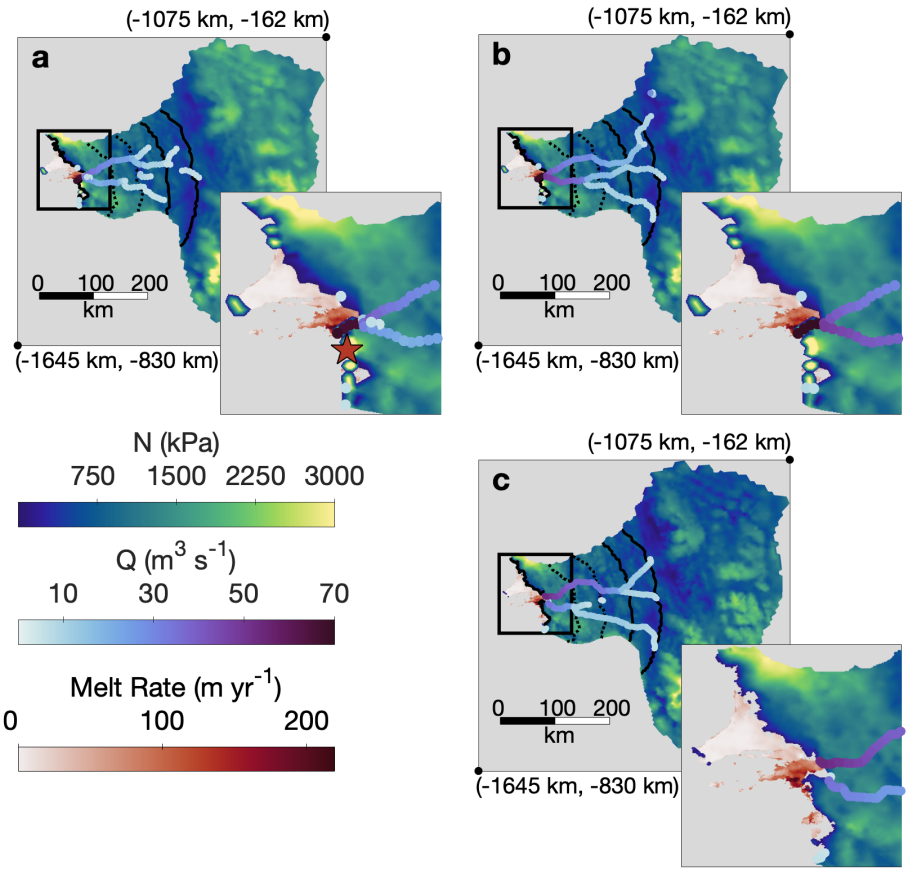

Figure 2.5. **a)** Average effective pressure and channel discharge across all data-compatible FSS runs. **b–c)** Effective pressure and channel discharge for **c)** the high-resolution model, and **b)** its low-resolution counterpart. The insets are enlarged views of the black boxes, and the star in **a** indicates the location of the secondary channel seen in one data-compatible FSS run. Sub-ice-shelf melt rates from Adusumilli et al. (2020) are plotted in all frames. For clarity, only channels with $\vec{Q} > 5$ m^3 s^{-1} are pictured in each frame. Again, transects spaced every 50 km from the terminus (used for determination of flux steady-state and in Figure 2.6) are shown as black lines, with the dotted lines spanning the transition zone of Schroeder et al. (2013). The locations of map corners are given in Standard Antarctic Polar Stereographic coordinates.

127 ± 24 m^3 s^{-1} of runoff into the ocean, whereas only 25 ± 21 m^3 s^{-1} is expelled through the distributed system (Figure 2.6). In all data-compatible FSS runs, the majority of channel discharge at the grounding line occurred through one primary channel with a discharge of 80 ± 24 m^3 s^{-1} near the center of the grounding line

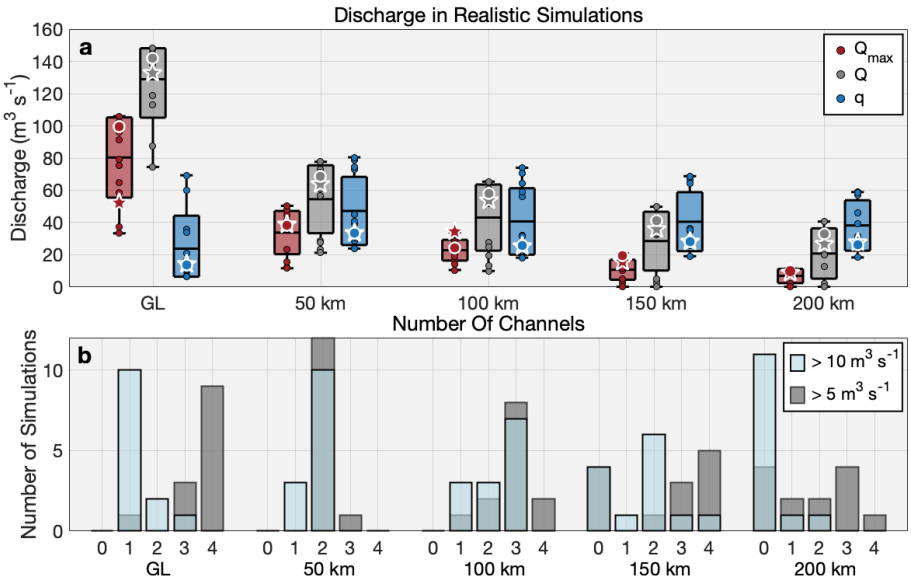

Figure 2.6. **a)** Total distributed (blue) and channel discharge (gray), as well as the discharge of the largest channel (red) across each transect (see Figure 2.5) for all data-compatible FSS runs (circles). Boxplots indicate the maximum, minimum, mean, and standard deviations. The stars indicate the high-resolution model, and the white-edged circles designate its low-resolution counterpart. **b)** The number of channels with $\vec{Q} > 5$ m^3 s^{-1} (gray) and $\vec{Q} > 10$ m^3 s^{-1} (blue) at each transect for all data-compatible FSS runs.

(-1.5369×10^6 m, -4.7298×10^5 m; Standard Antarctic Polar Stereographic). This location corresponds to the region of high basal melting observed at the Thwaites Ice Shelf in Adusumilli et al. (2020) (Figure 2.5). In one simulation, a secondary channel intersects the grounding line with a discharge of 38 m^3 s^{-1} at (-1.5310×10^6 m, -4.8585×10^5 m) where we lack basal melt data (Figure 2.5a). Other channelized discharge across the grounding line occurs through very small channels ($\lesssim 10$ m^3 s^{-1} scattered along the marine boundary.

2.3.2 Grid Resolution Sensitivity Analysis.

One data-compatible FSS simulation ($k_Q = 0.05$ m$^{7/4}$ kg$^{-1/2}$, $k_q = 4 \times 10^{-4}$ m$^{7/4}$ kg$^{-1/2}$, c_s 0.5 m^{-1}, $W_r = 0.1$ m) was rerun to flux steady-state with the high-resolution domain. The high-resolution run matched observed specularity content, and produced effective

pressures and water fluxes that closely resembled its low-resolution counterpart. High-resolution channels followed very similar pathways as those in the low resolution model (Figure 2.5b–c), and distributed and channelized discharges at each transect were approximately equal to those at low-resolution (Figure 2.6a). The main exception occurred at the grounding line, where the two main channels reached the ocean independently in the high-resolution model, but merge just above the grounding line with lower resolution (Figure 2.5b–c). This explains the almost twofold discrepancy of maximum channel discharge at the grounding line between the two resolutions (Figure 2.6a). Additionally, the high-resolution run had lower effective pressures near the upper domain boundary, although effective pressures within 300 km of the terminus are in strong agreement with the low-resolution model (Figures 2.5, 2.8a).

2.3.3 Distributed-only Model Configuration. Average water pressures in our 25 distributed-only simulations ranged from 74-98% flotation, and all met our flux steady-state criteria. However, no distributed-only run had a R_{wt} field that matched observed specularity content. In particular, the greatest mismatch occurred between 0 – 50 km and 100 – 150 km of the grounding line, where R_{wt} was consistently over R_{wt}^{crt}, but where observed specularity content was low (Figure 2.7). In other cases where the average flotation percentage was below 90%, water thicknesses were too low to produce any regions of $R_{wt} \geq R_{wt}^{crt}$. Furthermore, distributed-only simulations had unrealistically low effective pressures within 150 km of the terminus. Of the runs with an average water pressure over 90% flotation, many were at or near flotation within 200 km of the terminus (Figure 2.8a). Within 50 km of the terminus, the average effective pressure across

these distributed-only runs was one-third that of data-compatible channel-enabled scenarios.

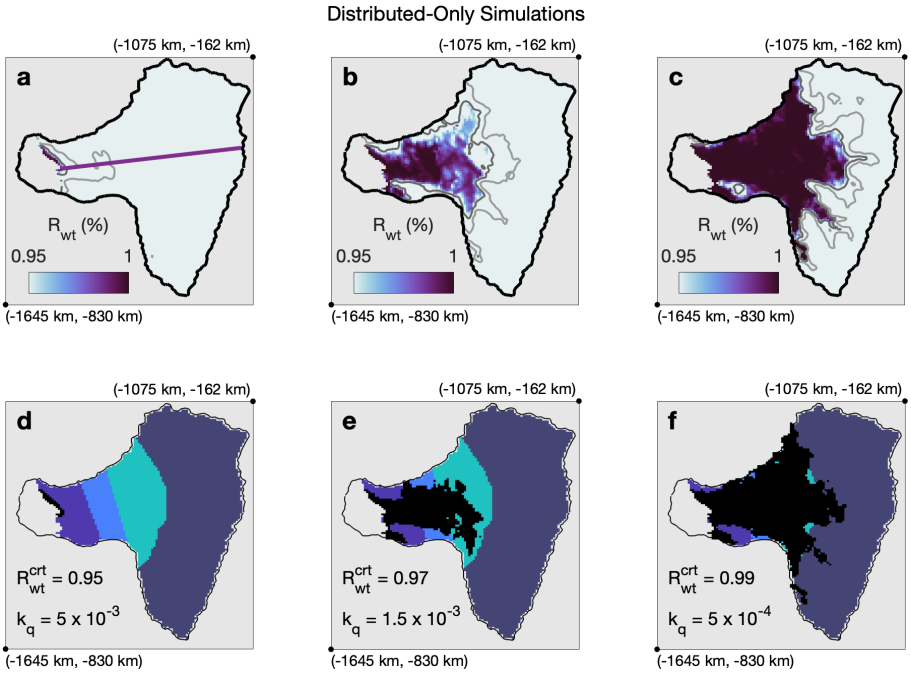

Figure 2.7. Three typical **a–c)** R_{wt} configurations and **d-f)** coinciding binary masks (black) for distributed-only runs. Masks depict regions where R_{wt} is above its threshold value, and thus the distributed system is at or above its capacity. R_{wt} in distributed-only runs generally resembled one of these three patterns. Light and dark gray lines in **a-c** are the 50% and 90% R_{wt} contours, respectively. Color-coding in **d-f** corresponds to the same zones as Figure 2.3. Purple line in **a** is the center-line transect used in Figure 2.8. k_q used in each run, along with the R_{wt}^{crt} used to create the coinciding binary mask, are provided in **d-f**. All three runs had bed roughness parameters $W_r = 0.1$ m and $c_s = 0.5$ m^{-1}.

2.4 Discussion

2.4.1 A Reconciled Framework for Channelization Beneath Thwaites Glacier.

The key result of our study is the likely existence of stable subglacial channels beneath Thwaites Glacier. In our model, channels typically extended over 100–200 km inland, and had grounding line discharges of 80 ± 24 m^3 s^{-1}, much larger than the maximum discharges of 1–5 m^3 s^{-1} and $<$ 25 m^3

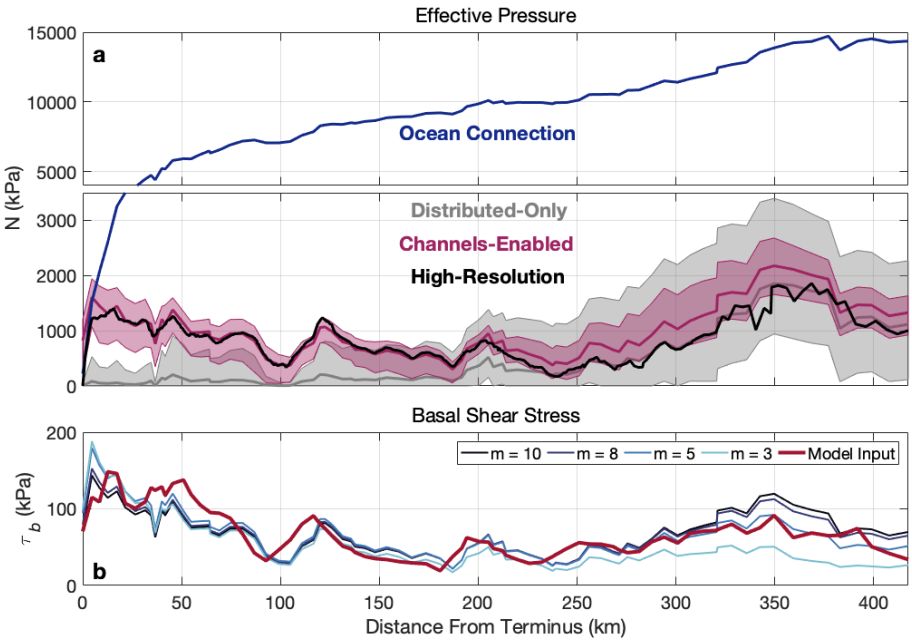

Figure 2.8. **a)** The range and mean (solid line) of effective pressures along the center-line transect in Figure 2.7a for all data-compatible FSS, channel-enabled runs (magenta) and all distributed-only runs above 90% flotation (gray). The black line depicts transect effective pressures from the high-resolution run. Shown in blue is the calculated effective pressure if assuming a perfect hydrostatic connection with the ocean. Note the different y-axis scale in the upper panel. **b)** Basal shear stress used as input in our model (red) plotted with reconstructed basal shear stress using a Budd-style friction law (blue). Blue hues represent different exponents used in the friction law. All lines follow the same center-line transect as in **a**.

s^{-1} modeled at Getz (Wei et al., 2020) and Totten (Dow et al., 2020) glaciers, respectively. No distributed-only experiments matched observed specularity content, and all had unrealistically high water pressures within 100 km of the terminus. This strongly argues that channelized drainage is necessary to explain observed radar specularity content.

Certain geometric and hydrologic conditions at Thwaites Glacier are unfavorable to the development of subglacial channels, and thus the extent of channelization in our model is somewhat surprising. In theory, subglacial channels should develop when the distributed system reaches a critical discharge that is

inversely proportional to the hydropotential gradient (Hewitt, 2011; Schoof, 2010). In Greenland, it is believed that glaciers are unable to reach this critical threshold farther inland where gentle surface slopes weaken the hydropotential gradient and thick ice may expedite creep closure (Chandler et al., 2013; Dow et al., 2014; Meierbachtol et al., 2013). Similar logic could also apply to the thicker and broader Antarctic ice sheets, especially given their insignificant surface melt input. Yet, our model consistently depicts subglacial channels extending 100–200 km inland in all parameter choices. These channels could be explained by the large catchment size (189000 km^2) of Thwaites Glacier (Joughin et al., 2009), its funnel-like geometry, and high basal melt rates of 3.5 $km^3\ yr^{-1}$ (Joughin et al., 2009), which together accumulate enough water to exceed the critical discharge threshold within 100–200 km from the grounding line. At first, the critical discharge may only be met locally (e.g., Hewitt, 2011) through the accrual of water in topographic depressions, which the subglacial channels tend to follow. High basal friction melt rates of 100 – 1000 mm yr^{-1} in the terminal 100 km, as calculated for our model input and by Joughin et al. (2009), are then likely responsible for the increased channelization near the grounding line.

Previous work has offered contrasting hypotheses on the persistence of subglacial channels beneath Thwaites Glacier. Originally, Schroeder et al. (2013) argued radar scattering from widespread concave channels produced the near-terminus, non-specular region they observed. However, an extensive channelized system may not allow for the isolation of subglacial lakes, and the discovery of subglacial lakes beneath Thwaites Glacier suggested channels may be ephemeral, forming only during subglacial lake drainage events (Smith et al., 2017). Based on our model, we here present a refinement of the hypothesis of Schroeder et al. (2013)

that leaves room for the development of the subglacial lakes observed by Smith et al. (2017).

In agreement with Schroeder et al. (2013), we interpret the overlapping regions of observed high specularity content and high R_{wt} between 100 – 250 km from the terminus to unequivocally indicate the pooling of broad, flat water bodies in a distributed system near or at its capacity. This distributed-dominated system then transitions to a channel-dominated system between 50 – 100 km from the terminus. Schroeder et al. (2013) hypothesized this transition to channelized flow occurs through the development of many channels spread across the glacier width, which scatter radar energy and lower specularity; however, our modeling instead suggests that the near-terminus, non-specular zone of Schroeder et al. (2013) depicts a below-capacity distributed system, whose water has been partially evacuated by a small number of large, stable channels. Such a configuration would produce non-specular radar returns due to a rough surface of discontinuous water cavities at a variety of orientations (Figure 2.2).

In such a sparsely channelized system, it is expected that isolated areas of the bed exist in which subglacial lakes may form. Disconnected portions of the drainage network are common beneath alpine and Greenland glaciers, particularly in the summer when channels draw water from the surrounding distributed system, leading to the isolation of poorly connected basal cavities (Andrews et al., 2014; Chu et al., 2016; Gordon et al., 1998; Hoffman et al., 2016; Murray and Clarke, 1995; Rada and Schoof, 2018). Disconnected areas may exist year-round, or may reconnect following a reconfiguration of the channelized system or the collapse of channels in the winter (Hoffman et al., 2016; Rada and Schoof, 2018). However, substantial subannual reshaping of the drainage system should not occur in the

absence of a seasonal melt cycle, like at Thwaites Glacier, and thus parts of the bed may remain disconnected for extended periods of time. This would allow disconnected water to gradually pool into lakes that drain when they periodically exceed their hydropotential seal (Fowler, 1999). Such drainage events could act as similar catalysts for drainage network reconfigurations as the seasonal melt cycles of alpine and Greenland glaciers. Our model lacks the complete physics to properly simulate the filling and draining of subglacial lakes (e.g., Carter et al., 2017); however, it is evident that persistent and extensive subglacial channels can exist concurrently with subglacial lakes beneath Thwaites Glacier, and further work is needed to understand the interaction between the two drainage features.

2.4.2 Implications of Channelization on Thwaites Glacier Dynamics.

2.4.2.1 Channelization and Submarine Melting at the Grounding Line.

The rapid and potentially unstable retreat of Thwaites Glacier is likely driven by enhanced sub-ice-shelf melting (Hoffman et al., 2019; Joughin et al., 2014; Milillo et al., 2019; Rignot et al., 2014; Seroussi et al., 2017; Yu et al., 2018), resulting in part from intruding warm Circumpolar Deep Water (CDW) flowing along bathymetric troughs to the grounding line (Hogan et al., 2020; Milillo et al., 2019; Nakayama et al., 2019). The most rapid retreat (12–18 km between 1992–2011) was recorded at the glacier's central, fast-flowing core (Rignot et al., 2014), where the retreat has continued at a rate of 0.6 km yr^{-1} until at least 2017 (Milillo et al., 2019). Ice shelf submarine melt rates exceed 200 m yr^{-1} at the fast-flowing core, coincident with the recent formation of a prominent sub-shelf cavity (Adusumilli et al., 2020; Bevan et al., 2021).

In all but one of our low-resolution data-compatible FSS runs, both main channels converge near the grounding line directly above the subshelf cavity described in Bevan et al. (2021) (Figure 2.5a–b). In our high-resolution model, one channel intersects the grounding line at this location, while the second reaches the ocean 16 km to the east, also in the region of high subshelf melting (Figure 2.5c). Subglacial discharge plumes, formed from channelized subglacial water entering the ocean, amplify local submarine melting through turbulent heating and the entrainment of deep and often warm water, such as CDW, along the terminus and ice shelf (Asay-Davis et al., 2017; Jenkins, 2011; Slater et al., 2015). While it would be an over-interpretation of our model to regard the exact locations of subglacial channels as reality, the ubiquitous conjunction of large channels (33–106 $m^3\ s^{-1}$) with high subshelf melt rates at the grounding line in all data-compatible scenarios strongly suggests channelized subglacial discharge augments submarine melting in this region. Recent ocean modeling of the Pine Island Ice Shelf cavity supports this assertion, and indicates subglacial discharge localized at the grounding line, and of similar magnitude to what occurs in our model, can explain the local ice shelf melt rates of $\sim$ 200 m yr^{-1} observed at Pine Island Glacier (Nakayama et al., 2021). Similar results have also been reported for the nearby Getz Ice Shelf, where subglacial discharge accelerates subshelf submarine melting by entraining and displacing CDW along the base of the ice shelf (Wei et al., 2020).

Additionally, CDW reaches the Thwaites Glacier grounding line through a series of bathymetric troughs and sills that moderate its flow (Hogan et al., 2020; Nakayama et al., 2019), and it is possible the entrainment of ambient water into subglacial discharge plumes may further enhance CDW flushing of the Thwaites subshelf cavity, similar to the subglacial plume-driven renewal of Greenland fjords

(Carroll et al., 2017; Gladish et al., 2015; Zhao et al., 2021). However, plume-driven buoyancy forcing may only have a minimal effect on cavity circulation beneath the Pine Island Ice Shelf (Nakayama et al., 2021), and thus it could be assumed that the comparable grounding line fluxes given by our model are still too weak to significantly enhance CDW advection to Thwaites Glacier.

2.4.2.2 Implications of Channelization for Effective Pressure and Basal Sliding.

Despite contributing to high ice-shelf basal melt rates and potential loss of ice-shelf buttressing, our model suggests subglacial channels may have a stabilizing effect on basal drag near the grounding line. Effective pressures are 3× higher within 50 km of the grounding line in channel-enabled runs than in distributed-only runs (Figure 2.8d). This region of high effective pressure coincides with a distributed system that is operating below its capacity (Figure 2.3), something not reproducible in distributed-only simulations (Figure 2.8a–c). Only 1–3 principal channels exist within the terminal 100 km; nevertheless, comparison with distributed-only experiments indicates that a small number of channels are still able to efficiently evacuate water from the entire region, due to their lower hydropotential compared to the surrounding area. Higher effective pressure in the terminal 100 km implies higher basal friction, which has been shown to be a leading control on the retreat and mass loss of Thwaites Glacier (Yu et al., 2018) and surface velocities at the neighboring Pine Island Glacier (Gillet-Chaulet et al., 2016; Joughin et al., 2019). High basal shear stress associated with competent bedrock is already thought to exist within 80 km of the grounding line (Joughin et al., 2009), and may work in tandem with channelized subglacial drainage to help buttress against further retreat.

Effective pressures decrease substantially further inland where channelization is minimal. In the upper highly specular area, average effective pressures in data-compatible runs range between 200–600 kPa, almost an order of magnitude less than the near-terminus region (Figure 2.8). Effective pressures in highly specular areas are similar to the -30–150 kPa effective pressures observed at Ice Stream B (Engelhardt and Kamb, 1997), which to our knowledge, remain the only direct observations of effective pressures in West Antarctica.

Smith et al. (2017) noted that the small ($< 10\%$) increase in ice velocity observed after subglacial lake drainage events may indicate an insensitivity of Thwaites Glacier dynamics to its subglacial hydrology. However, the linked subglacial lake drainage event measured by Smith et al. (2017) beneath Thwaites Glacier in 2013–2014 had an average discharge of $160 - 240$ m^3 s^{-1} over 6 months; only 3–5 times greater than modeled channel discharge 50 km from the terminus, and 1–2 times greater than the largest modeled channels at the grounding line. Any pre-existing channels of similar size to those in our model could, therefore, help accommodate the additional flux from lake drainage events, which may explain the relatively minor increase in ice velocity they observed. Thus, this lake drainage event could also be interpreted as evidence of channelized drainage stabilizing glacier dynamics, as is indicated by our model. As Thwaites Glacier continues to thin and retreat, we expect the subsequent changes in glacier geometry and meltwater input to continually reshape its subglacial drainage network. Our results suggest this will alter ice dynamics, and should be taken into account when considering the uncertainty in model projections.

Ice dynamics models have recently started implementing effective pressure-dependent sliding laws supported by current theory. However, a challenging

problem is how to best parameterize effective pressure in order to solve for basal shear stress. A common approach is to approximate effective pressure by assuming a perfect hydrostatic connection with the ocean (e.g., Asay-Davis et al., 2016; Cornford et al., 2020; Leguy et al., 2014; Nias et al., 2018; Yu et al., 2018, and others), shown for our model domain in Figure 2.8a. Effective pressure using an ocean connection assumption is in fair agreement with our channel-enabled runs within 5 km of the grounding line, but is up to an order of magnitude too high further inland, indicating a parameterization based on an open ocean connection may only be realistic near the terminus. This suggests a regularized-Coulomb friction law (e.g., Joughin et al., 2019) may be appropriate for Thwaites Glacier, as it only accounts for effective pressure where effective pressure is low and basal sliding speeds are high, such as near the grounding line (Schoof, 2005). However, our channel-enabled model indicates effective pressure actually decreases between 5–100 km from the grounding line, and maintains its proportionality to basal shear stress throughout the entire domain (Figure 2.8b). This implies basal shear stress stays in the Coulomb regime even within the glacier interior, and thus a yield stress or semi-plastic Budd-type law may work equally well for Thwaites Glacier, as has previously been successful at Pine Island Glacier in reproducing observed surface velocities (Gillet-Chaulet et al., 2016).

To test this hypothesis we attempt to reconstruct our input basal shear stress using a Budd-style friction law of the form: $\tau_b = CN\vec{u}_b^{1/m}$, where $\vec{u}_b$ is a model input, N is solved for by the hydrology model, and C is a tunable basal slipperiness coefficient. Here, m is the bed-dependent stress exponent that is likely between 5–10 for Pine Island Glacier (Gillet-Chaulet et al., 2016; Joughin et al., 2019; Nias et al., 2018), which is assumed to have similar basal properties to

Thwaites Glacier. Figure 2.8b illustrates the results using four plausible values of m and accompanying C values that minimize the root mean square error with the model input. All four versions effectively recover the input basal shear stress, with the best agreement using $m = 5$ or $m = 8$, which is consistent with previous work (Gillet-Chaulet et al., 2016; Joughin et al., 2019; Nias et al., 2018). Therefore, we assert that a Budd-style friction law is appropriate for Thwaites Glacier, assuming accurate knowledge of the effective pressure field. Based on these results we caution against the continued usage of the hydrostatic ocean connection parameterization for effective pressures beyond the marginal 5 km for Thwaites Glacier, which may produce unrealistically slow sliding velocities.

2.4.3 Model Considerations. Our results highlight the need for validation of subglacial hydrology models across the entirety of a glacier. We found a wide range of parameter values resulted in steady-state configurations, and most had some degree of channelization coincident with the location of observed anomalously high sub-ice-shelf melting. However, many simulations had water pressures and discharges that were either too low or too high to be realistic, and without comparison with radar specularity content, it would have been easy to arbitrarily choose the wrong parameters and base our conclusions on an unrealistic model. Borehole validation has been previously attempted for a small alpine glacier (Rada and Schoof, 2018), but the scale of Antarctic and Greenland glaciers makes this unattainable for ice sheets. We therefore suggest that ice-penetrating radar, such as used in this paper and in Dow et al. (2020), or other broad-scale proxies for basal water, is the best approach for validation of ice sheet subglacial hydrology models. While our comparison between R_{wt} and specularity content is somewhat *ad hoc*, it selected for a coherent grouping of parameters, water pressures, and

channel velocities within the expected realistic range, which gives us confidence in its effectiveness. Comparison criteria may need customization to be applicable at other glaciers, but the overall methodology presented in this paper should be beneficial in many settings. Bed conditions differ within and between glacier basins, and we stress our parameter choices should not be extrapolated to other glaciers without validation.

Many assumptions built into subglacial hydrology models remain unsupported, and it is uncertain how such assumptions may influence our results. We therefore deem it necessary to consider the primary underlying simplifications that may impact this paper. Our choice to ignore pressure-dependent melting/freezing in Equation 2.5 neglects the effects of supercooling, which would lead to the abatement of R-channels and the expansion of the distributed system as water flows out of a prominent overdeepening. Supercooling has been shown to decrease channelization in other subglacial hydrology models (de Fleurian et al., 2018). However, the overdeepening within 100 km from the grounding line (Figure 2.1a), in which channelization becomes pronounced, is far from meeting the supercooling threshold of Werder (2016). Furthermore, the upward bed slope in the terminal 100 km is only 60% of the downward surface slope, and should therefore allow for sufficient dissipative heating to continually grow channels (Alley et al., 1998). We therefore do not expect the neglect of Π in Equation 2.5 to significantly affect our conclusions.

Uniform parameterizations of the distributed system do not account for realistic heterogeneity in bed geometry or lithology, both of which can locally influence distributed connectivity (Andrews et al., 2014; Downs et al., 2018; Gordon et al., 1998; Hoffman et al., 2016; Murray and Clarke, 1995; Rada and Schoof,

2018). The bed of Thwaites Glacier is thought to consist of alternating regions of bedrock and glacial till (Holschuh et al., 2020; Joughin et al., 2009; Muto et al., 2019a,1) that could potentially affect the connectivity of the distributed system, and thus conductivity and discharge. Currently, all subglacial hydrology models assume a consistent k_q across their domains, although allowing k_q to vary with bed lithology may account for spatial differences in connectivity and produce more realistic results (Hoffman et al., 2016).

Modeling (Joughin et al., 2009) and seismic data (Muto et al., 2019a,1) suggest bed elevation could serve as a reasonable proxy for bed lithology under Thwaites Glacier, where subglacial till (low conductivity) accumulates in depressions and exposed bedrock (high conductivity) primarily exists at topographic highs. Regions of high specularity content coincide with low-lying troughs, and it is therefore conceivable that imposing a high k_q above these troughs, and low k_q within them, could reproduce the observed specularity content without the need for channelization. However, our results suggest the minimum k_q necessary to prevent channelization would still be high enough over a majority of the domain to drop water pressures below realistic levels. Lowering k_q within troughs, but maintaining the same k_q at higher elevations as used in our data-compatible FSS runs could help pool water into subglacial lakes in till-laden depressions (see Section 2.4.1), but it seems unlikely this would divert enough water to preclude the overall growth of channels in the terminal 100 km. Furthermore, the location of modeled channelized flow at the grounding line presents a convincing explanation for the anomalously high sub-ice-shelf melt rates observed at the same position, something that would be lacking in a purely distributed system. We acknowledge the neglect of a spatially variable k_q could

create some uncertainty in our discharge results, but is likely minimal, and our k_q parameter sweep may already account for this variability.

As described in Downs et al. (2018), the value of k_q used in subglacial hydrology models is a proxy for the connectivity of orifices linking cavities in the bed. Models assume the orifices scale with cavity size; however, in their original conception, orifices behave like small R-channels that may enlarge with turbulent melting (Fowler, 1987; Kamb, 1987). Downs et al. (2018) used this argument to scale k_q with meltwater input, which better captured seasonal water pressures. Although Thwaites Glacier lacks a seasonal meltwater cycle, we could use the same argument to justify use of a different distributed system flow law.

Darcy or Darcy-Weisbach flow laws are used almost ubiquitously in subglacial hydrology models (e.g., de Fleurian et al., 2018; Dow et al., 2020; Downs et al., 2018; Hewitt, 2013,1; Hoffman et al., 2018; Hoffman and Price, 2014; Schoof, 2010; Werder et al., 2013, and others), yet these laws are largely unvalidated in the subglacial environment. Distributed discharge with a Darcy-Weisbach turbulent flow law, as used in this paper, has a $\frac{5}{4}$ power dependency with water thickness. However, in other flow laws, such as Darcy porous media flow or Poiseuille laminar flow, the exponent may vary between 1 and 3 (e.g., Hewitt, 2013,1; Kyrke-Smith and Fowler, 2014; Kyrke-Smith et al., 2014). In practice, the use of a higher exponent could produce similar behavior to a melt-dependent k_q, and could account for a larger connectivity with increased meltwater, driven by the dissipative melting and opening of orifices. Although such a flow law would increase efficiency of the distributed system and potentially minimize channelization, we do not believe its use would dramatically change our results. Water thicknesses using a Darcy-Weisbach law are fairly uniform within 200 km of the grounding line (Figure 2.3c),

which suggests an increased dependency of discharge on water thickness may make little difference in our model.

2.5 Conclusions

This paper leverages observations from a variety of sources to select for the subglacial hydrology model scenarios that are the most likely representations of reality. Our range of possible steady-state scenarios highlights the need for thorough parameter sweeps in subglacial hydrology models, which are then winnowed to the most realistic grouping of simulations based on extensive observations. We emphasize validation of subglacial hydrology models within the glacier interior, and not just at its terminus, is necessary to properly constrain realistic drainage behavior. Furthermore, our work demonstrates subglacial hydrology models still produce a range of results that are compatible with data, and thus model results should be reported as a suite of possible scenarios, instead of one feasible configuration.

Our work presents an updated conceptual model for the subglacial drainage system beneath Thwaites Glacier. Our model indicates a few stable channels exist within 200 km of the grounding line, and coalesce into 1–2 large stable channels within the terminal 50–100 km. These channels intersect the ice-ocean boundary directly at the location of highest sub-ice-shelf melt rates, suggesting they play an important role in frontal ablation and grounding line retreat. However, in the interior of the glacier, subglacial channels efficiently evacuate water from a broad portion of the bed, thereby increasing basal friction within 100 km of the grounding line and potentially buttressing against further retreat. At this point, it remains unclear how common such drainage systems are in Antarctica, or what impact subglacial channels have on sub-ice-shelf cavity circulation and ice dynamics.

We expect the subglacial drainage network to continually reconfigure with future changes in meltwater production and glacier geometry, which will subsequently lead to spatially and temporally evolving basal shear stress and frontal ablation rates. Further work with a fully coupled ice dynamics-subglacial hydrology model will be necessary to determine the exact influence of subglacial channels on future retreat and mass loss.

2.6 Bridge

In Chapter II, I paired the MALI subglacial hydrology model with observations of radar specularity content and sub-ice-shelf melt rates to determine the likelihood of channelized subglacial drainage beneath Thwaites Glacier, West Antarctica, and explore its potential impact on ice dynamics and frontal ablation. In Chapter III, I look at glacial freshwater on the other side of the ice-ocean boundary, and investigate its impact on glacial fjord circulation and heat transport to tidewater glacier termini. This study targets LeConte Bay, Alaska, which serves as an accessible analog to Greenland fjords, but is an interesting location for this study in its own right, as Alaska glaciers were the single largest cryospheric contributors to sea level rise at the beginning of the 21st Century (Gardner et al., 2013).

CHAPTER III

SUBGLACIAL DISCHARGE REFLUX AND BUOYANCY FORCING DRIVE SEASONALITY IN A SILLED GLACIAL FJORD

This chapter was previously published as:

Hager, A. O., Sutherland, D. A., Amundson, J. M., Jackson, R. H., Kienholz, C., Motyka, R. J., Nash, J. D. (2022). Subglacial discharge reflux and buoyancy forcing drive seasonality in a silled glacial fjord. *Journal of Geophysical Research: Oceans*, 127, e2021JC018355. doi: 10.1029/2021JC018355

Author Contributions:

Writing – original draft: Alexander O. Hager

Writing – review and editing: Alexander O. Hager, David A. Sutherland, Jason M. Amundson, Rebecca H. Jackson, Christian Kienholz, Roman J. Motyka

Conceptualization: Alexander O. Hager, David A. Sutherland

Data curation: Alexander O. Hager, David A. Sutherland, Jason M. Amundson, Rebecca H. Jackson, Christian Kienholz, Roman J. Motyka, Jonathan D. Nash

Formal analysis: Alexander O. Hager, Christian Kienholz

Funding acquisition: David A. Sutherland, Jason M. Amundson, Roman J. Motyka, Jonathan D. Nash

Investigation: Alexander O. Hager

Methodology: Alexander O. Hager, Christian Kienholz

*Project Administration:*David A. Sutherland, Jason M. Amundson, Rebecca H. Jackson, Roman J. Motyka, Jonathan D. Nash

Resources: David A. Sutherland, Roman J. Motyka, Jonathan D. Nash

Supervision: David A. Sutherland, Jason M. Amundson, Rebecca H. Jackson, Roman J. Motyka, Jonathan D. Nash

Validation: Alexander O. Hager

Visualization: Alexander O. Hager

3.1 Introduction

Ocean-induced frontal ablation is a dominant driver of ice dynamics and mass loss for tidewater glaciers (Joughin et al., 2012; McNabb et al., 2015; Nick et al., 2009; Smith et al., 2020), and thus sea level rise in the 21^{st} century (Dieng et al., 2017; Gardner et al., 2013). Glacier retreat and acceleration has been observed following warming ocean temperatures (e.g., Holland et al., 2008; Luckman et al., 2015; Motyka et al., 2011; Murray et al., 2010; Straneo and Heimbach, 2013; Wood et al., 2018), yet fjords often regulate the degree of ocean forcing these glaciers experience (Straneo and Cenedese, 2015), as well as the export of glacial freshwater to the coastal ocean (Bamber et al., 2018,1). Near-glacier water properties depend on fjord circulation, which may vary with changes in subglacial discharge (Carroll et al., 2015; Jackson and Straneo, 2016; Sciascia et al., 2013; Straneo et al., 2011; Xu et al., 2012), glacier and iceberg submarine melting (Davison et al., 2020; Jackson et al., 2020; Magorrian and Wells, 2016; Moon et al., 2018), wind forcing (Jackson and Straneo, 2016; Jackson et al., 2014; Moffat, 2014; Moffat et al., 2018), fjord-shelf density gradients (Carroll et al., 2018; Mortensen et al., 2011), and hydraulic control over sills (Schaffer et al., 2020). In this paper, we quantify an additional control on glacial fjord circulation, the sill-driven mixing and recycling of glacial freshwater, and determine its influence on the seasonal variability of fjord circulation and near-glacier water properties when paired with the buoyancy forcing of subglacial discharge plumes.

Fjords are deep estuaries that are often highly stratified (Geyer and Ralston, 2011). Vertical mixing is mostly localized at bathymetric sills (Ebbesmeyer and

Barnes, 1980), or in the case of glacial fjords, within subglacial discharge plumes (Carroll et al., 2015; Jenkins, 2011). Ambient near-glacier water properties are therefore largely determined through the volumes and compositions of inflowing external water, outflowing glacially-modified water, and the degree of sill-driven mixing that occurs between the two. In addition to external forcing mechanisms, sill-driven mixing may also affect the timing and magnitude of deep water (below sill depth) renewal events (e.g., Farmer and Freeland, 1983; Gade and Edwards, 1980; Geyer and Cannon, 1982; Gillibrand et al., 1995), and thus often the advection of external water to the glacier grounding line. For example, sill-driven reflux (the vertical mixing and recirculation) of freshwater may sufficiently freshen inflow so to prevent deep water renewal (Geyer and Cannon, 1982; Gillibrand et al., 1995), or if mixing persists long enough, may freshen ambient fjord conditions to facilitate more frequent renewal events (Gillibrand et al., 1995).

Subglacial discharge buoyancy forcing has recently been identified as an important mechanism for deep water renewal in glacial fjords (e.g., Carroll et al., 2017; Gladish et al., 2015; Zhao et al., 2021). Yet, the strong seasonality of glacial freshwater fluxes (Bamber et al., 2018; Jackson and Straneo, 2016; Moon et al., 2018) implies this renewal mechanism is only active for part of the year. Freshwater reflux is similarly seasonal, and it should be expected that both subglacial discharge reflux and buoyancy forcing drive large changes in stratification, circulation, and heat advection between seasons. However, due to the inaccessibility of many glacial fjords in the winter, few year-round studies have observed the seasonal evolution of silled glacial fjord circulation (e.g., Matthews, 1981; Moffat et al., 2018; Mortensen et al., 2014), and it remains unclear how subglacial discharge and reflux affect heat advection to tidewater glacier termini throughout the year.

Here, we use a suite of observations collected throughout 2016–2017 in LeConte Bay, Alaska, to investigate the seasonal relationship between sill-generated mixing and plume-driven buoyancy forcing in a shallow-silled glacial fjord. We complement our observations with experiments using the Massachusetts Institute of Technology general circulation model (MITgcm) (Marshall et al., 1997), and employ the estuarine Total Exchange Flow (TEF) framework (MacCready, 2011) to calculate reflux fraction at bathymetric sills (Cokelet and Stewart, 1985; MacCready et al., 2021). We find a majority of glacial freshwater is refluxed at the fjord's shallow entrance sill, which when paired with a deep buoyancy source at the glacier terminus, creates a distinct summer circulation regime only feasible in silled, glacial fjords. In the summer, this circulatory cell has two competing effects on heat advection: 1) warm and relatively salty externally surface water is rapidly drawn down a series of sills to the 200 m deep grounding line; however, 2) this inflowing water also undergoes heavy sill-driven mixing with the outflowing plume, thereby cooling substantially upon entering the fjord. We anticipate our results are directly applicable to other shallow-silled glacial fjords throughout Alaska, Canada, and Patagonia, as well as in some fjords in Greenland with the proper geometric constraints.

3.2 Methods

3.2.1 Study Area: LeConte Bay, Alaska. LeConte Bay is a 25 km long, 1 – 2 km wide glacial fjord in Southeast Alaska (Figure 3.1). The fjord contains a series of 4 sills and sub-basins along its length. At the fjord mouth is a 4 km long, 8 – 20 m deep, sill (S1) that modulates exchange flow between LeConte Bay and Frederick Sound (Motyka et al., 2013). Exchange flow across S1 is aided by strong tidal forcing, with mixed semi-diurnal tidal amplitudes ranging between

2.5 and > 6 m (O'Neel et al., 2001). Three more sills (S2, S3, and S4) exist at 12 km, 1.7 km, and <500 m from the LeConte Glacier terminus, with maximum depths of ∼90 m, ∼180 m, and ∼170 m, respectively. Sub-basins (B1 – B4) reside between sills, and range in depths from ∼135 m to ∼320 m (Figure 3.1c). During our study period, the depth of the glacier grounding line was ∼ 200 m, deeper than any of the four sills. A subglacial discharge plume was observed near the southern extent of the glacier terminus throughout both summers of 2016–2017 (Kienholz et al., 2019; Sutherland et al., 2019); however, plumes have occasionally been observed near the northern terminus in other years (Motyka et al., 2013).

3.2.2 Shipboard Data Collection and Processing. Shipboard observations consist of hydrographic and water velocity data from six field surveys during March/April 2016 – September 2017. We conducted three extensive shipboard surveys in August 2016, May 2017, and September 2017 with instrumentation on two separate vessels, the MV Pelican and MV Steller, sampling concurrently. Three additional surveys in March 2016, October 2016, and July 2017 used only the MV Pelican. Shipboard temperature, salinity, and pressure data were collected using a vertical microstructure profiler (VMP; Rockland Scientific VMP-500) and conductivity, temperature, and pressure profilers (CTDs; Seabird 19plus and RBRconcerto), and were vertically averaged into 1 m bins. CTDs and the VMP were cross-calibrated at the beginning of each survey period. Two acoustic Doppler Current Profilers (ADCPs; 600 kHz and 150 kHz Teledyne Workhorse) were mounted on the MV Pelican, and a 300 kHz ADCP (Teledyne Workhorse) was mounted on the MV Steller. All ADCPs were operating continuously during CTD sampling to obtain concurrent hydrography and velocity profiles. The 600 kHz, 300 kHz, and 150 kHz ADCP data were vertically averaged into 2 m, 5 m,

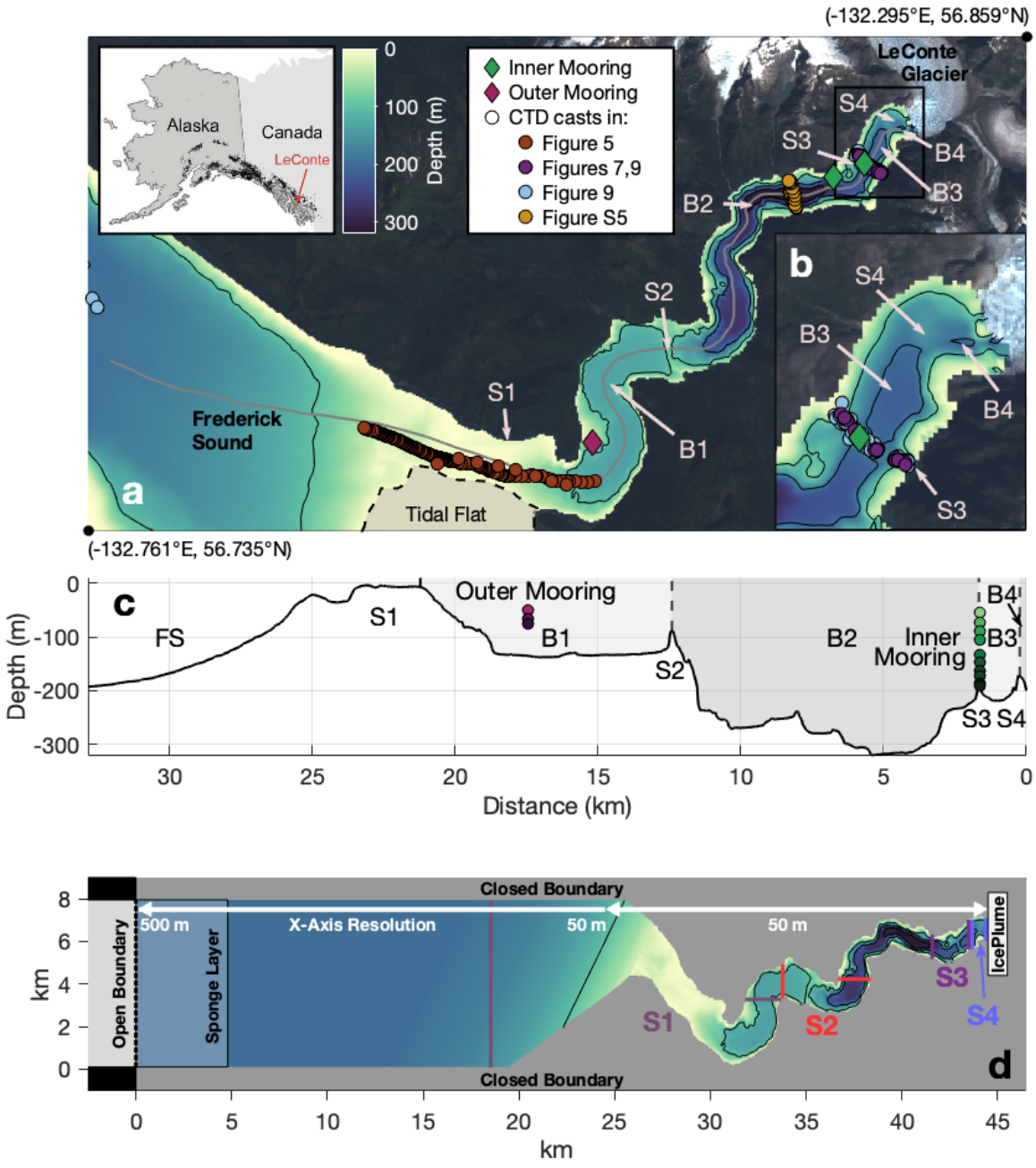

Figure 3.1. **(a)** Bathymetric map of LeConte Bay, including the locations of sills, sub-basins, moorings (including both Inner Mooring locations), and shipboard CTD casts from subsequent figures. **(b)** Zoom-in of the black box in **a**. **(c)** Thalweg bathymetry along gray line in **a**, including sills, sub-basins, and locations of all mooring instruments. Instrument colors coincide with Figure 3.3. **(d)** MITgcm model domain including the locations of the TEF efflux/reflux transects bracketing each sill. Contours in **a**, **b**, and **d** are at 100 m intervals.

and 6 m bins, respectively, and horizontally averaged into 30 m bins. We removed data within the bottom 15% of the water column, and within 4 m, 5 m, and 10 m of the surface for the 600 kHz, 300 kHz, and 150 kHz ADCPs, respectively. We also set an autocorrelation threshold for each beam, and removed all data with a signal to noise ratio of less than 110 (out of 128). Binned data from consecutive pairs of across-fjord ADCP transects were averaged together to improve their reliability.

3.2.3 Mooring Data Collection and Processing. Two moorings were deployed in LeConte Bay during our study period. The Inner Mooring contained 11 temperature, salinity, and/or pressure sensors (RBRsoloD, RBRsoloT, RBRduo, Seabird SBE56, Seabird SBE37 MicroCAT) between 58 m – 200 m depth (Figure 3.1b). Iceberg coverage precluded any shallower instrumentation. We stationed the Inner Mooring 2.8 km from the glacier terminus between March and August 2016, then relocated it to 1.9 km from the terminus until September 2017 (Figure 3.1a). The Outer Mooring was located 18 km from the glacier terminus between August 2016 – September 2017, and was equipped with four temperature, salinity, and/or pressure instruments (Onset HOBO PT, RBRsoloT, Seabird SBE37 MicroCAT) between 47 m and 78 m depth (Figure 3.1). Hydrographic instruments on all moorings sampled at 1 second to 30 minute intervals, and the data was later interpolated to 15 minutes. Short gaps exist in all mooring data in August 2016 and May 2017 when the instruments were retrieved for servicing. Salinity time series were filtered to remove significant outliers (five standard deviations from a moving mean). Additional data gaps resulted from instruments losing power or behaving erratically.

3.2.4 Modeled Subglacial Discharge. Glacial runoff during our study period was modeled using an enhanced temperature index model (Hock,

1999), coupled with an accumulation model and linear reservoir-based discharge routing model (Hock and Noetzli, 1997). Modeled runoff is a product of all glacial meltwater and liquid precipitation in the glacier watershed. To account for poorly constrained parameters, we generated high, medium, and low run-off scenarios, where the medium scenario used a parameter combination that minimizes the root mean square error between modeled and observed specific mass balance measurements. The model was previously published in Sutherland et al. (2019) and Amundson et al. (2020), which include further details of its implementation.

3.2.5 MITgcm Setup and Experiments. We used the Massachusetts Institute of Technology general circulation model (MITgcm) (Marshall et al., 1997) to calculate the reflux of plume water at each sill, and to fill observational gaps needed for hypothesis testing. Experiments were designed to resemble either winter or summer fjord conditions, and were forced with either spring or neap tides, along with a range of subglacial discharge rates typical of each season.

Model bathymetry was constructed using data from a 5 m resolution multibeam echosounder (Reson SeaBat 7111) survey in August 2016, with data gaps filled in using two 20 m resolution fathometer (Furuno 528L) surveys in August 1999 and September 2000 (Eidam et al., 2020). Observed fjord bathymetry was then interpolated onto the 50 m x 50 m model grid (Figure 3.1d). Outside of S1, we constructed an artificial 25 km extension to the domain with similar depth (200 m) and width (8 km) as Frederick Sound. Resolution in the x-direction of the extended domain telescopes from 50 m at S1 to 500 m at the open boundary on the western extent. A sponge layer 10 grid cells (4.8 km) thick existed along the open boundary to mitigate reflection of internal waves back into the domain.

Fjord bathymetry was rotated 49° clockwise to best fit onto a rectangular grid and minimize the number of dry cells. Vertical resolution of our model was 2.5 m in the upper 20 m, 5 m at 20 – 90 m depth, 10 m at 90 – 200 m depth, and 25 m at 200 – 325 m depth.

Idealized tides were implemented by imposing an oscillating tidal velocity along the open boundary, and were tuned so that the amplitudes of tidal pressure variations resemble those observed at the Inner and Outer Moorings. Experiments were forced with symmetric semidiurnal tides with a constant amplitude of 5.5 m or 2.8 m to reflect typical spring or neap tides, respectively. We used shipboard θ/S profiles from March/April and August 2016 to initialize our winter and summer experiments, respectively.

We grouped θ/S profiles measured into six regions: Frederick Sound, S1, B1, B2, B3 and B4, then initialized our model with the observed maximum and mean θ and S profiles, respectively, in each (Figure C.1). Any resultant θ/S gradients between regions were smoothed during the spin-up process. For each season, we spun-up the model with neap tidal forcing until reaching steady state (defined as the point when TEF salt fluxes converge to constant values), then restarted with either neap or spring tides, and ran the model until it re-equilibrated to a quasi-steady state. A quasi-steady state was typically reached within 20 or 30 days of model time for summer and winter runs, respectively.

Subglacial discharge and submarine melt were parameterized using the IcePlume Package (Cowton et al., 2015) using a straight glacier terminus on the eastern extent of our domain (Figure 3.1d). We forced the model with a subglacial discharge plume at 200 m depth on the south side of the terminus, which is consistent with multibeam sonar surveys (Sutherland et al., 2019) and time-

lapse photography (Kienholz et al., 2019) conducted during our study period. For summer experiments, neap and spring tide scenarios were each run with constant subglacial discharge forcing of either 150 $m^3\ s^{-1}$, 250 $m^3\ s^{-1}$, or 350 $m^3\ s^{-1}$ (Table C.1). We neglected subglacial discharge in the winter formulation. We used a line-plume parameterization (Jenkins, 2011) considering a channel width of 100 m, which was based on estimates of plume geometry and discharge during our August 2016 survey (e.g., Jackson et al., 2017). Individual line-plume length is limited by horizontal grid resolution (50 m), so the 100 m long line-plume consists of two adjacent 50 m line-plumes, with the total discharge split evenly between the two. This approach generates the desired entrainment rate of a 100 m line-plume, although interaction between the plumes may make flow nearest to the terminus unrealistic. A small ($\sim 10^{-4}$) negative velocity was evenly imposed across the open boundary to compensate for the volume of water entering the domain. We tuned the IcePlume background water velocity to 0.9 m s^{-1} for our summer experiments to increase ambient submarine melting so that the area-averaged melt rate resembled the observed rate of 8 – 8.5 m d^{-1} (Jackson et al., 2020; Sutherland et al., 2019). This was necessary because standard theory significantly underpredicts ambient submarine melting at LeConte Glacier (Jackson et al., 2020). Part of the discrepancy between theory and observations is caused by plume-driven horizontal circulation along the ice face (Jackson et al., 2020; Slater et al., 2018), so in our winter runs where no plume exists, we dropped the background velocity to the default value of 0.1 m s^{-1}, although we lack observational constraints on this value.

All experiments were run in a hydrostatic configuration with a nonlinear free surface, 4 second time steps, and a Coriolis frequency of $1.22 \times 10^{-4}\ s^{-1}$.

We prescribe horizontal eddy viscosities according to a Smagorinsky scheme (Smagorinsky, 1963), using a Smagorinsky constant of 2.2. The nonlocal K-Profile Parameterization scheme (Large et al., 1994) was used to parameterize vertical mixing, with a background and maximum viscosity of 5×10^{-4} m^2 s^{-1} and 5×10^{-3} m^2 s^{-1}, respectively. We set diffusivities to zero, although some numerical mixing still exists due to advective truncation errors. All reported model output is averaged over one day of model time. Information regarding model validation can be found in Appendix C.

3.2.6 MITgcm TEF Plume Reflux Calculations. Following the work of MacCready et al. (2021), we calculate recirculation of the outflowing plume by coupling TEF (MacCready, 2011) to efflux/reflux theory (Cokelet and Stewart, 1985), which quantifies the net effect of mixing in estuaries without the need to resolve the mixing itself. Their framework assumes an estuarine system where turbulent mixing between inflowing and outflowing layers primarily occurs at constrictions, such as sills, that are separated by deep, advection-dominated basins, where mixing is negligible. Across each mixing zone, some portion, the efflux, of each layer will be transported to the next basin, while the remainder, the reflux, will be vertically transported to the opposing layer and recirculated to its original basin (Figure 3.2).Through mass and volume conservation, this process can be written as:

$$\begin{aligned} \alpha_{21} Q_1 + \alpha_{24} Q_4 &= Q_2 \\ \alpha_{21} S_1 Q_1 + \alpha_{24} S_4 Q_4 &= S_2 Q_2 \\ \alpha_{31} Q_1 + \alpha_{34} Q_4 &= Q_3 \\ \alpha_{31} S_1 Q_1 + \alpha_{34} S_4 Q_4 &= S_3 Q_3 \end{aligned} \tag{3.1}$$

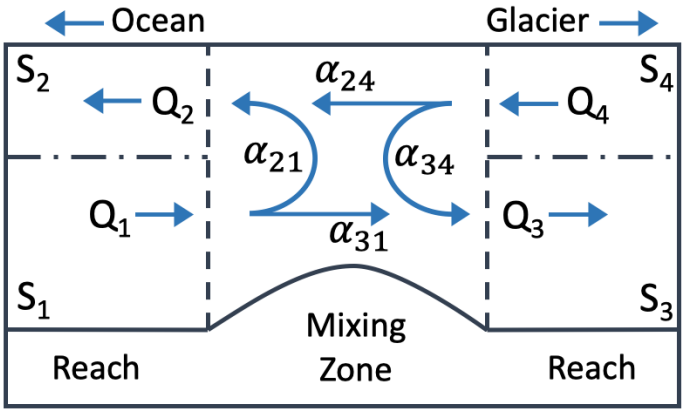

Figure 3.2. Schematic illustrating the different variables in efflux/reflux theory across a sill-generated mixing zone.

where S_i and Q_i are tidally-averaged flux-weighted salinities and tidally-averaged volume fluxes, respectively. Subscripts designate transport layers, where layers 1 and 2 are the inflowing and outflowing layers oceanward of the mixing zone, respectively, and layers 3 and 4 are the inflowing and outflowing layers glacierward of the mixing zone, respectively (Figure 3.2). α_{ij} represents the percentage of layer j that mixes into layer i. The solutions to 3.1 are:

$$\begin{aligned} \alpha_{21} &= \frac{Q_2}{Q_1}\frac{S_2 - S_4}{S_1 - S_4} & \alpha_{31} &= \frac{Q_3}{Q_1}\frac{S_3 - S_4}{S_1 - S_4} \\ \alpha_{24} &= \frac{Q_2}{Q_4}\frac{S_1 - S_2}{S_1 - S_4} & \alpha_{34} &= \frac{Q_3}{Q_4}\frac{S_1 - S_3}{S_1 - S_4}. \end{aligned} \tag{3.2}$$

In this framework, conservation of mass and volume require:

$$\begin{aligned} \alpha_{21} + \alpha_{31} &= 1 \\ \alpha_{24} + \alpha_{34} &= 1 \end{aligned} \tag{3.3}$$

and

$$\begin{aligned} S_4 \leq S_2 < S_1 \\ S_4 < S_3 \leq S_1. \end{aligned} \tag{3.4}$$

In this study, we are primarily concerned with α_{34}, the reflux of the outward flowing plume back into the fjord at each mixing zone.

As with MacCready et al. (2021), we calculate S_i and Q_i using the TEF framework (MacCready, 2011), which satisfies the Knudsen Relations and accounts for both tidal and subtidal transports (Burchard et al., 2018; Knudsen, 1900; MacCready, 2011). TEF transports are the horizontal equivalent of the efflux/reflux vertical fluxes, and are thus the compatible framework for quantifying exchange flow (MacCready et al., 2021). Salt and volume fluxes across a given TEF transect are divided into 1000 discrete salinity classes, and are then tidally-averaged using a 24-24-25 hr Godin filter. We calculated inward and outward transports using the dividing salinity method, an updated methodology for calculated TEF quantities that allows for multiple inflowing and outflowing layers, and has been shown to provide accurate results even in weakly stratified water (Lorenz et al., 2019; MacCready et al., 2018). The sum of all inflowing and outflowing salt and volume fluxes are given as $F_{in,out}$ and $Q_{in,out}$, respectively, and the associated flux-weighted salinities are $S_{in,out} = F_{in,out}/Q_{in,out}$.

We defined TEF transects on either side of each of the four sills (Figure 3.1d), which we assume to be the primary locations of mixing in LeConte Bay, apart from the subglacial discharge plume. Transects were parallel to either the x or y axis, and we used the corresponding perpendicular velocity, v or u, for our flux calculations. TEF transports were then substituted into Eq. 3.2, using $Q_{in} = Q_1$ and $Q_{out} = Q_2$ for the transect oceanward of the mixing zone, $Q_{in} = Q_3$ and $Q_{out} = Q_4$ glacierward of the mixing zone. The same substitution is done for $S_{in,out}$. As done in MacCready et al. (2021), we made minor adjustments to the TEF transports prior to calculation of Eq. 3.2 so that Eqs. 3.1, 3.3, and 3.4 are satisfied. This step is necessary because TEF budgets are not exact, and some drift in salinity may occur within each section (MacCready et al., 2021). An error was

assigned to each variable equal to the difference that it was adjusted, and the error was then propagated through Eq. 3.2. The net error on α_{ij} due to these corrections amounted to no more than 0.3% of the reported value, although it was typically much lower.

Parameterization of melting icebergs has only recently been implemented in the MITgcm (Davison et al., 2020), and we have inadequate fjord-scale coverage of iceberg prevalence to include it in our model. Still, iceberg melt is likely the primary freshwater source in the winter, and its neglect in our model may lead to spurious TEF results in the winter. We therefore limit our winter TEF budgets to one neap tide experiment, which we expect underestimates actual reflux values, due to the decreased baroclinic volume fluxes and increased salinity throughout the fjord (Davison et al., 2020).

3.2.7 Observed Inflow Composition. Although we lack the proper spatial and temporal data coverage to undertake efflux/reflux theory with our observations, we can use standard mixing equations to arrive at similar results. The shallow depth of S1 allows only the uppermost Frederick Sound water to enter LeConte Bay each tidal cycle, during which we expect some amount of mixing to occur across each sill with the outflowing plume (the combined outflow of subglacial discharge, entrained ambient fjord water, iceberg melt, and surface runoff). Assuming these two end-members remain constant for the duration of a field campaign, and that no other water masses significantly contribute to the inflow, we can use conservation of mass, salt, and temperature to write the inflowing θ/S properties as a mixing product of Frederick Sound (fs) and plume

(plm) water:

$$\begin{aligned} \chi_{fs} + \chi_{plm} &= 1 \\ \chi_{fs} S_{fs} + \chi_{plm}\, S_{plm} &= S_{in} \\ \chi_{fs} \theta_{fs} + \chi_{plm}\, \theta_{plm} &= \theta_{in} \end{aligned} \tag{3.5}$$

where χ is the fraction of Frederick Sound or refluxed plume water within a water parcel in the glacierward flow. Equations 3.5 can be rearranged to solve for χ_{plm}:

$$\chi_{plm} = \frac{S_{fs} - S_{in}}{S_{fs} - S_{plm}}. \tag{3.6}$$

We use CTD and ADCP data from August 2016 at repeated transects across S3, together with CTD casts in Frederick Sound (Figure 3.1) to calculate (θ_{plm}, S_{plm}) and (θ_{in}, S_{in}) (other surveys lacked adequate data in Frederick Sound). For each transect, we used the 150 kHz ADCP to isolate the plume (defined as outflowing water within the -0.03 m s^{-1} contour in contact with the maximum outward surface velocity) from the inflow, then found the mean (θ_{plm}, S_{plm}) across all transects. As only the shallowest Frederick Sound water can pass over S1, we averaged only the upper 29 m of Frederick Sound CTD casts to determine (θ_{fs}, S_{fs}). This is the depth of the 90% contour of the Frederick Sound passive tracer remaining in Frederick Sound at the end of our neap tide MITgcm scenarios (the tidal phase during the August 2016 survey).

For each transect, we then calculate the net, volume flux-weighted percentage of plumewater in the inflow:

$$X_{plm} = \frac{\int_A \chi_{plm}\, u'\, dA}{\int_A u'\, dA} \qquad \text{for} \quad u' > 0 \tag{3.7}$$

for glacierward baroclinic velocity u' and cross-sectional area A. This calculation requires extrapolating χ_{plm} and u' to the sides, bottom, and surface of the fjord. To ensure conservation of volume, we follow similar steps to Sutherland et al. (2019)

in which we extrapolate to the surface assuming constant shear, then arbitrarily add the missing volume flux uniformly 1) to all depths, 2) to the inflow at 50 m – 165 m depth, 3) to the intensified inflow at 125 m – 165 m depth, or 4) to the surface layer at 0 – 50 m. The range in these scenarios is then incorporated into the uncertainty in X_{plm}, together with the uncertainty in χ_{plm}.

3.3 Results

3.3.1 Observed Seasonal Stratification and Circulation

Regimes. Shipboard and mooring data depict two dominant stratification and circulation regimes in LeConte Bay: 1) a winter regime (November - March) with a weak two-layer exchange flow that occurs when subglacial discharge is negligible, and 2) a highly stratified, three-layer summer regime (mid June - mid September) when mean subglacial discharge is between 150 - 400 m^3 s^{-1} (Figures 3.3, 3.4). Two short transitional periods in spring (April – mid June) and fall (mid September – October) bridge these two regimes, and represent the establishment or destruction of stratification, coincident with the initiation or cessation of subglacial discharge, respectively.

3.3.1.1 Seasonal Water Properties and Stratification. Mooring and CTD θ/S data revealed that water properties were largely homogeneous both vertically and horizontally throughout most of the winter (Figures 3.3 and 3.4). Both moorings had only minor salinity fluctuations throughout November – March, except for a gradual increase of ∼1.5 psu measured at all instruments (Figure 3.3). The entire fjord experienced fortnightly temperature cycles reflecting spring/neap tidal forcing, which were superimposed over a general cooling trend of $\sim$ 3°C throughout the winter. CTD casts from late winter (March/April 2016) depict a cold, fresh surface layer in the upper 10 m that transitioned into a continuously

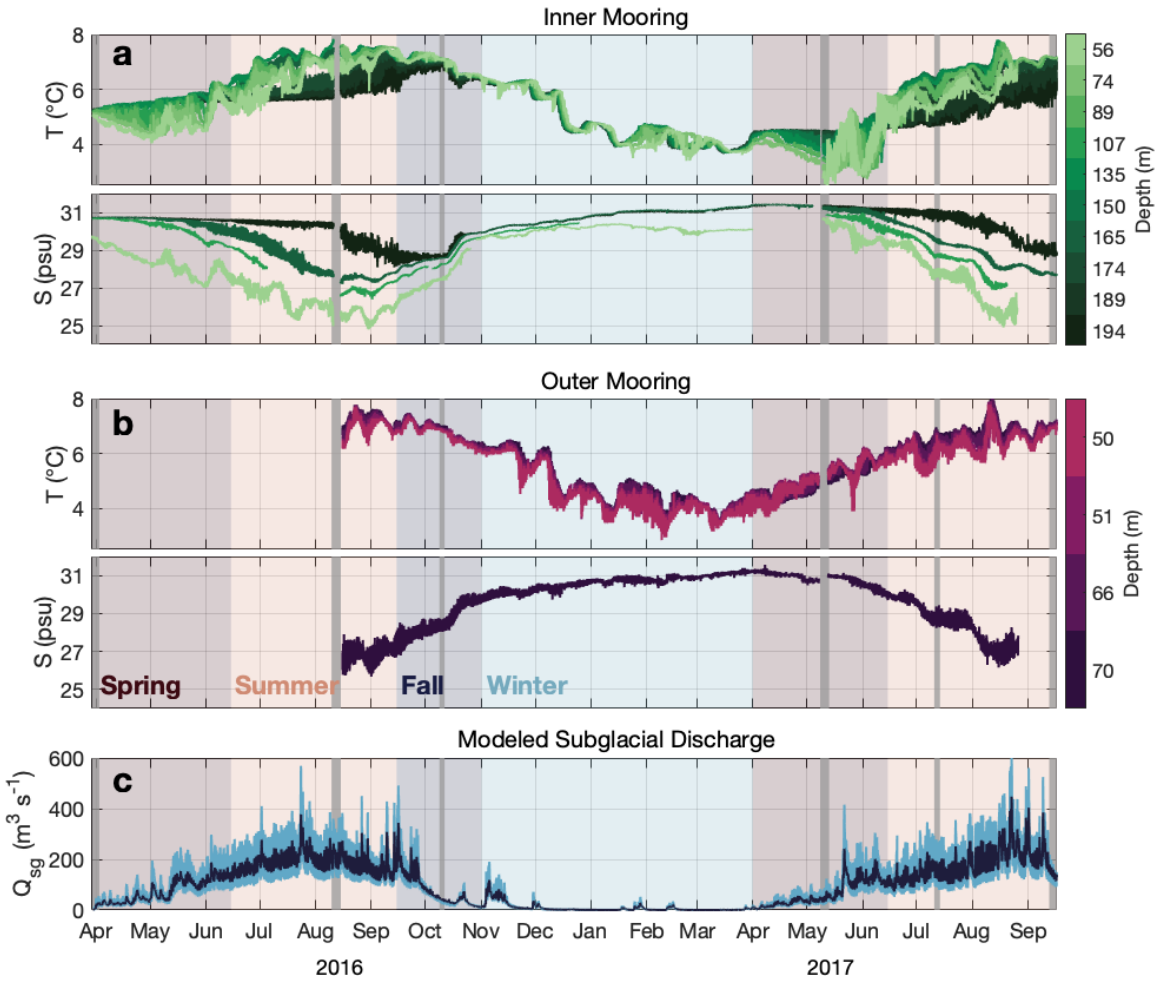

Figure 3.3. Temperature and salinity time series from **(a)** the Inner Mooring and **(b)** the Outer Mooring, color-coded by depth of each instrument. The Inner Mooring comprised of ten temperature instruments, four of which also recorded salinity. All four Outer Mooring instruments measured temperature, and one also recorded salinity. **(c)** Modeled subglacial discharge for our study period, depicting the range in runoff scenarios in light-blue, and the medium runoff scenario in dark-blue. Gray bars in **a**–**c** indicate shipboard surveys. Background colors demarcate the four seasonal regimes and transitional periods.

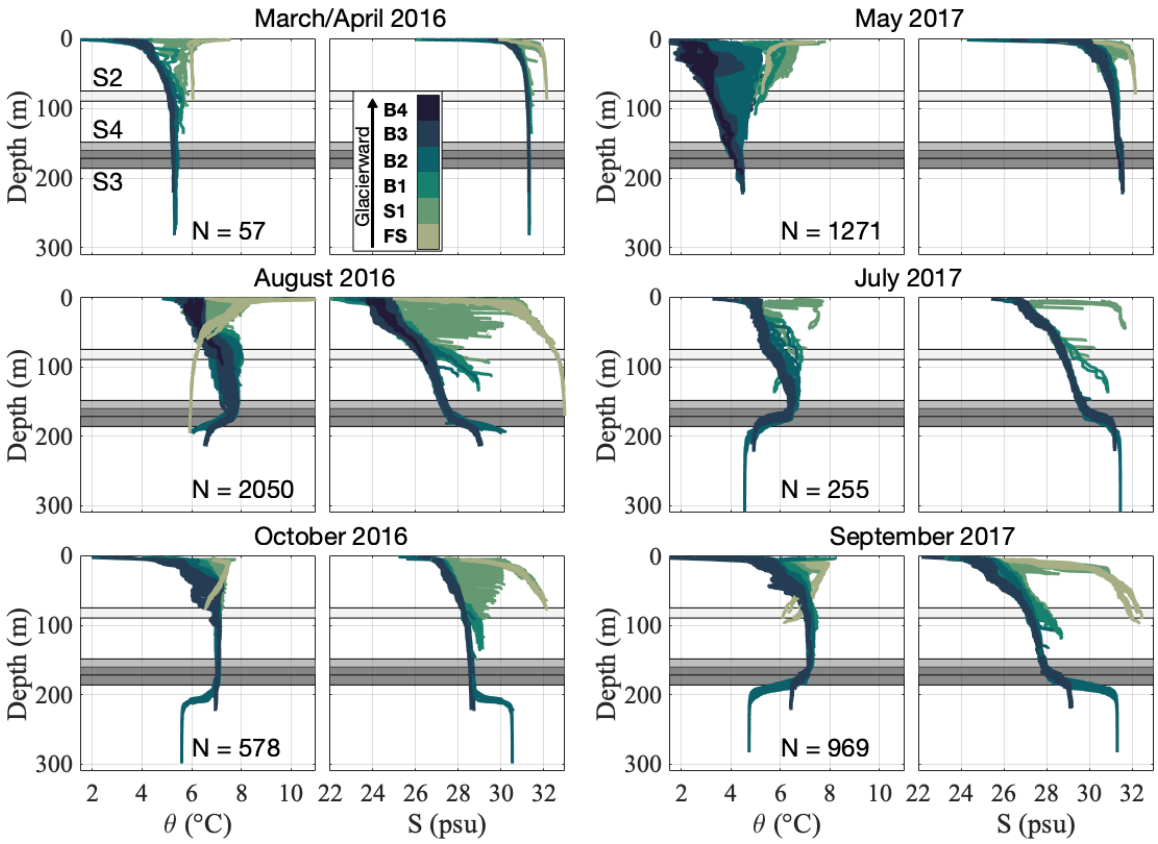

Figure 3.4. θ/S data from all CTD casts during each field campaign, color-coded by location in Frederick Sound (FS), over S1, or within in each sub-basin. Horizontal gray bars depict the depths of S2, S3, and S4.

stratified water column until 100 m depth, below which was nearly homogeneous water (Figure 3.4a). Despite the weak horizontal gradients within the fjord, winter θ/S properties differed by an average of ~ 3.5°C and 1 psu across S1.

Stratification started to develop almost immediately upon the onset of subglacial discharge in early April of both years, marking the beginning of the spring transitional period. In 2017, Inner Mooring temperatures cooled between 50 – 130 m throughout April, while Outer Mooring temperatures warmed (Figure 3.3). This opposing behavior created a large along-fjord temperature gradient across B2 in the upper 150, although along-fjord salinity gradients remained negligible

(Figure 3.4). At this time, a warm glacierward intrusion was observed at 25–50 m depth in B2 (Figure C.5). In early/mid-May, Inner Mooring temperatures started their annual warming trend, reaching similar temperatures to the Outer Mooring by late May to early June. Warming at the Inner Mooring began with its shallowest sensors and gradually deepened to ∼165 m, where the warmest water resided by the end of the transitional period. Below this depth, temperatures remained fairly constant.

Summer stratification began in mid-June of both years, and marked the development of a highly stratified, three-layer system, as seen in all of our summer surveys (August 2016, July 2017, September 2017; Figure 3.4). The upper $\sim$ 50 m of the water column was a relatively cold (5–6°C) and fresh (24–27 psu) surface layer. A pycnocline at $\sim$ 50 m separates this layer from a warm (6–8°C) water body at 50–165 m. The warmest water in the fjord was within this layer and consistently occurred between 120–165 m depth. A prominent second pycnocline existed in B2 and B3 at 165–185m, which coincided with the depths of S3 and S4 (Figures 3.4, S3). CTD surveys conducted at different months of the summer show this pycnocline strengthened throughout the summer, as overlying water freshened and warmed. Below the 165–185m pycnocline rests a third water mass with the same θ/S properties as winter deep water. In the shallower B1 basin, a less dramatic pycnocline at $\sim$ 90 m, corresponding to the depth of S2, separated the middle layer from a saltier and colder bottom layer (Figure 3.4). As a result of the 90 m and 165–185 m pycnoclines, water properties bifurcated at each sill (S2-S4), so that water below sill depth was warmer and fresher on its glacierward side.

Large internal tides were recorded at the Inner Mooring within and just below the 165 – 185 m pycnocline (Figure C.4) that amplified throughout the

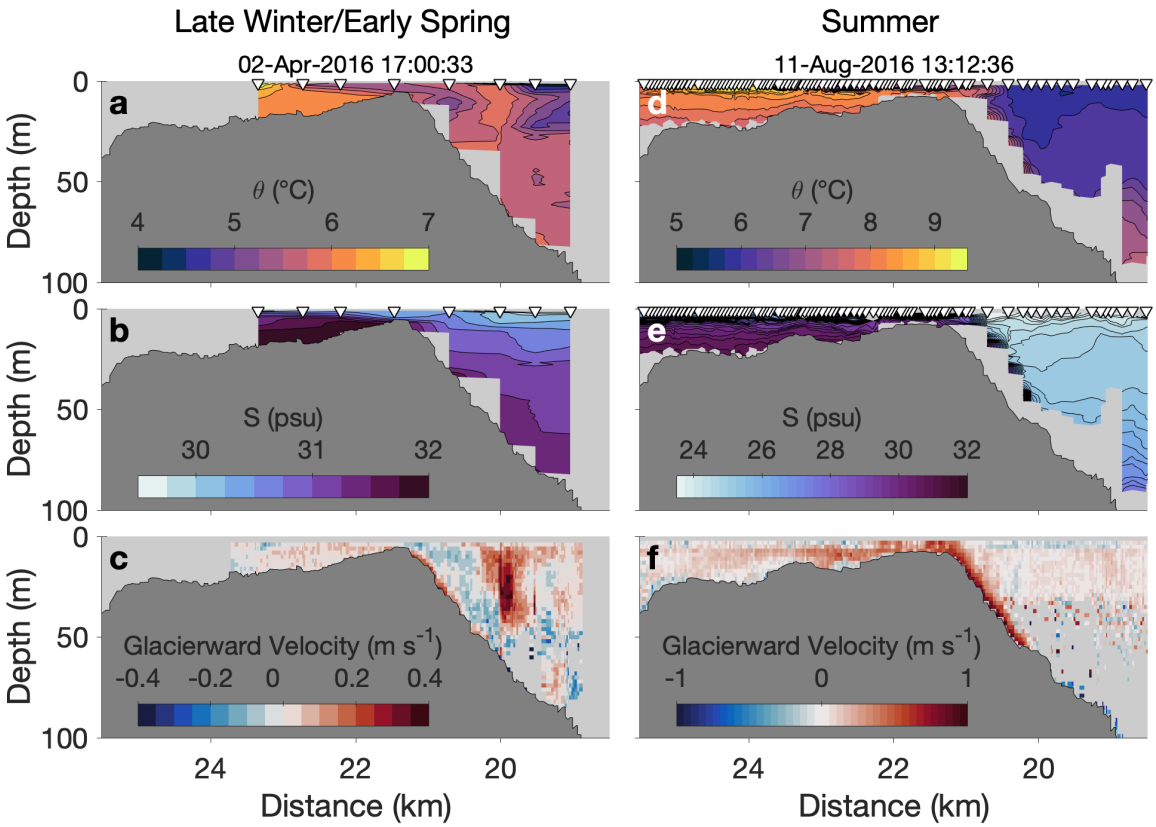

Figure 3.5. Shipboard CTD and ADCP transects over S1 from late winter/early Spring (April 2016) and summer (August 2016). Both transects were measured during neap flood tides, and the median time of each transect is given. White triangles in **a**–**b** and **d**–**e** mark the location of each CTD cast, which are also shown in Figure 3.1. Note the differing color-scales between surveys. View is to the north (Frederick Sound to the left and LeConte Bay to the right).

summer as the pycnocline strengthened. At their largest, these internal tides created semi-diurnal fluctuations of up to 1.5°C and 1 psu, indicating a maximum wave height of 35 m.

3.3.1.2 Seasonal Circulation. External water enters LeConte Bay from Frederick Sound via unidirectional flow over S1 each flood tide. Warm, dense Frederick Sound water then propagates down the lee-side of S1 as a gravity current upon entering LeConte Bay (Figure 3.5). During our March/April 2016 survey, a salinity difference of 1 psu between external and ambient water resulted in a

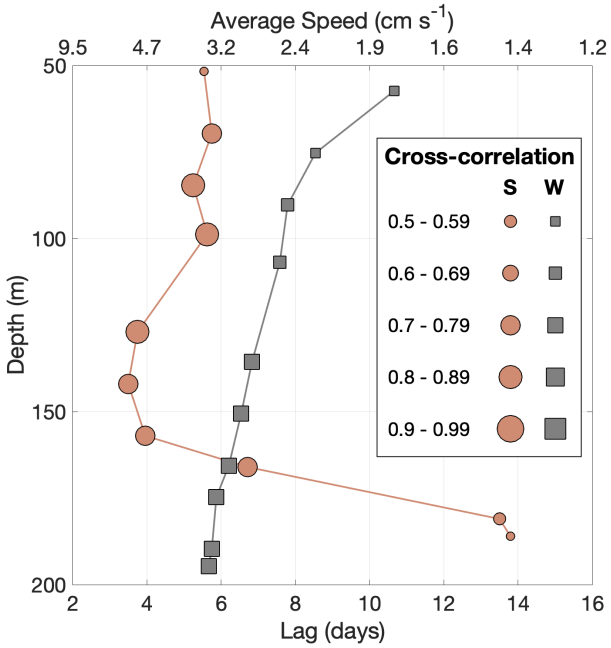

Figure 3.6. Time-lagged cross-correlations between each of the Inner Mooring temperature sensors and the uppermost Outer Mooring temperature sensor (50 m). Markers indicate the lag time (and inferred travel speed) with the highest correlation for each sensor. Circles and squares represent mooring data summer (Jun. 15 – Sept. 15) 2017 and winter (Nov. 1 – Mar. 31) 2016–2017, respectively. Marker size scales with maximum correlation of each instrument. All correlations are significant.

gravity current of $\leq$ 0.5 m s^{-1}, which formed a hydraulic jump upon reaching neutral buoyancy at ∼50 m depth. In contrast, fresher ambient fjord conditions (and an across-S1 salinity difference of 6 psu) in August 2016 created flood tide gravity currents that traveled up to 1 m s^{-1} to a depth beyond the range of our ADCP (Figure 3.5); however, CTD casts suggest these flows reached neutral buoyancy near the 90 m pycnocline in B1.

To determine the fate of water after it enters LeConte Bay, we used time-lagged cross-correlations between the Inner Mooring temperature sensors and the Outer Mooring temperature sensor deployed at 50 m depth (based on the MITgcm experiments, all flow to the Inner Mooring sensors would have first traveled near

this instrument). As salinity largely controls fjord density, temperature is the better tracer of water masses, and the larger number of temperature sensors on each mooring greatly increases vertical resolution. Cross-correlations were calculated between instruments at lag intervals of one hour, and we report only the lag time with the strongest correlation (cross-correlations had only one significant maximum). In the winter, the deepest Inner Mooring sensor had the strongest correlation with the Outer Mooring (r = 0.73). This sensor also recorded the shortest lag time between moorings (5.7 days), implying an average travel speed of 3.3 cm s^{-1} between moorings (Figure 3.6). Correlations decreased and lag times increased for each successively shallower sensor in the water column. During the summer of 2017, the three shortest lag times of 3.7 – 4 days, suggesting mean speeds of 4.6 – 5.2 cm s^{-1}, were recorded between 125 – 160 m depth, just above the 165 – 185 m deep pycnocline. This depth also coincided with the warmest water observed in the summer Inner Mooring record and CTD surveys. Below the pycnocline, lag times dramatically increased with depth to >14 days. Lags in the upper inflowing layer, between 50 – 100 m depth, varied from 5.4 – 5.9 days, suggesting mean travel speeds of 3.2 – 3.4 cm s^{-1}. All temperature sensors between 70 and 166 m depth exhibited moderate to strong correlations (r >0.7) between moorings.

Figure 3.7 depicts typical across-fjord transects over S3 from March/April 2016 and August 2016, and illustrates the main differences between the winter and summer circulation regimes. In the winter, a weak estuarine exchange flow existed within the surface layer, including a small outward flowing plume on the north bank of the fjord. The plume was compensated primarily by surface inflow along the fjord's south side, as well as slow-moving, homogeneous water at depth. Note

that some subglacial discharge was present during this survey, which contributed to the plume's volume. Conversely, surface exchange flow in the summer occurred in the upper 50 m, and instantaneous water velocities were approximately 2 – 3 times greater than in winter. Again, the outflowing plume was located on the fjord's north bank, and was partly compensated by an estuarine exchange flow to the south. However, a comparable inflow existed 120 – 165 m deep that contains the warmest ($< 8°C$) water observed at the Inner Mooring and in all summer CTD casts. This is also the depth where the shortest lags were calculated in mooring cross-correlations. In August 2016, the surface exchange flow in the upper 50 m and the heightened inflow at 120 – 165 m each accounted for 29% of the inflowing volume flux at S3, despite occupying only 13% and 10% of the cross-sectional area, respectively. Just below the intensified, warm inflow is the 165 – 185 m pycnocline, which is obscured in Figure 3.7 by S3 bathymetry, but visible in Figure C.5.

3.3.2 MITgcm Fjord Circulation. Modeled water velocities largely agreed with observations and provide insight to fjord-scale circulation (Figure 3.8). In winter experiments, unidirectional tidal flows forced Frederick Sound water into LeConte Bay, creating gravity currents of similar speed ($\sim$0.5 m s^{-1}) to those observed (Figures 3.8c and 3.5c). In the poorly stratified winter water column, weak gravity currents then propagated down S1 and S2 to the floor of B2 ($\sim$ 320 m), renewing the deepest fjord water first before the overlying water column (Figure 3.8, Movie S1). This circulation style agrees with evidence from mooring cross-correlations, and tidally-averaged model velocities were of similar magnitude to those estimated from correlation lag times. The modeled tidally-averaged outflow was deeper than the surface exchange observed in March/April

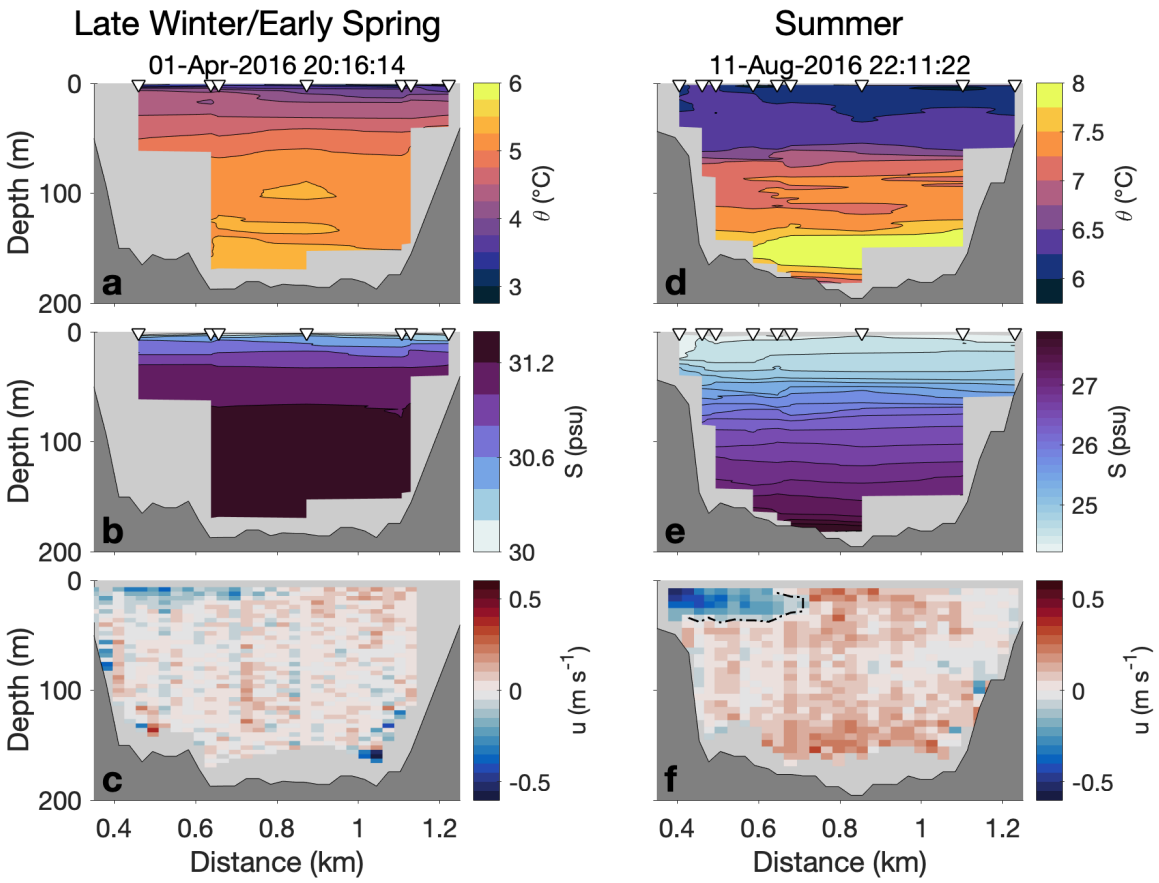

Figure 3.7. Shipboard CTD and ADCP transects along S3 in late winter/early spring (April 2016) and summer (August 2016), both measured during neap ebb tides (median time of each transect is given). Positive velocities are glacierward. The -0.03 m s^{-1} contour used to distinguish the plume in our observed reflux calculations is shown in **f**. White triangles in **a**–**b** and **d**–**e** mark the locations of each CTD cast, which are also shown in Figure 3.1. Note the differing color-scales between surveys. The view is glacierward.

2016, but it is unclear if this is an accurate portrayal of winter circulation, or an artifact of neglecting subglacial discharge and iceberg meltwater.

In our summer scenarios, gravity currents entered LeConte Bay from Frederick Sound at velocities of $\sim$ 1m s^{-1} (Figure 3.8d), consistent with shipboard transects across S1 (Figure 3.5f). Instead of sinking to the bottom of B1 and B2, summer gravity currents traveled along the pycnoclines formed oceanward of S2 and S4. These are the same 90 m and 165–185 m pycnoclines observed in summer surveys, below which rested stagnant water in both the model and observations. Above each pycnocline, where gravity currents reached neutral buoyancy, was a band of fast inflowing water (at 120–165 m depth in B2; Figure C.2) with tidally-averaged velocities similar to those estimated from mooring cross-correlations (Figure 3.8d). This depth also contained the highest concentration of Frederick Sound water in our model, and was where the fastest and warmest inflowing water exists in the summer (Figure 3.8b). In our model, the warm, high Frederick Sound concentration water over-topped S4, and was drawn down to the glacier grounding line. It was then entrained into the subglacial discharge plume and exported from the glacier terminus in a 40 m deep surface layer (Movie S1).

3.3.3 Plume Reflux Calculations.

3.3.3.1 Observed Inflow Composition. On average, 66 $\pm$ 18% of the inflow observed at S3 in August 2016 was composed of refluxed plume water (Figure 3.9d). As expected, the greatest percent (50–80%) of refluxed plume water resided in the slow inflow at 50 – 125 m depth, while the enhanced inflow at 125–165 m depth still consisted of 30–50 % plume water (Figure 3.9a). Below 165 m depth, θ/S properties drift from the Frederick Sound-plume mixing line, indicating the water within and below the 165–185 m pycnocline is mixed with an

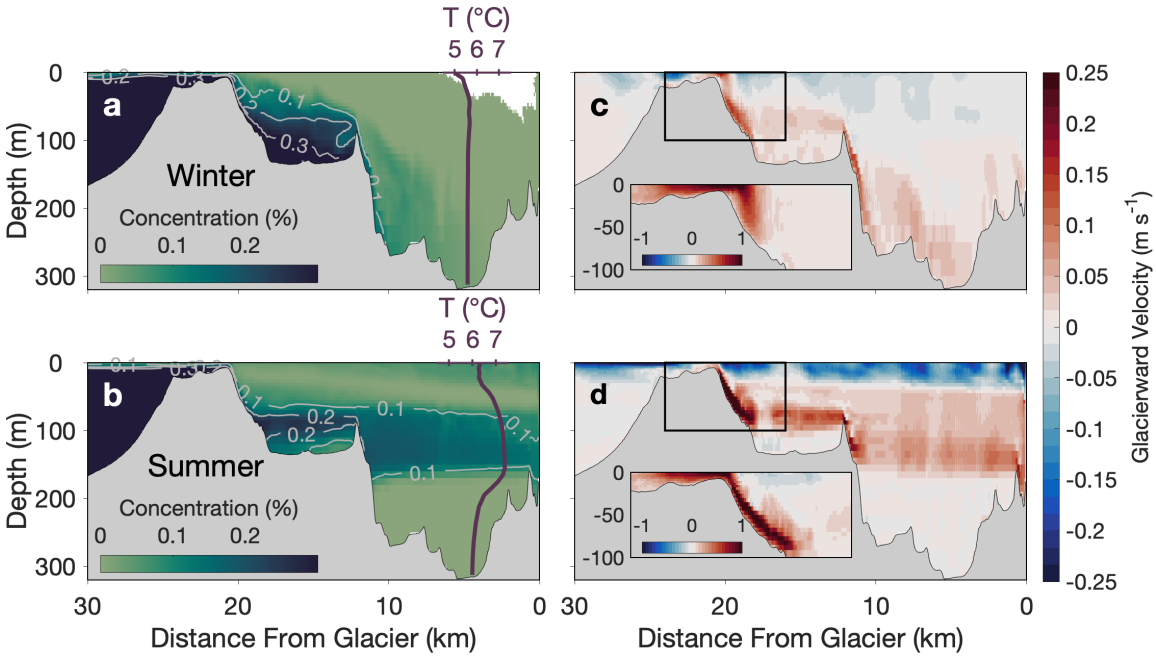

Figure 3.8. MITgcm tidally-averaged, thalweg Frederick Sound passive tracer concentrations and glacierward velocities for **(a, c)** winter and **(b, d)** summer experiments. Tracer concentrations are plotted 7 days after tracer initialization. Purple lines in **a**–**b** are temperature profiles extracted from B2. Insets in **c**–**d** depict instantaneous velocities across S1 (black box) during maximum flood tide. Note the different color-scale used in the insets. The summer run used in **a** and **c** was forced with neap tides and subglacial discharge of 250 m^3 s^{-1}.

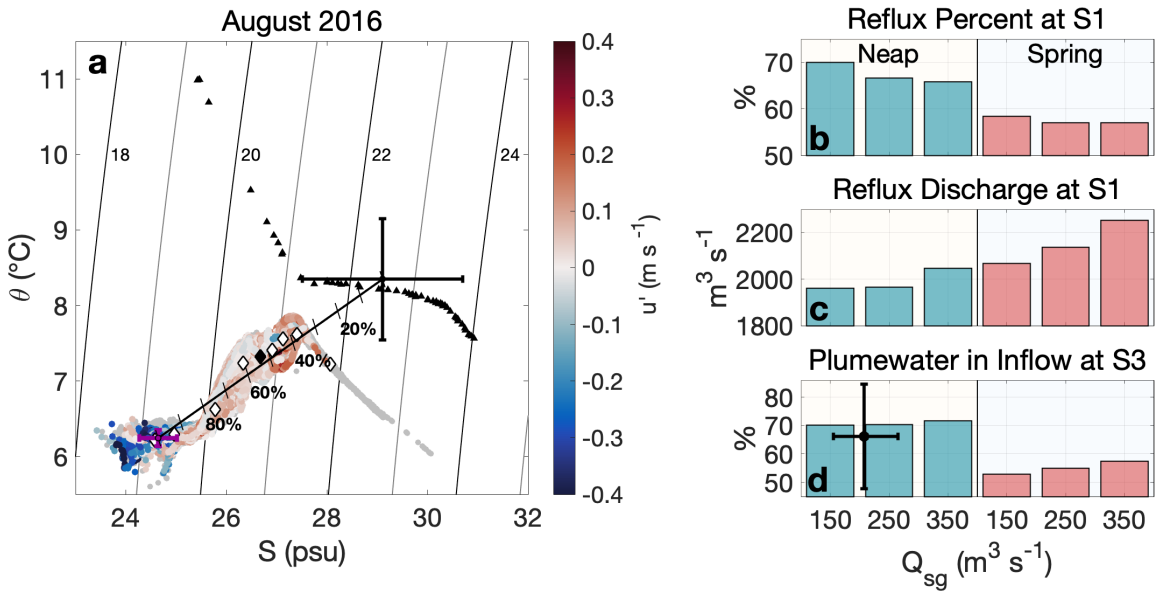

Figure 3.9. **(a)** θ/S data from CTD casts along S3 (circles) and upper Frederick Sound water (black triangles) used to calculate χ_{plm} and X_{plm}. S3 CTD casts are color-coded by glacierward baroclinic velocity, as measured from the 150 kHz ADCP. Gray circles indicate data points without corresponding velocities. Standard deviations of Frederick Sound and plume water properties, used to calculate uncertainty in χ_{plm}, are given as the black and purple error bars, respectively. The mixing line connecting the two end-member means illustrates the percentage of plume water throughout the inflow (χ_{plm}). Diamonds indicate depth intervals of 20 m; the black diamond is at 100 m. Contours denote density anomaly. **(b)** The reflux percent (α_{34}) and **(c)** reflux discharge (Q_R) at S1 for all summer MITgcm runs, plotted by forcing magnitude. **(d)** The fraction of plume water in the inflow at S3 in all summer MITgcm runs, plotted with the average X_{plm} (black error bars) for all transects in **a**. Note the average X_{plm} is plotted with the neap tide model scenarios to represent the tidal phase during the field survey.

additional water body, and contains very little recirculated plume water. This third θ/S signature is consistent with winter deep water.

3.3.3.2 TEF Reflux in MITgcm Experiments. Across all summer runs, 57 – 70% of the outflowing plume was refluxed at the S1 (Figure 3.9b), and plume reflux at all other sills was negligible ($<$ 3% and often $<$ 1%). The addition of subglacial discharge decreased the fraction of the plume that was refluxed at S1 (α_{34}); however, because the plume was larger in higher subglacial

discharge scenarios, this still corresponded to an overall increase in the volume flux of recirculated plume water (Q_R) at S1 (Figure 3.9b–c). Conversely, stronger tidal forcing decreased α_{34}, yet still led to a higher Q_R than neap tide runs. In all summer runs, a greater reflux volume at S1 led to decreased inflowing salinity and near-glacier temperatures for a given tidal forcing (Table C.1). In total, refluxed plume water accounted for 53 – 72% of inflowing water by the time it reached S3 (Figure 3.9b). This was determined by treating the section of the fjord between S3 and Frederick Sound as one mixing zone (Cokelet and Stewart, 1985), and calculating the reflux budget using the oceanward S1 transect and the glacierward S3 transect (Figure 3.1d). α_{34} was higher in our winter experiment than any summer run, reaching 74% at S1 and 8.5% at S2 (Table C.1). Still, due to the weaker water velocities and lack of subglacial discharge, Q_R was on average only 34% of summer runs at S1.

As a point of comparison, we also quantified the impact of shear-driven mixing independent of sills, which we calculated by treating B2 as its own mixing zone. 3% or less of the surface plume was refluxed across B2, comparable to reflux at the three deepest sills. However, up to 10% of the inflow was entrained into the surface plume, indicating the plume continues to grow even after reaching neutral buoyancy.

3.4 Discussion

Our results demonstrate the importance of coupled sill-generated mixing and subglacial plume-driven bouyancy forcing in promoting substantial seasonal differences in fjord circulation. Such seasonal circulation regimes are important drivers of heat advection at LeConte Bay and likely other glacial fjords.

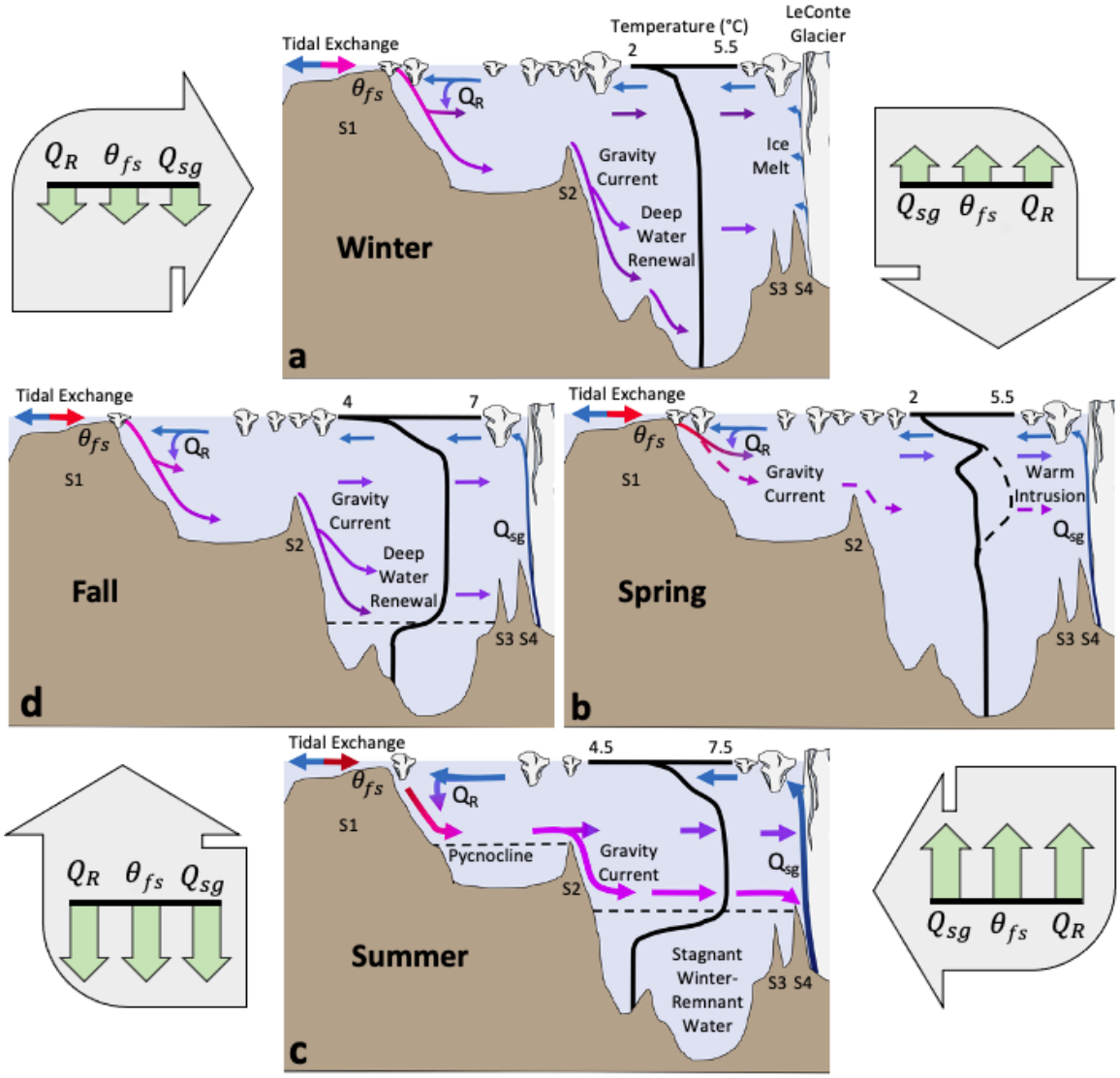

Figure 3.10. Schematics of characteristic along-fjord circulation patterns for each season, along with approximate temperature profiles in B2 (note the differing temperature ranges). Colors of arrows in **a**–**d** represent relative water temperatures. Dashed lines in **b** indicate the progressive deepening of inflowing water throughout the spring transition, as inferred from the Inner Mooring record. Large gray arrows in corners qualitatively depict the trends in subglacial discharge (Q_{sg}), Frederick Sound temperature (θ_{fs}), and reflux discharge (Q_R) between seasons.

3.4.1 Seasonal Circulation and Stratification Regimes. *Winter Regime (November – March)*

In the winter, when subglacial discharge is negligible, fjord renewal and circulation in LeConte Bay is analogous to a non-glacial silled fjord. Large tidal velocities of ~ 1 m s^{-1} across S1 overwhelm any baroclinic transport across the sill, and thus the timing and volume of renewal events is largely dependent on the tidal prism (e.g., Gade and Edwards, 1980; Geyer and Cannon, 1982; Stigebrandt, 1977). Due to the reflux of glacial and iceberg meltwater at S1, LeConte Bay remains fresher than Frederick Sound throughout the winter, which allows renewing water to sink to depth.

Once over S1, renewing water flows glacierward down S1 and S2 as a gravity current until reaching the bottom of the fjord (Figure 3.10a), as evident in our winter MITgcm experiments (Figure 3.8) and mooring time-lagged cross-correlations. Winter transit times from S1 to the glacier terminus may be upwards of 10 days (Figure 3.6), although the water with the highest Frederick Sound concentration is routed to depth in B2 (Figure 3.8a). B2 deep water may eventually be replaced by denser renewing water, reaching the glacier terminus only after some amount of uplift, mixing, and dilution.

In the absence of an appreciable freshwater source in the winter, renewing water properties appear to be determined by two main processes: 1) the volume of Frederick Sound water forced over S1 each flood tide, and 2) the θ/S of Frederick Sound water. Frederick Sound is warmer than LeConte Bay throughout the year (Figure 3.4), and thus differences between spring and neap tidal volume fluxes create fortnightly fluctuations in LeConte Bay, with warming occurring during spring tides (Figure 3.3). The relatively minor difference in salinity between these

two water bodies in the winter ($\sim$ 1 psu) explains why only minimal fortnightly fluctuations in salinity are observed.

Spring Transitional Period (April – mid-June)

The spring transition began when subglacial discharge accelerated at the beginning of the melt season, causing additional mixing and reflux of freshwater at S1. At LeConte Bay, this happened in early April during both years of our study. Almost immediately, renewal of deep water ceased (Figure 3.3), and the fjord entered a temporary transitional period in which a large along-fjord temperature gradient developed across B2 in May 2017 (Figure 3.4). We posit that a similar process to what has been observed at Loch Sunart, Scotland (Gillibrand et al., 1995), occurred at this time. Initially, the additional freshwater reflux freshened inflowing water so that it was less dense than ambient fjord water, thus creating a stratified surface layer that prevented deep water renewal, despite the presence of subglacial discharge. Inflowing water instead flowed glacierward near the surface, creating the warm intrusion at 25 – 50 m depth observed in May 2017 (Figure C.5). Below this depth, advection was weak and a strong along-fjord temperature gradient developed (Figure 3.4). However, as subglacial discharge increased throughout the spring, so did the reflux of freshwater at S1. As with Loch Sunart, freshwater reflux eventually freshened fjord conditions enough to allow renewing water to again sink gradually deeper in the water column (Gillibrand et al., 1995). At LeConte Bay, the Inner Mooring time series depicts the top-down freshening and cooling of the fjord in April, followed by warm intrusions in May that progressively occur deeper in the water column (Figure 3.10b).

Entrainment of ambient fjord water into the subglacial plume expedites this fjord renewal process (Carroll et al., 2017; Gladish et al., 2015), and allows for

dense winter water to be readily replaced by progressively fresher water throughout the melt season. However, water below the glacier's grounding line depth, or oceanward of any obstructing secondary sills, cannot be entrained and renewed, leading to its isolation and stagnation in the spring and summer. Eventually, all water above grounding line depth that can be renewed is replaced by fresher water, creating pycnoclines at grounding line depth or at the depth of obstructing sills. It is above these pycnoclines where summer gravity currents will reach their terminal depth and flow glacierward. In LeConte Bay, this occurs at 90 m depth in B1 and 165–185 m depth in B2, as determined by the depths of S2 and S3/S4, respectively.

Summer Regime (mid-June – mid-September)

We define the beginning of the summer regime as the time when freshwater reflux and plume entrainment have permitted renewing gravity currents to reach their terminal depth above S3 and S4, and establish the 165 – 185 m pycnocline (Figure 3.10c). This occurred in mid-June of both years (Figure 3.3). In B2, gravity currents reached neutral buoyancy at 120 – 165 m, where the fastest glacierward velocities, warmest water, and highest concentrations of Frederick Sound water occurs in the summer (Figures 3.9a and 3.8). MITgcm experiments indicate that the draw down of water from S4 to the grounding line via plume-driven entrainment creates a subcritical flow over S4 that augments velocities on its oceanward side (Figure 3.8d). It seems likely that this process, together with the momentum carried by gravity currents reaching neutral buoyancy at the same depth, are responsible for the enhanced velocities observed at 120 – 165 m. An estuarine exchange flow in the upper 50 m was also prevalent throughout the summer (Figure 3.7).

At S1, the $\sim$ 40 m deep outflowing plume was largely blocked by the shallow sill, creating conditions that could lead to overmixing (Stigebrandt, 1981; Stommel and Farmer, 1953), if not for the strong barotropic tides forcing semi-diurnal exchange with Frederick Sound. The intersection of the plume with S1, paired with fast tidal currents (0.5 – 1 m s^{-1}; Figures 3.5 and 3.8), readily mixed outflowing plume water with inflowing Frederick Sound water. Both MITgcm TEF experiments and August 2016 θ/S observations indicate enough mixing occurs at S1 to cause a majority of the outflowing plume to be recirculated, and subsequently make up the bulk of the inflow. TEF budgets indicate salinities decrease and reflux volumes increase with additional subglacial discharge. Therefore, as subglacial discharge increases throughout July and August, the larger volume of ambient water entrained into the subglacial discharge plume will be replaced by a reciprocal supply of continually fresher renewing water. This creates a cycle of continuous freshening of fjord water and strengthening of pycnoclines (Figure 3.4) until a steady-state is reached, or until subglacial discharge subsides in the fall.

Approximately 10% more of the outflowing plume was expelled from the fjord during spring tide model scenarios. However, by volume, more plume water was refluxed during spring tide, which was on average 1 psu saltier than neap tide plume water. This is the result of larger barotropic volume fluxes over S1, as well as throughout the fjord. Such tidal dependence of reflux volume and salinity explains the fortnightly salinity cycles observed in the mooring record.

Summertime stratification prevents deep water ($>$ 185 m) renewal by gravity currents in B2, and deep water properties in B2 largely maintained their winter signatures throughout both summers (Figures 3.4 and 3.3). However, the gradual freshening and warming of the deepest Inner Mooring sensors indicates the upper

deep water may undergo some renewal through mixing generated by internal tides, although the persistence of water properties below 200 m indicates wave-generated renewal is limited.

We can attribute the variations in summertime water properties in LeConte Bay to three primary forcing mechanisms: 1) θ/S properties of Frederick Sound, 2) strength of tidal forcing, and 3) subglacial discharge. During both summer and winter, tidal forcing regulates the volume of external water entering the fjord; however, when paired with summer subglacial discharge, tidal magnitude is the dominant control on the recirculation of large volumes of freshwater back into the fjord. Buoyancy forcing related to subglacial discharge drives an along-fjord circulation at depth (Motyka et al., 2003), and helps draw Frederick Sound water down each sill toward the grounding line (Carroll et al., 2017). However, our results indicate that in fjords where heavy mixing between layers promotes large reflux volumes, subglacial discharge will also have a substantial impact on the composition of the inflow. Variations in subglacial discharge will therefore affect both the magnitude of the buoyancy-driven flow toward the glacier, as well as the water properties of the inflow.

Fall Transitional Period (mid-September – October)

The fall transition begins with the attenuation of subglacial discharge, which started in mid-September of both years. By the end of October, the water column is almost entirely homogenized (Figure 3.3), except for a remnant of the 165 m – 185 m pycnocline now below the Inner Mooring at 200 m (Figure 3.4). The rapid destruction of stratification illustrates the precarious balance between freshwater reflux and tidal renewal of external water. Without the reflux of substantial volumes of subglacial discharge and associated meltwater, summertime stratification

quickly collapses, and circulation reverts to its winter regime. As inflowing water increases in density, gravity currents propagate deeper into B2, gradually weakening the remnant summer pycnocline and sinking it deeper into the water column (Figure 3.10d).

3.4.2 Implications for Heat Transport to LeConte Glacier.

Multiple lines of evidence indicate heat transport to LeConte Glacier is enhanced during the summer circulation regime, and may become more pronounced with future changes in local climate. First, summertime circulation creates a direct pathway for the warmest water of Frederick Sound, found at its surface, to reach the LeConte Glacier grounding line at 200 m depth, 25 km away. Throughout the summer, heightened along-fjord water velocities rapidly transport Frederick Sound surface water to the glacier terminus within 4 – 5 days, where only the warmest water ($> 7°$C) reaches the grounding line. Summer submarine melt rates of 8 m d^{-1}, the highest observed at LeConte Glacier, coincide with the depth of this intrusion (Sutherland et al., 2019). Upon reaching the terminus, this warm water is entrained into the subglacial discharge (Motyka et al., 2013, 2003) and meltwater plumes (Jackson et al., 2020), and vertically displaced along the glacier terminus. Conversely, in the winter, the highest concentration of Frederick Sound water flows to the bottom of B2, and may only reach the glacier through further mixing and dilution with overlying water.

Second, the majority of the outflowing plume is refluxed at the fjord mouth, which significantly increases the flushing time of LeConte Bay. This is supported through a simple flushing time calculation developed for tidally flushed estuaries (Sanford et al., 1992), which we use for each of our MITgcm scenarios:

$$t_f = \frac{V\ T_{tide}}{(1-b)\ V_{fl} + V_{fw}} \tag{3.8}$$

where V is the fjord volume, T_{tide} is the tidal period, V_{fl} is the flood tidal prism, V_{fw} is the freshwater volume flux (equivalent to subglacial discharge), and b is a return flow factor analogous to α_{34} at S1. Applying this model to LeConte Bay, we consider the entire fjord volume for our winter run, while for summer runs, we only consider the volume of water above 185 m that undergoes renewal. Summer flushing times more than double from 5–11 days if neglecting reflux ($b = 0$) to 11–32 days when reflux is accounting for ($b = \alpha_{34}$; Table C.1). In winter, accounting for reflux increases the fjord flushing time from 22 to 77 days. This indicates reflux may extend the duration of synoptic temperature anomalies within LeConte Bay and delay the export of glacial freshwater to the coastal ocean.

Third, the internal tides observed in both summers suggests such waves may be important to the heat balance of the glacier terminus. Internal tides commonly form near sills, and become particularly pronounced when pycnoclines coincide with sill depth (Gade and Edwards, 1980), as is the case for summer pycnoclines in LeConte Bay. Internal waves may influence the composition of near-glacier water through vertical mixing, or by regulating which water masses flow into B4 (deep water or overlying renewing water). Furthermore, internal waves may introduce additional velocity variance to the near-glacier region, which should increase submarine melt rates.

Finally, the continual replacement of ambient fjord water with fresher recirculated plume water throughout the summer leads to a feedback cycle where LeConte Bay progressively freshens throughout the summer, while pycnoclines strengthen (Figures 3.3 and 3.4). As a result, gravity currents and along-fjord water velocities may also accelerate until subglacial discharge diminishes in the fall, or until a steady-state is reached. If 21^{st} century projections of extreme warming in

Alaska and western North America are realized (Christensen et al., 2013), then we anticipate the initiation of this feedback cycle will occur sooner in the spring and its cessation later in the fall. This transformation will expedite heat transport to LeConte Glacier for a greater portion of the year, which may independently become exaggerated due to warmer ocean temperatures and higher subaerial melt rates. Even in the absence of climate change, such a feedback cycle may also result from ice dynamics processes, such as a retreat along a retrograde slope, which would enhance subglacial discharge (Amundson and Carroll, 2018) and thus reflux.

Although heat advection is at a maximum in the summer, current ocean forcing parameterizations in ice sheet models would still likely overestimate heat advection to LeConte Glacier, due to the neglect of sill-driven mixing. In LeConte Bay, external shelf water accounts for less than half of the inflowing volume transport, and water temperatures near the glacier terminus are at least 3 – 4 °C cooler than Frederick Sound surface water in the summer (Figure 3.4). This leads to the conflicting outcome that sill-driven mixing creates a circulatory cell that amplifies heat advection to the grounding line, yet the reflux of cold plume water simultaneously cools external water as it enters the fjord. Thus, the extrapolation of external water properties from sill depth to the grounding line, as done in the Ice Sheet Model Intercomparison Project for CMIP6 (Slater et al., 2020) and elsewhere (e.g., Khazendar et al., 2019), would greatly exaggerate near-glacier temperatures in LeConte Bay. Sill-driven mixing is, therefore, an under-appreciated component of fjord parameterizations, and its neglect may produce unreliable results in fjords with significant mixing.

3.4.3 Application to Other Glacial Fjords. Variability in subglacial discharge (Jackson and Straneo, 2016; Straneo et al., 2011), wind forcing

(Jackson and Straneo, 2016; Jackson et al., 2014; Moffat, 2014; Moffat et al., 2018), and baroclinic exchange with the shelf (Carroll et al., 2018; Mortensen et al., 2011) have previously been observed as drivers of seasonal modes in glacial fjords. Our results indicate sill-driven mixing of glacial freshwater can also cause pronounced seasonal differences in stratification and circulation, particularly when coupled with subglacial discharge. When ambient fjord water is entrained and displaced by the subglacial discharge plume, mixing and reflux of freshwater at sills ensures it is replaced by fresher water. If this process continues for long enough, the entire water column above the grounding line, or above any obstructing secondary sills, will freshen adequately so that external water is quickly drawn from sill depth along pycnoclines directly to the glacier grounding line, provided it is located deeper than the sill (Carroll et al., 2017).

Despite the strong tidal forcing and shallow-silled geometry of LeConte Bay, the coupling of sill-generated mixing and plume-driven buoyancy forcing is not unique, and has been observed at other glacial fjords. Analogous seasonal behavior to LeConte Bay has been documented at Glacier Bay, Alaska (Matthews, 1981), Jorge Montt Fjord, Patagonia (Moffat et al., 2018), and Godthåbsfjord, Greenland (Mortensen et al., 2014, 2011). At these fjords, summer stratification routes warm surface water along a series of sills and pycnoclines to reach glacier termini at depth. In all cases, the summer regime was associated with the downward mixing of freshwater at entrance sills, leading to a $\lesssim 10\%$ increase in subsurface freshwater fractions at Godthåbsfjord and Jorge Montt Fjords between winter and summer (Matthews, 1981; Moffat et al., 2018; Mortensen et al., 2013). Similar seasonality and associated freshwater mixing has also been observed at other shallow-silled fjords throughout Southeast Alaska (Muench and Heggie, 1978; Walters et al.,

1988), and may be an important control on heat transport to tidewater glaciers throughout that region.

MITgcm modeling of Ilulissat Icefjord, Greenland, suggests the reflux of glacial freshwater can occur even in instances where a subsurface outflowing plume intersects a sill at depth (Gladish et al., 2015). In their experiment, Gladish et al. (2015) showed that the subglacial discharge plume from Jakobshavn Glacier may reach neutral buoyancy at a similar depth to the 245 m entrance sill. The resultant subsurface outflowing plume mixed with inflowing external water at the entrance sill, resulting in cooler fjord water than other scenarios without subglacial discharge. Consistent with our flushing time estimates, fjord residence time increased in their model with additional subglacial discharge, and thus, presumably, the reflux of outflowing water at the sill. Residence time halved with the artificial deepening of the entrance sill by 450 m and the subsequent removal of the mixing zone. A similar process could also occur at Rink Isbrae, where the subsurface plume may intersect a 410 m deep sill at low subglacial discharge (Bartholomaus et al., 2016; Carroll et al., 2016).

Finally, the annual flux of iceberg meltwater often exceeds glacier-derived freshwater sources in glacial fjords, particularly when subglacial discharge is no longer at its maximum (Enderlin et al., 2016; Moon et al., 2018). As most of this meltwater remains at depth (Moon et al., 2018), it seems probable that iceberg meltwater will affect reflux in many silled fjords, particularly in locations where sills ground large icebergs at mixing zones (e.g., Sulak et al., 2017).

3.5 Conclusions

Through pairing extensive observations with three-dimensional numerical modeling, we demonstrated that the reflux of glacial freshwater at fjord sills can

lead to distinct seasonal circulation regimes, particularly when paired with plume-driven buoyancy forcing. At LeConte Bay, the majority of glacial freshwater is refluxed at the shallow entrance sill during the summer, which together with subglacial plume entrainment, readily freshens all fjord water above the grounding line or secondary sills. The resultant stratification enables warm water to flow from the surface of Frederick Sound directly to the LeConte Glacier grounding line at 200 m depth, 25 km from the entrance sill. We expect this summertime circulation to enhance frontal ablation through increasing heat advection to the glacier terminus and forming internal tides; however, further work is needed to quantify the relationship between reflux and near-glacier water properties, and whether this has a significant affect on glacier dynamics.

Similar seasonal circulation regimes to LeConte Bay have been observed at glacial fjords in Patagonia, Greenland, and Alaska, and thus we anticipate our findings to be applicable across many settings. Although LeConte Bay behaves as a relatively simple fjord where shelf exchange only occurs through tidal forcing, similar seasonal patterns have been observed in other fjords of varying geometries. This suggests that freshwater reflux is an important control on circulation and heat advection in many glacial fjords, and is likely to be a critical component to any box-model fjord parameterization.

3.6 Bridge

In Chapter III, I paired MITgcm simulations of LeConte Bay with mooring and shipboard observations to determine how the subsurface release and sill-driven mixing of glacial freshwater drives seasonal circulation in LeConte Bay, Alaska. In Chapter IV, I expand on this study by creating a suite of idealized MITgcm Greenland fjords to determine how sill-driven reflux, subglacial discharge, glacier

submarine melting, iceberg submarine melting, and the bathymetric obstruction of offshore water transform water properties between the continental shelf and tidewater glacier termini. I then quantify the uncertainty these local forcing mechanisms contribute to ocean thermal forcing parameterizations in Greenland ice sheet models. Chapter IV utilizes the novel MITgcm IceBerg package to simulate iceberg melting, which had not been released at the time of Chapter III model experiments.

CHAPTER IV

LOCAL FORCING MECHANISMS CHALLENGE PARAMETERIZATIONS OF OCEAN THERMAL FORCING FOR GREENLAND TIDEWATER GLACIERS

This chapter is formatted for submission to *Geophysical Research Letters*, where it will be co-authored with my advisor, David Sutherland.

Author Contributions:

Alexander Hager conceived of and designed the study, performed the modeling and analysis, wrote the paper, and created the figures. David Sutherland secured the funding, reviewed and edited the manuscript, and contributed guidance and expertise in glacial fjord dynamics.

4.1 Introduction

Mass loss from the Greenland Ice Sheet (GrIS) has contributed 10.8 ± 0.9 mm to mean sea level rise in the last three decades (The IMBIE Team, 2019) and is projected to raise sea level by up to 90 ± 50 mm by 2100 (Goelzer et al., 2020). This mass loss has, in part, been triggered by the tidewater glacier response to warming ocean temperatures (e.g., Holland et al., 2008; Motyka et al., 2011; Murray et al., 2010; Nick et al., 2009; Straneo and Heimbach, 2013; Wood et al., 2018), with frontal ablation accounting for 32–66% of GrIS mass loss since 1972 (Enderlin et al., 2014; Mouginot et al., 2019; Van den Broeke et al., 2016). In Greenland, fjords are the principal pathways connecting tidewater glacier termini to the coastal ocean, where local processes relating to sill-driven mixing and silled obstruction of external water (Hager et al., 2022; Jakobsson et al., 2020; Moffat et al., 2018; Mortensen et al., 2014, 2011, 2013), submarine melting of icebergs and glacier termini (Davison et al., 2020; Jackson et al., 2020; Magorrian and Wells, 2016;

Moon et al., 2018), and subglacial discharge (Carroll et al., 2015; Jenkins, 2011) modulate the magnitude of ocean forcing at the ice-ocean boundary on a seasonal basis (e.g., Hager et al., 2022; Moffat et al., 2018; Mortensen et al., 2013). However, such processes are too small scale to be resolved in global climate models (e.g., Golaz et al., 2019; Watanabe et al., 2010), and instead, sea level rise projections have relied on poorly-validated simplifying parameterizations of oceanic boundary conditions in ice sheet models (e.g., Jourdain et al., 2020; Slater et al., 2020) that create large sources of uncertainty when predicting future mean sea levels (Goelzer et al., 2020; Seroussi et al., 2020). This paper focuses on the ocean thermal forcing of GrIS outlet glaciers, yet Antarctic ice sheet models use similar simplifications to prescribe ocean boundary conditions beneath ice shelves (e.g., Jourdain et al., 2020; Seroussi et al., 2020).

Recent studies have shown that retreat across a population of tidewater glaciers can be reasonably approximated as a linear function of the climate forcing they experience (Black and Joughin, 2022; Cowton et al., 2018; Fahrner et al., 2021; Slater et al., 2019). For many Greenland tidewater glaciers, change in terminus position is specifically the result of enhanced submarine melting of the terminus and subsequent changes to ice dynamics (e.g., Holland et al., 2008; Luckman et al., 2015; Murray et al., 2010; Smith et al., 2020; Straneo and Heimbach, 2013). Taken together, these findings have prompted the development of parameterizations that use submarine melting to drive frontal ablation in ice sheet models. In particular, the Ice Sheet Intercomparison Project for CMIP6 (ISMIP6) (Nowicki et al., 2016), which produced sea level contribution predictions for Greenland in the 6$^{\text{th}}$ Assessment Report of the Intergovernmental Panel on Climate Change (Masson-Delmotte et al., 2021), relies on two such parameterizations. The first

parameterization is the simplest – being designed to be implementable in all participating ISMIP6 models – and is used to determine changes in glacier terminus position over a given time (Slater et al., 2020,1):

$$\Delta L = \kappa \left(Q^{0.4} \, \Theta_{t_2} - Q^{0.4} \, \Theta_{t_1} \right) \tag{4.1}$$

where ΔL is the retreat/advance distance (km) between times t_1 and t_2, Q is the mean summer subglacial discharge, Θ is the ocean thermal forcing (°C above freezing temperature), and κ is a coefficient tuned to fit the observed terminus positions of almost 200 Greenland tidewater glaciers between 1960–2018 (Slater et al., 2019). Here, submarine melting is assumed to scale proportionally to $Q^{0.4}\Theta$.

The second parameterization encompasses only submarine melt, and leaves the subsequent glacier response (as given by the relationship between ice flux, submarine melt, and calving) to be calculated by the ice sheet model (Slater et al., 2020). Here, submarine melt rate ($\dot{m}$) is (Rignot et al., 2016):

$$\dot{m} = (3 \times 10^{-4} \, h \, q^{0.39} + 0.15) \, \Theta^{1.18} \tag{4.2}$$

where h is grounding line depth and q is the annual mean subglacial discharge normalized by calving front area. In both implementations, ice sheet models need a method for prescribing Θ based on offshore ocean conditions. In ISMIP6, this was done by first taking a spatial average of annual mean ocean conditions within seven large regional zones surrounding Greenland (Slater et al., 2020). For the retreat implementation (Eq. 4.1), glaciers are forced with a depth-averaged Θ so that all glaciers within a region experience the same thermal forcing (Slater et al., 2020, 2019). In the submarine melt implementation (Eq. 4.2), an adjustment is made accounting for fjord bathymetry preventing deep currents from reaching the glacier face (Section 4.2.2). However, neither parameterization explicitly

incorporates water transformation between the coast and glacier termini (e.g., Gladish et al., 2015; Straneo et al., 2012), which can vary greatly even between neighboring fjords (Bartholomaus et al., 2016). Furthermore, accelerated mass loss from the Greenland Ice Sheet can be largely attributed to the dynamics of only a small number of individual glaciers (Enderlin et al., 2014; Fahrner et al., 2021), which can dominate the uncertainty in Greenland sea-level contributions (Goelzer et al., 2020). There is thus an "urgent" need for improved parameterizations that incorporate local water transformation and that are validated by high-resolution models or extensive observations (Slater et al., 2020,1).

The large-scale and long-term observations necessary to validate such parameterizations is logistically difficult in Greenland, suggesting a modeling approach is warranted. However, until recently, general circulation models lacked the ability to realistically incorporate iceberg melting, which can be the primary freshwater source in Greenland fjords (Enderlin et al., 2016; Moon et al., 2018). Here, we employ the newly developed IceBerg package (Davison et al., 2020) within the Massachusetts Institute of Technology general circulation model (MITgcm) (Marshall et al., 1997) that enables the inclusion of icebergs to test the accuracy of both ISMIP6 thermal forcing parameterizations across a variety of local forcing conditions. We create a suite of idealized model simulations each forced with different combinations of subglacial discharge, iceberg prevalence, tidal forcing, and sill geometry, but all experiencing the same offshore temperature and salinity conditions at the open boundary. In doing so, our objective is to simulate the diverse array of neighboring fjord conditions that can result from the same regional ocean forcing when local factors are accounted for. We then quantify the error of each ISMIP6 thermal forcing parameterization for all model runs and determine

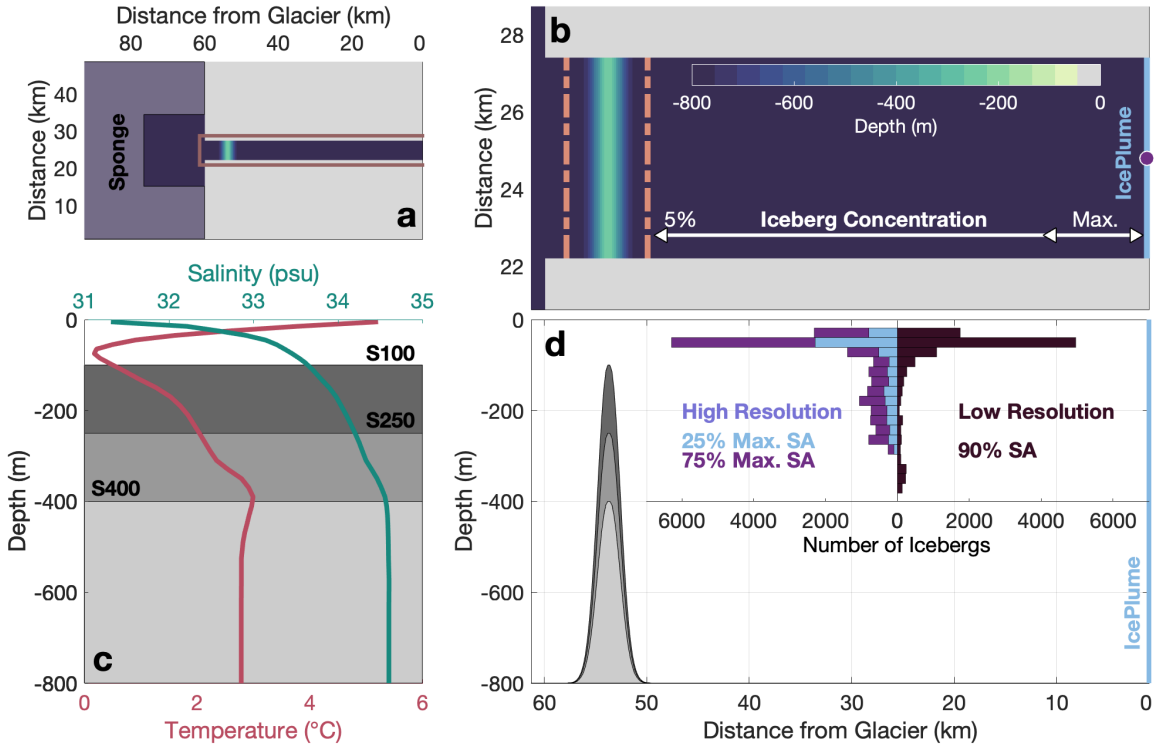

Figure 4.1. **(a)** Model domain with the location of the sponge layer along open boundaries. **(b)** Enlargement of brown box in **a** depicting the locations of the entrance sill, TEF transects (dashed lines), glacier face (blue line), subglacial discharge plume center-point (purple dot), and the distribution of iceberg concentrations. **(c)** Initial and open boundary conditions in relation to the depths of each sill. **(d)** Along-fjord cross-section of **b** depicting the vertical distribution of iceberg keel depths (binned every 25 m) for each iceberg scenario (labeled by the maximum coverage of grid cell surface area, SA), plotted with the depths of each sill.

the primary contributors to local water transformation and uncertainty within each formulation. Based on our results, we recommend simple improvements to current thermal forcing parameterizations that decrease their error by up to 89%.

4.2 Methods

4.2.1 Model Setup. MITgcm fjord geometries were typical of Greenland (e.g., Straneo and Cenedese, 2015) and were 800 m deep, 5 km wide, 60 km long, and had a laterally uniform, Gaussian-shaped sill near the mouth

of the fjord with a minimum depth of either 100 m, 250 m, or 400 m (hereafter distinguished as S100, S250, and S400 runs; Figure 4.1). Vertical resolution was 10 m in the upper 100 m, 20 m between 100 – 500 m depth, and 50 m below 500 m. The majority of runs had horizontal resolutions of 200 m; however, a few high subglacial discharge and iceberg meltwater flux runs were conducted at 500 m resolution (Table D.1). A 800 m deep coastal zone was constructed outside the fjord with an additional 30 cells to the west and 20 cells to the north and south. Horizontal resolution in the coastal zone linearly telescoped to 2 km at the northern, western, and southern open boundaries. A 10 cell sponge layer was imposed at each open boundary to inhibit internal waves from reflecting back into the domain.

All simulations were run in a hydrostatic configuration with a nonlinear free surface and a Coriolis frequency of 1.3752×10^{-4} s^{-1}. High and low resolutions models were run at time steps of 25 – 30 s and 60 s, respectively. Horizontal viscosity was prescribed using a Smagorinsky scheme (Smagorinsky, 1963) and a Smagorinsky constant of 2.2, while horizontal diffusivities were set to zero (some numerical diffusion still exists). We used the KPP parameterization (Large et al., 1994) for vertical mixing, setting the background and maximum viscosity to 5×10^{-4} s^{-1} and 5×10^{-3} s^{-1}, respectively, and background and maximum diffusivities to zero and 5×10^{-5} s^{-1}, respectively. Models were run to steady-state, which occurred after all water below sill depth had been flushed (200-1000 days). Output was averaged over the last 10 days of model time, and all "near-glacier" model output was averaged over the two closest grid cells to the glacier face.

Models were initialized from temperature and salinity profiles observed in 2013–2015 outside the Uummannaq fjord system, West Greenland (Bartholomaus

et al., 2016), which shares a similar vertical structure to coastal properties around Greenland: a warm, fresh summer surface layer underlain by cold Polar Water and warm, salty Atlantic Water at depth (Straneo and Cenedese, 2015; Straneo et al., 2012). The same profiles were used as boundary conditions along the open boundaries (Figure 4.1b). M2 frequency tidal velocities of 5×10^{-3} m s^{-1} were imposed along the western boundary, creating tidal amplitudes of $\sim$ 1.5 m within the fjord, typical of tides throughout East and West Greenland (Howard and Padman, 2021). For fjord geometries where significant tidal mixing was expected (S100 and S250 simulations), we tested additional high and low tidal forcing scenarios with tidal velocities of 7×10^{-3} m s^{-1} and 3×10^{-3} m s^{-1}, creating tides of 2.06 m and 0.88 m, respectively (Table D.1).

Subglacial discharge and glacial submarine melting were parameterized with the IcePlume package (Cowton et al., 2015) using a straight glacier face along the eastern boundary (Figure 4.1c). Summer high resolution runs were forced with subglacial discharge of 300 m^3 s^{-1}, which is typical of summer runoff from Rink Isbræ (Bartholomaus et al., 2016; Carroll et al., 2016). Summer low resolution runs were designed to resemble the largest Greenland glacial fjords and were forced with subglacial discharge of 1000 m^3 s^{-1}, characteristic of glacier runoff entering Sermilik Fjord and Ilulissat Icefjord (Carroll et al., 2016; Echelmeyer and Harrison, 1990; Gladish et al., 2015; Moon et al., 2018). Subglacial discharge plumes are parameterized to have a half-conical geometry in most runs; however, we test the influence of plume geometry (and thus subglacial hydrology) by repeating five runs with subglacial discharge spread out across a 1 km wide line-plume (e.g., Jenkins, 2011), which may be more realistic for some fjord systems (Hager et al., 2022; Jackson et al., 2017; Kajanto et al., 2022). Winter scenarios were

reinitialized from the steady state of summer runs with the same tidal, iceberg, and geometric constraints, but were forced by a 10 m^3 s^{-1} line-plume across the entire glacier width to account for a switch to basal friction-generated, distributed subglacial drainage in the winter (e.g., Cook et al., 2020). To be consistent with ISMIP6 methodology, we do not account for seasonal differences in offshore waters; thus, our seasonal sensitivity runs only test seasonal variation in local forcing mechanisms. In all runs, a background velocity of 0.1 m s^{-1} was implemented to facilitate ambient submarine melting along the glacier face.

Icebergs were parameterized using the IceBerg package (Davison et al., 2020), which treats icebergs as stationary barriers to flow and adjusts surrounding fjord water properties according to calculated meltwater fluxes. Iceberg depths were set using an inverse power law size frequency distribution with an exponent of -1.9, similar to that observed in Rink Isbræ and Sermilik fjords (Sulak et al., 2017). Consistent with observations (e.g., Enderlin et al., 2016; Moon et al., 2018; Schild et al., 2021; Sulak et al., 2017), we prescribed a maximum iceberg depth of 300 m and 400 m in high and low resolution runs, respectively (iceberg size is limited by grid resolution; Figure 4.1d). Icebergs were concentrated at the fjord head, filling either 25% or 75% of the fjord surface area within 10 km of the glacier, which linearly decreased to 5% just inside the entrance sill (Figure 4.1c). These concentrations approximate those observed at Rink Isbræ and Sermilik fjords (Sulak et al., 2017). Additional S250 simulations targeting the ice-choked conditions of Ilulissat Icefjord were conducted at low resolution using an iceberg concentration of 90% throughout the fjord. Submarine meltwater plumes were parameterized by imposing a background velocity of 0.06 m s^{-1} along the iceberg

face. All forcing and geometric conditions were repeated without icebergs. A full list of all 26 model simulations is included in Table D.1.

4.2.2 Testing of ISMIP6 Thermal Forcing Parameterizations.

We follow (Slater et al., 2020) in calculating the equivalents of both ISMIP6 thermal forcing parameterizations, using our open boundary conditions as proxies for regional annual mean water properties. In the first thermal forcing parameterization (ISMIP6retreat) used with Eq. 4.1, thermal forcing is determined by:

$$\Theta(z) = \theta(z) - \theta_f(z) = \theta(z) - [\lambda_1 S(z) + \lambda_2 + \lambda_3 z] \tag{4.3}$$

where θ and S are the prescribed potential temperature and practical salinity profiles at the open boundaries, θ_f is the local freezing temperature at depth z, and $\lambda_1 = -5.73 \times 10^{-2}$°C psu^{-1}, $\lambda_2 = 8.32 \times 10^{-2}$°C, and $\lambda_3 = 7.61 \times 10^{-4}$°C m^{-1} (Jenkins, 2011). Profiles of $\Theta(z)$ are then depth-averaged between 200-500 m depth (Slater et al., 2020) so that Θ is given as a singular value across all model runs for ISMIP6retreat.

In contrast to ISMIP6retreat, the submarine melt thermal forcing parameterization (ISMIP6melt) accounts for bathymetry preventing the flow of external water entering the fjord below sill depth. This is accomplished by first defining an effective depth as the deepest part of the near-glacier water column in direct contact with the open ocean (here equal to the z-coordinate just above sill depth). Water properties above the effective depth are directly extrapolated to the glacier terminus, while water properties below sill depth are made equal to those at the effective depth (Slater et al., 2020). Extrapolated potential temperature and practical salinity are then converted to *in situ* temperature and absolute salinity before calculating thermal forcing across the glacier face: $\Theta(z) = T(z) - T_f(z)$.

Here, T and T_f are the *in situ* temperature and freezing temperature, which together with the absolute salinity are calculated using the non-linear TEOS-10 toolbox (McDougall and Barker, 2011). As in Slater et al. (2020), the final Θ value used in Eq. 4.2 is taken from the grounding line depth. The ISMIP6melt formulation therefore predicts the same thermal forcing for all runs within each of the S100, S250, and S400 groups.

4.2.3 Quantification of Sill-driven Mixing. Following MacCready et al. (2021) and Hager et al. (2022), we quantify the net effect of sill-driven vertical mixing by pairing the estuarine Total Exchange Flow framework (TEF) (MacCready, 2011) with efflux/reflux theory (Cokelet and Stewart, 1985). We use this approach because it provides bulk mixing transports that are easily relatable to other forcing processes. TEF utilizes isohaline coordinates to identify inflowing and outflowing transports that satisfy the Knudsen Relations and account for both tidal and subtidal fluxes (Burchard et al., 2018; Knudsen, 1900; MacCready, 2011). We use 1000 salinity classes to bin salt and volume fluxes across each transect, and employ the dividing salinity method (Lorenz et al., 2019; MacCready et al., 2018) to calculate inward and outward transports, allowing for the potential for multiple layers of each to exist. Inflowing and outflowing transport-weighted salinities are given by $S_{in,out} = F^s_{in,out}/Q_{in,out}$, where $F^s_{in,out}$ and $Q_{in,out}$ are the sums of all inflowing and outflowing salt and volume fluxes, respectively. We treat temperature as a tracer corresponding to each salt class so that the transport-weighted inflowing and outflowing temperatures are calculated as: $T_{in,out} = F^t_{in,out}/Q_{in,out}$ (e.g., Lorenz et al., 2019).

Efflux/reflux theory assumes an estuarine system where mixing is concentrated at constrictions, such as sills, separated by deep basins, or reaches,

where mixing is minimal (Cokelet and Stewart, 1985). At each mixing zone, some portion of inflowing or outflowing water is vertically mixed and recirculated, or refluxed, into the opposing layer and back into its original reach, while the remainder, the efflux, is transported across the mixing zone to the next reach (Figure D.1). Using mass and volume conservation, the percentage of inflowing or outflowing water that is refluxed or effluxed can be written in terms of TEF variables (MacCready et al., 2021), but for the purposes of this paper, we are primarily concerned with α^r_{out}, which represents the percent of the outflowing fjord water that is refluxed at the entrance sill:

$$\alpha^r_{out} = \frac{Q^g_{in}}{Q^g_{out}} \frac{S^o_{in} - S^g_{in}}{S^o_{in} - S^g_{out}} \tag{4.4}$$

where superscripts o and g denote the TEF transports on the oceanward and glacierward sides of the mixing zone, respectively (Figure D.1). We calculated efflux/reflux budgets between two TEF transects on either side of the entrance sill, and avoid prescribing icebergs within the sill region to ensure temperature and salt are conserved across the mixing zone. More information about using TEF with efflux/reflux theory can be found in MacCready et al. (2021), Hager et al. (2022), and in Appendix D.

4.2.4 Calculation of Local Heat Fluxes. Quantifying the heat fluxes associated with each local forcing mechanism is important when determining the primary causes of local water transformation. The heat flux resulting from the submarine melting of ice (H_{melt}) is calculated by:

$$H_{melt} = \rho_{mw}\, Q_{mw}[L + c_i(\theta_f - \theta_i)] \tag{4.5}$$

where ρ_{mw} is the meltwater density (1000 kg m^{-3}), Q_{mw} is the total meltwater flux as determined from IceBerg or IcePlume, L is the latent heat of fusion, c_i is the heat capacity of ice, θ_f is the potential freezing temperature, and θ_i is the potential temperature of ice. In our experiments, ice is set to its melting temperature so that Eq. 4.5 collapses to

$$H_{berg} = \rho_{mw}\, Q_{berg}\, L \tag{4.6}$$

and

$$H_{sm} = \rho_{mw}\, Q_{sm}\, L \tag{4.7}$$

for the iceberg and glacier submarine melt heat fluxes, respectively.

Advective heat fluxes (H_{adv}) arising from sill-driven reflux and subglacial discharge are given by:

$$H_{adv} = \rho\, c_p\, Q\, (\theta_{adv} - \theta_r) \tag{4.8}$$

where ρ is the water density, c_p is the heat capacity of water, Q is the advective volume flux, θ_{adv} is the potential temperature of the advected fluid, and θ_r is a reference temperature. To calculate the sill-driven heat reflux (here called heat reflux), we substitute TEF quantities into Eq. 4.8 so that:

$$H_{reflux} = \rho\, c_p\, \alpha^r_{out} Q^g_{out}\, (T^g_{out} - T^g_{in}) \tag{4.9}$$

where $\alpha^r_{out} Q^g_{out}$ is the reflux volume, $T^g_{out} - T^g_{in}$ is the temperature difference between the outflowing and inflowing layers on the sill's glacierward side, and ρ is the refluxed water density as determined from T^g_{out}, S^g_{out}, and the mid-column water pressure at 400 m depth. For the subglacial discharge heat flux, Eq. 4.8 is a specified as:

$$H_{sg} = \rho_{sg}\, c_p\, Q_{sg}\, (T_{sg} - T^g_{in}) \tag{4.10}$$

where Q_{sg} is the total subglacial discharge, ρ_{sg} is 1000 kg m^{-3}, T_{sg} is 0°C, and the reference temperature, T^g_{in}, is chosen to be consistent with Eq. 4.9. In practice, T^g_{in} works well as a reference temperature in both Eqs. 4.9 and 4.10 as inflowing water properties remain largely unaltered between the sill and glacier face.

4.2.5 Empirical Orthogonal Functions of Near-Glacier Variability.

Empirical Orthogonal Function (EOF) analysis was conducted on near-glacier thermal forcing profiles to determine the dominant modes of variability between runs. Near-glacier $\Theta(z)$ profiles were cross-sectionally averaged before removing the mean Θ within each sill group (Figure D.2a). This second step was necessary to account for the dependence of mean fjord temperatures on sill depth (Figure 4.2). EOFs were then calculated on the resultant profiles (Figure D.2b).

4.3 Results

4.3.1 Near-Glacier Water Properties.

The simulations illustrate how local forcing processes (e.g., bathymetric obstruction of offshore water, sill-driven mixing, subglacial discharge, iceberg and glacier submarine melting) determine near-glacier fjord conditions. Despite identical temperature and salinity forcing at the open boundaries, area-weighted mean thermal forcing ($\Theta_{\bar{A}}$) at the glacier face varied by 2.7°C across all runs, while salinities differed by up to 1.4 psu (Figure 4.2, Table D.1). Grounding line thermal forcing varied by 2.9°C between runs. In the deepest silled model runs (S400), near-glacier water properties largely reflect imposed boundary conditions, particularly below 200 m where influence from subglacial discharge and iceberg melt is negligible. However, deep (below sill depth) water properties progressively freshen and cool as sill depth shoals, allowing for $\Theta_{\bar{A}}$ to be neatly grouped by depth of sill: 4.2–4.7°C for S400 runs, 3.6–4.1°C for S250 runs, and 2.0–2.9°C for S100 runs (Figure 4.2).

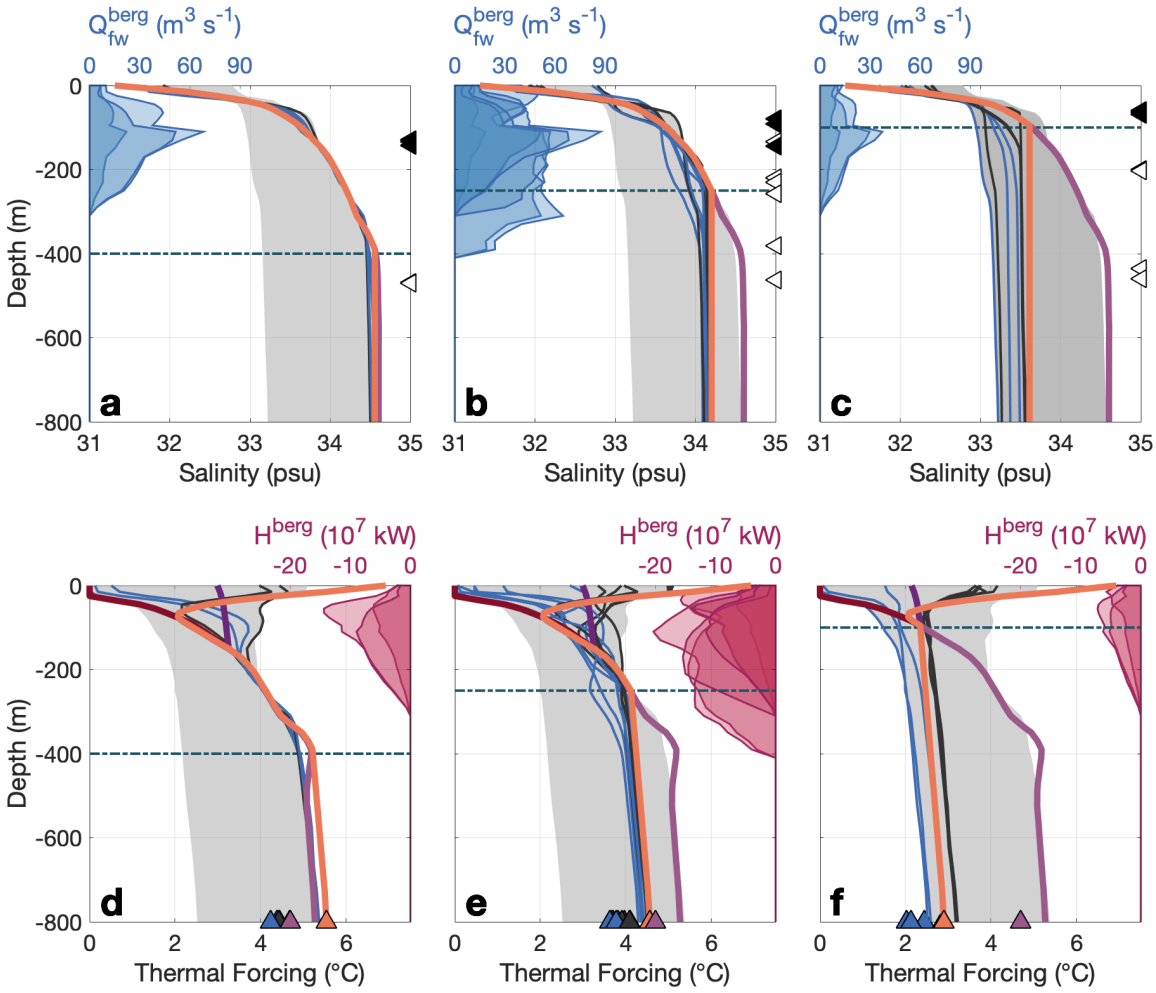

Figure 4.2. Near-glacier **(a-c)** salinity and **(d-f)** thermal forcing profiles for all iceberg (blue) and non-iceberg (gray) runs, plotted with profiles of ISMIP6retreat (violet) and ISMIP6melt/AWmelt (orange). In **d-f**, red and purple profiles depict the AWberg and AWconst parameterizations, respectively. The gray background in all plots illustrates the range across all runs and the horizontal dashed line depicts sill depth (**a,d** are S400 runs; **b,e** are S250 runs; **c,f** are S100 runs). Triangles in **a-c** represent the terminal plume depth for line-plumes (white) and half-conical plumes (black). Violet and orange triangles in **d-f** depict $\Theta(z)$ for ISMIP6retreat and ISMIP6melt, respectively, in relation to $\Theta_{\bar{A}}$ for iceberg (blue triangles) and non-iceberg (gray triangles) runs. The vertical distribution of iceberg freshwater fluxes (Q_{fw}^{berg}) and heat fluxes (H^{berg}) are shown in **a-c** and **d-f**, respectively.

.

Deep water properties are almost entirely homogeneous in all runs, with only minor variability occurring when icebergs keels extend below sill depth or subglacial discharge plumes reach neutral buoyancy below sill depth (this most often occurs with line-plumes). The greatest variability exists above 150 m, where most iceberg melting occurs and where most summer subglacial discharge plumes reach neutral buoyancy (Figure 4.2).

Unsurprisingly, iceberg runs were always cooler than their non-iceberg counterparts; however, the difference between these groups is larger for runs with shallower sills. On average, the difference in $\Theta_{\bar{A}}$ between iceberg and non-iceberg runs diminished from 0.7°C for S100 runs to 0.3°C and 0.2°C for S250 and S400 runs, respectively. Iceberg melt had the greatest impact on water properties in the upper 150 m, contributing to a temperature range of 5.1°C at the surface, independent of sill depth. However, where iceberg keel depth exceeded sill depth, iceberg melting cooled the entire water column to the grounding line, indicating some volume of iceberg meltwater was mixed and refluxed at the silled mixing zone. Such cooling is most pronounced in S100 runs, where the difference in grounding line thermal forcing was on average 0.5°C between iceberg and non-iceberg runs.

$\Theta_{\bar{A}}$ showed no significant difference between tidal sensitivity runs, neither was there an appreciable distinction between runs with sheet and half-conical plumes and otherwise equivalent forcing. Winter runs were generally cooler than their summer counterparts in the upper 150 m, particularly at the depth where summer subglacial discharge plumes warm the water column but are absent in the winter (Figure D.3). However, seasonal variability in the upper 150 m still fell within the limits set by iceberg and non-iceberg runs, and there was no distinction

in deep water properties between seasons. In total, $\Theta_{\bar{A}}$ varied $\leq$ 0.3°C between winter and summer runs with otherwise equivalent forcing (Table D.1).

After removing the dominant influence of sills, EOF analysis indicates the presence or absence of icebergs accounts for 85% of the remaining thermal forcing variability between runs. In general, this first EOF mode reflects the same pattern of cooling in the upper 300 m present in all iceberg runs (Figure D.2b), but its amplitude changes sign for non-iceberg runs, thus imitating the warm surface water that exists when icebergs are absent. The second EOF mode makes up 8% of the variance between runs and has a spatial structure identical to the open boundary temperature conditions. Therefore, the second mode can be interpreted as the influence of regional ocean temperatures on near-glacier thermal forcing. A third EOF mode contributing 5% of the variance depicts temperature variability coincident with the terminal depths of subglacial discharge plumes (Figure D.2b), and is therefore interpreted to represent variable outflowing plume conditions. As reflux affects the entire deep water column evenly, variability resulting from reflux is difficult to discern through EOF analysis. It is therefore possible that reflux variability is incorporated into any of the three dominant modes, part of the remaining 2% of the variance without clear physical corollaries, or was removed with the mean during EOF computation.

4.3.2 Internal Freshwater Sources and Heat Fluxes. In summer iceberg runs, iceberg meltwater made up $32 - 66\%$ of the freshwater budget, while subglacial discharge similarly contributed $31 - 66\%$ of the total freshwater input. Glacier submarine melting only accounted for $1 - 4\%$ of the freshwater budget for summer iceberg runs. Iceberg melting comprised $\sim$ 95% of the freshwater budget in iceberg winter runs, with subglacial discharge and submarine melt making up

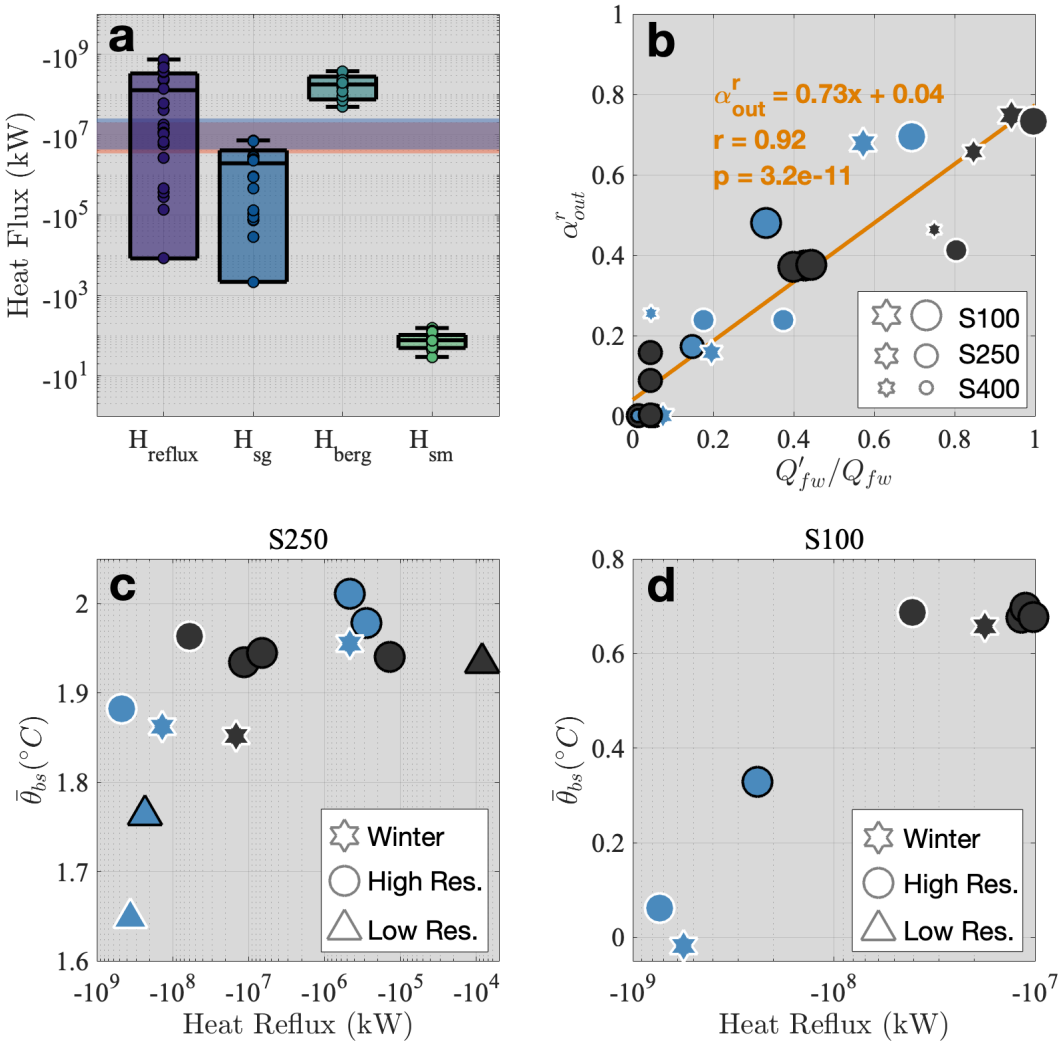

Figure 4.3. **(a)** Box plots of heat fluxes associated with reflux (H_{reflux}), subglacial discharge (H_{sg}), iceberg submarine melting (H_{berg}), and glacier submarine melting (H_{sm}). Box plots depict maximum, minimum, mean, and standard deviations across all runs. Horizontal blue and orange rectangles depicts ranges of estimated surface heat fluxes for winter and summer runs, respectively. Note that summer surface heat fluxes are reflected across the x-axis for illustrative purposes, but are actually positive and represent surface warming. **(b)** Reflux fraction (α^r_{out}) as a function of Q'_{fw}/Q_{fw}, the portion of the total freshwater budget released below sill depth. Stars and circles differentiate between winter and summer runs, respectively. Marker sizes vary by sill depth. Orange line is Eq. 4.11. **(c-d)** Depth-averaged, near-glacier temperatures below sill depth ($\bar{\theta}_{bs}$) as a function of heat reflux for S250 and S100 runs. Marker shape differentiates between winter (stars), summer high resolution (circles), and summer low resolution (triangles) runs. In **b-d**, blue and gray markers represent iceberg and non-iceberg runs, respectively, and white edges depict runs forced with a line-plume.

the remaining 5%. In non-iceberg summer runs, subglacial discharge accounted for $\geq$ 90% of the freshwater budget; however, glacier submarine melting was the primary source of freshwater in winter non-iceberg runs, making up 53–65% of the total freshwater input.

Despite comparable freshwater fluxes, the heat flux from iceberg submarine melting surpassed that from subglacial discharge by multiple orders of magnitude, regardless of iceberg concentration or subglacial discharge (Figure 4.3a). Iceberg melting removed heat from surrounding waters at rates of -4.9×10^7 to -3.8×10^8 kW. In contrast, subglacial discharge heat fluxes were -2.2×10^3 to -7.2×10^6 kW and glacier submarine melt heat fluxes were -29 to -150 kW. The heat flux associated with refluxed outflowing water (here called heat reflux) spanned five orders of magnitude from -8.3×10^3 to -7.4×10^8 kW, at its maximum exceeding the magnitudes of even the largest iceberg heat fluxes, while at its minimum falling near the lower limits of subglacial discharge heat flux.

As opposed to heat fluxes from freshwater sources, which principally cool the upper water column, heat reflux can directly facilitate cooling of deep water. Our experiments show an exponential cooling of deep water temperatures with increasingly negative heat reflux for both S250 and S100 runs, resulting in a decrease of over $\sim$ 0.3°C and $\sim$ 0.6°C, respectively (Figure 4.3a–b). In general, the runs with the highest heat reflux either contained icebergs, line-plumes, or both; however, there is no clear relationship between heat reflux and any specific local forcing processes (Figure 4.3a–b). Nevertheless, there is a highly significant ($r = 0.92$, $p = 3.2 \times 10^{-11}$) linear relationship between the portion of the freshwater budget released below sill depth and the percent of outflowing water refluxed at the

entrance sill, α^r_{out} (Figure 4.3b). In our experiments, α^r_{out} can be estimated by:

$$\alpha^r_{out} = 0.73\frac{Q'_{fw}}{Q_f w} + 0.04 \tag{4.11}$$

where Q_{fw} is the freshwater flux and the prime denotes freshwater entering the domain below sill depth (subglacial discharge is included in Q'_{fw} if the plume reaches neutral buoyancy below sill depth).

All S100 runs had significant sill-driven reflux ($\alpha^r_{out} \geq 37\%$). α^r_{out} in S250 runs ranges from $0 - 66\%$, but is highest in runs with substantial iceberg freshwater flux below sill depth, or in runs with sheet-like plumes (Figure 4.3b). α^r_{out} was negligible in all summer S400 runs, but became significant in winter runs where weak subglacial discharge plumes still intersect the sill at depth (Table D.1). Despite equivalent α^r_{out} between S100 tidal sensitivity runs ($\sim 37\%$), tidal forcing does have a minor effect on S250 runs and is responsible for a range of $0.2 - 16\%$ across S250 tidal scenarios (Table D.1).

4.3.3 Thermal Forcing Parameterizations. Overall, ISMIP6melt predicts $\Theta_{\bar{A}}$ better than ISMIP6retreat, where the root mean square error (RMSE) is 0.74°C for ISMIP6melt and 1.31°C for ISMIP6retreat (Table D.2). However, neither parameterization was satisfactory across all sill depths, and both decreased in accuracy when icebergs were introduced (Figure 4.4, Table D.2). ISMIP6retreat performed best for S400 runs (RMSE = 0.31°C), in which fjord water was of similar composition to shelf water. However, the accuracy of ISMIP6retreat decreased substantially with successively shallower sills (RMSE of 0.83°C for S250 and 2.1°C for S100 runs). Conversely, the ISMIP6melt was best at predicting $\Theta_{\bar{A}}$ for S100 runs (RMSE = 0.44°C), but poorly predicted $\Theta_{\bar{A}}$ in S400 runs (RMSE = 1.12°C). Within the S400, S250, and S100 groups, the RMSE of both parameterizations

was ~ 0.2°C, ~ 0.3°C, and ~ 0.7°C higher in iceberg runs than non-iceberg runs, respectively.

4.4 Discussion

4.4.1 Uncertainty in Thermal Forcing Parameterizations.

Our results demonstrate the wide range of fjord conditions that can result from equivalent regional ocean forcing and emphasize the need for local processes to be incorporated into the coupling of global climate and ice sheet models. In order of importance, we identify these local processes as:

1. *Bathymetric obstruction of external water* – The 2.7°C range in $\Theta_{\bar{A}}$ in our runs is strongly dependent on the depth of the entrance sill, which preferentially blocks warm water from entering the fjord when the sill is shallow. The prominent thermocline between 100 m – 400 m depth in our boundary conditions (Figure 2.1b) has been observed in fjords throughout Greenland, and marks the transition between Polar and Atlantic water (Straneo et al., 2012). In our experiments, external temperatures range from 0.46°C at 100 m to 3°C at 400 m depth (Figure 2.1b), nearly the exact range in $\Theta_{\bar{A}}$ between S100 runs and S400. Furthermore, we see no overlap in $\Theta_{\bar{A}}$ between the three sill depths. Therefore, we conclude that the depth of the entrance sill in relation to the 100 m – 400 m thermocline plays a first-order role in determining internal fjord temperatures, but we do not expect sill depth to be a strong control when sills lie below the Polar–Atlantic water thermocline.

2. *Presence or absence of icebergs* – After adjusting for the silled obstruction of external water, cooling from iceberg meltwater (or lack thereof) is responsible

for 85% of the remaining variability between runs, as well as a temperature difference of 5.1°C at the surface. Similar magnitudes of iceberg-driven cooling were modeled in Davison et al. (2020), Davison et al. (2022), and Kajanto et al. (2022). Iceberg meltwater fluxes are comparable to subglacial discharge in summer runs and dominate the freshwater budget in the winter, which is in agreement with prior estimates of iceberg meltwater fluxes in Greenland fjords (Enderlin et al., 2016; Moon et al., 2018). However, the additional energy required to melt this volume of water enables icebergs to disproportionately cool the surrounding water column when compared to a similar volume flux of subglacial discharge.

3. *Refluxed outflowing water* – Heat reflux can rival the heat flux of iceberg melting, leading to a substantial cooling of deep water temperatures. Where heat reflux is important, the $\lesssim$ 0.6°C cooling occurs throughout the water column from sill depth to the grounding line, often affecting a much larger portion of the water column than the melting of icebergs. While such an effect is hard to identify with EOF analysis, the exponential decrease of deep water temperatures with heat reflux (Figure 4.3) indicates this process has the potential to significantly impact near-glacier thermal forcing in certain fjords.

4. *Subglacial discharge* – While subglacial discharge certainly affects near-glacier thermal forcing, the variability (both inter- and intra-seasonal) this contributes to near-glacier temperature profiles is overshadowed by the influence of icebergs. EOF analysis suggests subglacial discharge is responsible for only 5% of the near-glacier temperature variability. However,

subglacial discharge remains a critical driver of submarine melting through its influence on glacial fjord circulation (Carroll et al., 2015; Sciascia et al., 2013; Straneo et al., 2011; Xu et al., 2012), deep water renewal (Carroll et al., 2017), turbulent upwelling (Slater et al., 2015), near-glacier horizontal circulation (Slater et al., 2018), and enhanced iceberg melt (Kajanto et al., 2022). Our results further indicate the terminal depth of subglacial discharge plumes can directly affect reflux at silled mixing zones, and thus influence deep water temperatures.

5. *Surface heat flux* – Although we neglect surface heat fluxes in our model, we approximate their magnitude based on previous estimates from Sermilik Fjord. Surface heat fluxes in Sermilik Fjord are thought to be ~ 80 W m^{-2} in the summer and ~ -100 W m^{-2} in the winter (Hasholt et al., 2004; Jackson and Straneo, 2016). Applying these values to the exposed surface area (not covered by icebergs) in our simulations, we estimate total surface heat fluxes in our simulations would be 3.4×10^6 to 2.0×10^7 kW in the summer and -4.3×10^6 to -2.5×10^7 kW in the winter (Figure 4.3). Thus, surface heat fluxes could often exceed those from subglacial discharge but are an order of magnitude less than iceberg melt heat fluxes. However, surface heating only affects the uppermost water column, and thus we do not expect it to substantially affect $\theta_{\bar{A}}$ in Greenland fjords. Nevertheless, surface heating may significantly affect heat reflux in Alaska and Patagonia fjords where shallow sills protrude into the surface layer (e.g., Hager et al., 2022).

6. *Glacier submarine melting* – While our modeling suggests glacier submarine melting has a negligible affect on near-glacier thermal forcing, we cannot

discount it as an important variable. Our model resolution is too coarse to resolve the complexities of the ice-ocean boundary, and recent observations indicate the IcePlume package may underestimate ambient melting by a factor of 100 (Jackson et al., 2020).

Observational studies point to similar drivers of contrasting water properties between nearby fjords. In northwest Greenland, slight differences in sill geometry allow warm Atlantic Water to flow unimpeded into Petermann Fjord, while inflow of Atlantic Water into the inner basin of neighboring Sherard Osborn Fjord is restricted to a cross-sectional area $\sim$ 7.5$\times$ smaller (Jakobsson et al., 2020). When paired with enhanced sill-driven reflux of glacially-modified water, this restricted heat inflow is responsible for a 0.2°C difference in near-glacier water between these otherwise similar fjords (Jakobsson et al., 2020). Furthermore, Rink Isbræ, Kangerlussuup Sermia, and Sermeq Kujalleq (Jakobshavn Isbræ) are all located within the same ISMIP6 region, and are thus subject to the equivalent ocean thermal forcing in ISMIP6 projections (except for bathymetric adjustments used for ISMIP6melt) (Slater et al., 2020). Yet, mean fjord temperatures in the upper 100 m differed by up to 2.5°C in summer 2014, seemingly due to the large iceberg meltwater flux into Ilulissat Icefjord, where Sermeq Kujalleq terminates (Bartholomaus et al., 2016; Mojica et al., 2021). These observations align with our model results, and further highlight the importance of sill processes and iceberg melting in determining near-glacier water properties.

In addition to local forcing processes, our results point to a further source of error in the commonly used thermal forcing paramaterizations, namely the dependence on specific depths when calculating thermal forcing. For ISMIP6retreat, a depth-average of regional ocean thermal forcing from 200–500 m

was chosen to encompass most Greenland tidewater glacier grounding lines (Slater et al., 2020), yet this depth range also bounds the largest vertical temperature gradient along the Greenland coast. Thus, any sill that exists within or above this range will greatly affect the ability of ISMIP6retreat to accurately predict near-glacier thermal forcing. Indeed, ISMIP6retreat was fairly accurate for S400 runs, in which the difference in 200–500 m temperatures between external and internal water was minimal, but its accuracy decreased progressively with each shallower sill as the temperature difference between external and internal water increased to $> 1.5°C$.

Although ISMIP6melt accounts for silled obstruction of external water, its accuracy in predicting near-glacier forcing remained dependent on sill depth. We explain this paradox by ISMIP6melt's reliance on the grounding line thermal forcing, which is at a maximum except for the uppermost surface waters because $\Theta(z)$ increases with pressure. However, due to the homogeneity of deep water, grounding line thermal forcing in S100 runs is close to its depth-averaged value and thus $\Theta_{\bar{A}}$, while the difference between grounding line and depth-averaged thermal forcing is still large for S400 runs where homogeneous deep water comprises a smaller portion of the water column (Figure 4.2). Therefore, our results indicate reliance on grounding line temperatures may lead to an overestimation of near-glacier thermal forcing, particularly for fjords with deep or non-existent sills.

4.4.2 Translation of Thermal Forcing Uncertainty to Frontal Ablation Parameterizations.

Together, the sources of uncertainty in ISMIP6retreat and ISMIP6melt translate into large errors in frontal ablation rates provided by Eqs. 4.1 and 4.2 (Figure 4.4). Using the 25^{th} and 75^{th} percentiles of κ (Slater et al., 2019), we find the $\leq 2.6°C$ difference between $\Theta_{\bar{A}}$ and Θ prescribed

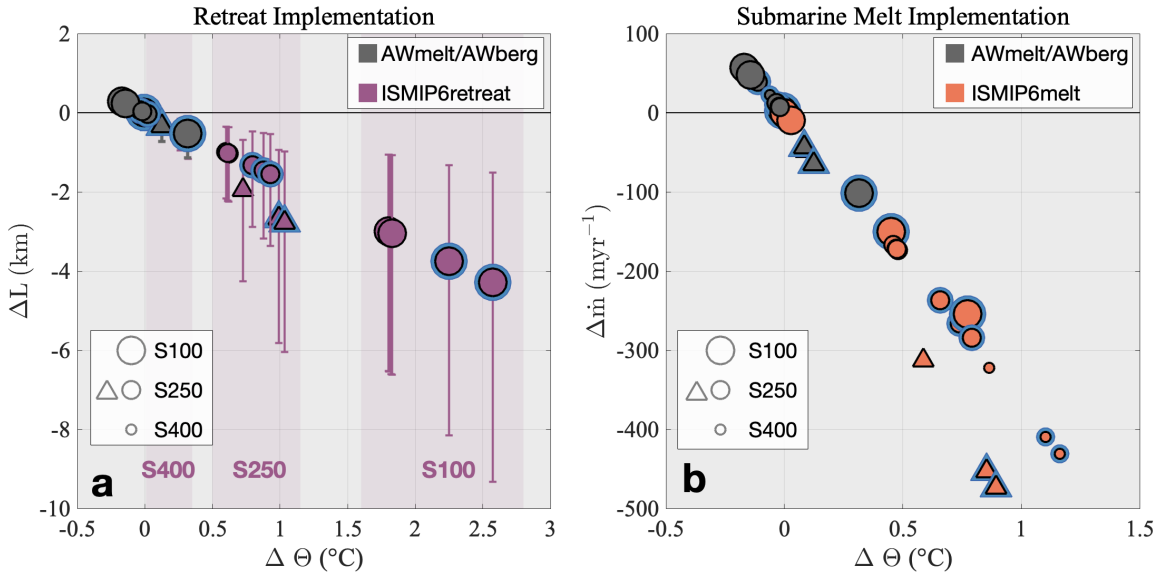

Figure 4.4. Uncertainty in the ISMIP6 **(a)** retreat implementation (Eq. 4.1) and **(b)** submarine melt implementation (Eq.4.2) resulting from the error of thermal forcing parameterizations. In **a**, purple markers denote ΔL uncertainty resulting from ISMIP6retreat, while gray markers denote ΔL uncertainty when employing AWberg for iceberg runs and AWmelt for non-iceberg runs. In **b**, orange markers denote uncertainty in $\dot{m}$ arising from error in ISMIP6melt, and gray indicates uncertainty when using AWberg for iceberg runs and AWmelt for non-iceberg runs. $\Delta\Theta$ is the difference between $\Theta_{\bar{A}}$ and Θ as predicted by either ISMIP6retreat or ISMIP6melt. In both plots, iceberg runs are depicted with blue edges, low resolution S250 runs are represented with triangles, and marker size scales with sill depth. Error bars in **a** denote the range in uncertainty given by the 25^{th} and 75^{th} percentiles of κ, with the marker depicting the 50^{th} percentile. Plots only include summer scenarios to be consistent with the dependence of Eq. 4.1 on summer subglacial discharge.

by ISMIP6retreat translates to an uncertainty in the terminus positions of S100 glaciers of up to 1.5 – 9.3 km (Fig. 4.4). On average, GrIS tidewater glaciers are projected to retreat 10 – 25 km by the end of the 21st Century (Slater et al., 2020), indicating the retreat uncertainty arising from the ISMIP6retreat thermal forcing parameterization is substantial compared to the predicted long-term retreat of GrIS glaciers.

Even for S250 runs the error in prescribed retreat can be significant, particularly for our large-iceberg, high-discharge Ilulissat Icefjord-style simulations (error in ΔL is $\leq$ 6 km). Only in fjords with sills below the offshore 100 – 400 m deep thermocline (Figure 2.1b), such as our S400 runs, do we expect the ISMIP6retreat error to be small enough not to significantly impact ΔL. However, at present, only 10 individual glaciers are responsible for the majority of GrIS mass loss (Fahrner et al., 2021), three of which, Kakiffaat Sermiat, Sverdrup Gletsjer, and Sermeq Kujalleq, terminate in fjords with sills $\lesssim$ 250 m deep (as opposed to grounding line depths of 400 – 800 m) (Morlighem et al., 2017). In particular, Sermeq Kujalleq, which terminates in Ilulissat Icefjord, single-handedly accounts for 10% of GrIS mass loss (Smith et al., 2020) and dominates uncertainty in mass balance projections of central-West Greenland (Goelzer et al., 2020). Therefore, the large ISMIP6retreat error in S250 and S100 runs could signify substantial uncertainty in the terminus positions for some of the GrIS' most important contributors to sea level rise, and thus mass loss for the GrIS as a whole.

Although ISMIP6melt is more accurate than ISMIP6retreat, it still results in over-prescribing submarine melting by up to $\sim$ 500m yr^{-1} (Figure 4.4b). There is no clear dependence of ISMIP6melt uncertainty on any particular local forcing mechanism, but in general, the error tends to be greatest for S400 runs, or S250

runs with icebergs and/or high subglacial discharge. Dependence of ISMIP6melt uncertainty on sill depth highlights the detrimental effect of defining Θ only at the grounding line. This error should be particularly significant for large glaciers terminating in iceberg-packed fjords with deep sills, such as Helheim Gletsjer (Moon et al., 2018; Morlighem et al., 2017), the second largest contributor to GrIS mass loss (Fahrner et al., 2021).

4.4.3 Improved Thermal Forcing Parameterizations. Motivated by the results above, we develop and test four modifications to ISMIP6melt and ISMIP6retreat that account for the largest sources of uncertainty in our experiments. We first test revisions of each ISMIP6melt and ISMIP6retreat that are independent of specific depths, here called AWmelt and AWretreat, respectively. Thermal forcing profiles are calculated as done for ISMIP6melt and ISMIP6retreat, but are extrapolated across the glacier terminus and an area-weighted average thermal forcing is calculated instead of pulling from a set depth (Figure D.4). The third parameterization (AWberg) accounts for bathymetric obstructions in the same way as ISMIP6melt, but the surface 150 m follow the Gade slope submarine melt mixing line (Gade, 1979; Straneo and Cenedese, 2015) to approximate the influence of iceberg submarine melting on the upper water column (Figure 4.2). As surface salinity in the fjord remains relatively similar to external water (Figure 4.2), we leave salinity unchanged from ISMIP6melt, and adjust temperatures accordingly to fit the Gade slope. A final modification is made in which below freezing temperatures are set to the *in situ* freezing point (Figure D.4). In practice, AWberg sets the lower limit of cooling that can occur through submarine melting, while AWmelt sets the upper bound on surface temperatures attainable for non-iceberg runs (Figure 4.2). Therefore, we test a fourth, middle-

ground parameterization (AWconst) in which the ISMIP6melt temperature and salinity at 150 m is extrapolated to the surface before calculating the thermal forcing profile (Figure 4.2). For both AWconst and AWberg, the final thermal forcing value used in Equations 4.1 and 4.2 is again an area-weighted mean across the glacier face.

AWmelt and AWretreat both perform better than their depth-dependent counterparts (overall RMSE of 0.29°C and 1.17°C, respectively), although the accuracy of AWretreat is still heavily dependent on sill depth (Table D.2). AWmelt provides a reliable thermal forcing prediction for all sill depths, but its accuracy wanes for iceberg runs (RMSE = 0.39°C) compared to non-iceberg runs (RMSE = 0.13°C). Conversely, AWberg is quite accurate for iceberg runs (RMSE = 0.17°C) and less so for non-iceberg runs (RMSE = 0.34°C), but remains an accurate predictor of thermal forcing for the entire ensemble (RMSE = 0.26°C). AWconst performed similarly to AWmelt (Table D.2), and thus we focus our discussion on AWmelt and AWberg, the two physically-based updated parameterizations.

Across all runs, AWmelt and AWberg each decreased uncertainty by $61 - 80\%$ when compared to the pre-existing ISMIP6 parameterizations. However, their true merit would come through some *a priori* knowledge or likelihood estimate of iceberg presence, whereby AWmelt could be used in fjords with few icebergs and AWberg used where icebergs are prevalent. Such a tactic would result in a $75 - 89\%$ error reduction from ISMIP6melt and ISMIP6retreat in our experiments. This translates to a mean error of 0.18 km for ΔL and 31 m yr^{-1} for $\dot{m}$ (Figure 4.4), only 8% and 14% of the errors when using ISMIP6retreat and ISMIP6melt, respectively. Furthermore, the relatively small error in frontal ablation is dispersed between over-predicting and under-predicting ablation for different

runs, resulting in a mean error near zero for both ΔL and $\dot{m}$ (Figure 4.4). We suggest such a prediction of iceberg presence could rely on the terminus ice flux or a calving law, which when paired with grounding line depth (to derive maximum iceberg keel depth) and fjord geometry (to identify iceberg pinning points) may estimate an iceberg concentration for each fjord. If no such predictor is feasible, then a universal implementation of either AWmelt or AWberg would still greatly improve parameterizations of near-glacier thermal forcing, although we expect AWberg to be more applicable to majority of Greenland glaciers, particularly as ice mass loss accelerates (e.g., Goelzer et al., 2020).

Implementation of AWberg and AWmelt in ice sheet models would first require re-tuning κ in Eq. 4.1 to fit retreat observations, akin to Slater et al. (2019). As the range of κ values is meant to encompass uncertainties stemming in part from error in ISMIP6retreat, we expect the considerable reduction in thermal forcing parameterization error to narrow the range of κ values and thus possible retreat scenarios for GrIS glaciers. Retreat uncertainty reduction will be most significant for glaciers terminating in iceberg-laden, shallow-silled fjords, where near-glacier thermal forcing differs greatly from the far-field ocean.

Finally, the success of AWberg in capturing the effects of iceberg melting suggests a similar approach could be implemented in Antarctic ice sheet models to account for the basal melting of ice shelves. Currently, ice shelf basal melting is not parameterized in the extrapolation of far-field ocean properties beneath ice shelves, so that modeled sub-shelf temperatures are warmer than observed (Jourdain et al., 2020; Seroussi et al., 2020). This suggests sub-ice-shelf thermal forcing parameterizations could be improved using a similar approach to AWberg.

4.4.4 Remaining Uncertainty Associated with Sill-Driven Mixing.

While AWberg effectively parameterizes the two largest sources of uncertainty in predicting near-glacier thermal forcing – bathymetric obstruction and iceberg meltwater – it does not account for the modification of deep water though sill-driven reflux, which was found to be significant in this study and in previous work (Davison et al., 2022; Hager et al., 2022; Kajanto et al., 2022). The influence of reflux is difficult to discern through EOF analysis, although multiple lines of evidence highlight its importance in shallow silled fjords. First, heat reflux has the potential to exceed even the greatest iceberg heat fluxes, and is responsible for the cooling of deep water (88% of the water column in S100 runs) by up to $\sim$ 0.6°C (Figure 4.3). Second, the difference in uncertainty between iceberg and non-iceberg runs increases with each shallower sill depth, regardless of parameterization. This is even true for AWberg, which effectively accounts for iceberg melting near the surface. Thus, there must be an additional source of error associated with icebergs that is also dependent on sill depth, which can only be explained through the cooling of deep water through the reflux of iceberg meltwater and subglacial discharge.

Deep water cooling from sill-driven mixing is not expected to be important in fjords with sills deeper than iceberg keels or the summer terminal plume depth; however, reflux is likely influential in a number of critical glacial fjord systems. As discussed above, some of the largest contributors to GrIS mass loss empty into fjords with sills $\lesssim$ 250 m deep, where we expect heat reflux to significantly influence near-glacier temperatures. Indeed, recent modeling of Ilulissat Icefjord indicates the sill-driven reflux of iceberg meltwater cools near-glacier water by 0.2°C (Kajanto et al., 2022), a result shared by our Ilulissat Icefjord-style low resolution runs.

Although the updated parameterizations presented in this paper greatly decrease error compared to existing ISMIP6 methods, incorporation of sill-driven mixing could further reduce error in shallow silled fjords, such as the Ilulissat Icefjord-Sermeq Kujalleq system. We anticipate such improvements would require the use of box-models that contain representations of iceberg melting, subglacial discharge, and reflux. The strong linear dependence of α^r_{out} on Q'_{fw}/Q_{fw} (Figure 4.3b) indicates reflux fractions can be accurately estimated from the vertical distribution of freshwater fluxes in the water column, without any knowledge of tidal forcing. Thus, Eq. 4.11 could be used within a box-model to predict reflux, assuming the model can approximate freshwater fluxes throughout the water column.

4.5 Conclusions

In summary, we have tested the accuracy of common ocean thermal forcing parameterizations across a wide range of local forcing scenarios and fjord geometries, and identified fjord bathymetry and iceberg melt-driven cooling as the two greatest sources of error when translating regional water properties to tidewater glacier termini. Accordingly, we made simple corrections to existing ISMIP6 parameterizations that appropriately account for each of these local factors and significantly decreased parameterization error. The AWberg and AWmelt parameterizations presented here each reduced uncertainty in Θ predictions by 61–80% when compared to current ISMIP6 methods. However, when paired together so that AWmelt is used in fjords with few icebergs and AWberg is used where icebergs are pervasive, then regional ocean water properties can be used to predict near-glacier thermal forcing within an error margin of 0.13–0.17°C (eliminating 75–89% of the error for ISMIP6 parameterizations). This decreased

error in predicting Θ would vastly reduce uncertainty in projections of frontal ablation for individual glaciers. Prediction of iceberg prevalence in Greenland fjords is an topic of ongoing research (e.g., Shankar et al., 2021), but until such work is implementable in ice sheet models, we suggest AWberg could serve as a suitable universal thermal forcing parameterization for Greenland fjords. We note that such a change would require recalibration of κ in the ISMIP6 retreat implementation (Eq. 4.1), but that this would result in a substantial decrease in the range of retreat scenarios for individual glaciers.

Our experiments did not explore the influence of offshore intra-annual variability on internal fjord temperatures (e.g., Davison et al., 2022; Kajanto et al., 2022), and required fjords to be at steady-state, which is likely unattainable in Greenland. Therefore, further work is needed to test the accuracy of AWberg and AWmelt in temporally varying conditions. Additional improvements to the parameterizations presented here could take the form of a box-model that can effectively represent sill-driven reflux. We emphasize that such a model would need to accurately parameterize iceberg melting and subglacial discharge plumes, as well as incorporate local fjord bathymetry. Still, the revised thermal forcing parameterizations are an encouraging improvement to existing methods, and their simplicity makes them relatively straightforward to implement in the next generation of ice sheet models.

CHAPTER V

CONCLUSIONS

5.1 Summary

Mass loss from the Antarctic and Greenland ice sheets is accelerating and will substantially raise global sea level by the end of the 21st Century. Yet, there is still considerable uncertainty in sea level rise projections arising in part from unknown physics at the ice-ocean and ice-bed boundaries, as well as untested simplifying parameterizations of these critical systems. In this dissertation, I have investigated how glacially sourced meltwater impacts ice dynamics through its influence on basal sliding, frontal ablation, glacial fjord circulation, and ocean thermal forcing. I then explored how these processes are parameterized in ice sheet models, and what impact more realistic representation could have on ice sheet projections.

In Chapter II, I developed a novel approach for subglacial hydrology modeling in which I ran a parameter sweep of over 130 MALI simulations that were compared with radar specularity content to select for possible realistic drainage networks beneath Thwaites Glacier. This work demonstrated that enough basal friction-generated meltwater exists at the bed of Thwaites Glacier, and possibly other large Antarctic glaciers, to form stable subglacial channels with grounding line fluxes of 80 $\pm$ 24 m^3 s^{-1}. In all data-compatible runs, modeled subglacial channels intersected the grounding line directly at the the location of highest observed sub-ice-shelf melt rates, suggesting they are an important driver of frontal ablation and thus Thwaites Glacier retreat. Nevertheless, upstream of the grounding line, subglacial channels may help buttress against retreat by lowering effective pressures across the glacier width. Finally, modeled effective pressures

in data-compatible runs were considerably smaller than what current ice sheet model parameterizations would predict, highlighting the need for process-based parameterizations of effective pressure that encompass the effects of channelized subglacial drainage.

In Chapter III, I transitioned from the subglacial environment to investigate the influence of glacial meltwater in driving fjord dynamics. This chapter leveraged a suite of mooring and shipboard observations with three-dimensional numerical modeling to demonstrate that the subglacial release and sill-driven mixing of glacial freshwater can cause distinct seasonal circulation regimes that directly affect heat transport to the LeConte Glacier terminus. In the summer, subglacial discharge reflux and buoyancy forcing create a circulatory cell that draws warm external surface water directly to the glacier grounding line at 200 m depth, likely enhancing frontal ablation and increasing susceptibility to climate change. It is expected similar behavior occurs throughout Alaska, Patagonia, and in some Greenland fjords, where such local water transformation could lead to unrealistic parameterizations of ocean thermal forcing of the GrIS.

In Chapter IV, I investigated this claim further by quantifying the effect of sill-driven mixing, as well as other local forcing mechanisms, in determining near-glacier thermal forcing in Greenland. I found that the bathymetric obstruction of offshore water and the submarine melting of icebergs are the two dominant local controls on near-glacier water properties. Based on this result, I developed an updated method for prescribing ocean thermal forcing of the GrIS that greatly decreases error in both thermal forcing and frontal ablation projections when compared to the current ISMIP6 framework. While sill-driven meltwater reflux is not incorporated into the new methodology, my results suggest its

inclusion in a fjord-scale box model could further improve ocean thermal forcing parameterizations.

5.2 Future Work

The results presented in this dissertation provide myriad avenues for further research. Possible future work in Antarctic could include:

1. Chapter II results suggest subglacial channels could affect the stability of Thwaites Glacier by enhancing submarine melting while potentially increasing basal friction. However, it remains unclear which is the more important process. Thus, employing a fully coupled ice dynamics-subglacial hydrology model to quantify the effect of channelized subglacial drainage on the ice dynamics of Thwaites Glacier is imperative to accurately predicting the retreat of Thwaites Glacier and similar Antarctic glaciers. Such work could use the fully coupled MALI model to run projections of Thwaites Glacier retreat with varying levels of channelization, as based on my Chapter II results.

2. The inability of the hydrostatic ocean connection assumption to accurately portray modeled effective pressures beneath Thwaites Glacier demonstrates an updated parameterization is needed for Antarctic ice sheet models. Such a parameterization would need to be computationally efficient while accounting for the effects of channelized subglacial drainage, and may rely on hydropotential mapping and basal meltwater input to estimate the locations and discharges of subglacial channels, as well as their effect on nearby effective pressures. Development and validation of this parameterization could be part of the ice dynamics-subglacial hydrology modeling described above.

3. The release of subglacial discharge from Antarctic tidewaters has the potential to significantly influence ice shelf melting, ocean circulation, and nutrient transport in the iron-depleted Southern Ocean. Currently, the model framework exists to couple the Regional Ocean Modeling System (ROMS) to the Elmer/Ice ice-dynamics model, while allowing for modeled subglacial discharge from the Glacier Drainage System (GlaDS) to be passed into the ROMS domain as a freshwater input. Coupling of these three models would enable a detailed exploration of where channelized subglacial discharge may be entering the Southern Ocean, and investigate its impact on ice shelf stability, ocean circulation, and nutrient transport. Ideally, such a project would employ GlaDS to map the locations and discharges of subglacial channels at glacier grounding lines, preferably validated by radar specularity content where feasible. The grounding line transports would then be fed into ROMS, which will be coupled with the ice shelf portion of Elmer/Ice, to determine their impact on ice shelf melt rates and ocean dynamics. This study could either look at a particular region of Antarctica, such as the Amundson Sea, or Antarctica as a whole.

Motivated by Chapters III and IV, possible future research on Greenland glacial fjords could include:

1. Implement updated ocean thermal forcing parameterizations for use in ISMIP7. Assuming ISMIP7 uses a similar approach to ISMIP6 to prescribe tidewater glacier retreat, this would first require re-tuning κ in Eq. 4.1, akin to Slater et al. (2019), but using AWberg and/or AWmelt to parameterize near-glacier thermal forcing. A proper test to check that the updated

parameterizations will indeed improve GrIS ice loss projections will be to determine that the range of κ values decreased from the original ISMIP6 implementation, thus signifying reduced uncertainty in retreat projections. If this is true, then we will have confidence that the updated ocean thermal forcing parameterizations will indeed improve GrIS mass loss projections.

2. Develop a fjord-scale box-model that realistically accounts for bathymetric obstruction, iceberg melting, sill-driven reflux, subglacial discharge, and surface heat flux that can be used to couple global climate models to ice sheet models. Box models have already been developed for non-glacial fjords (e.g., Gillibrand et al., 2013) and are under development in glacial settings (e.g., Sanchez et al., 2022). Once designed, box-models will first need to be validated with observations under a variety of local forcing conditions, or compared to a 3-D circulation model in a similar fashion to my Chapter IV research, before being implemented in ice sheet models.

3. Deploy a vast observational network to track the evolution of offshore and inner fjord water properties to validate the parameterizations put forth in Chapter IV, and test their applicability in temporally variable systems. Ideally, such a study would employ mooring arrays to compare far-field ocean properties with those near glacier termini in neighboring fjords subject to differing bathymetry and iceberg forcing. Central West Greenland is likely the best location for this study due to the number of differing fjord systems in close proximity to each other. One significant challenge will be avoiding iceberg collisions with the mooring array; however, a possible solution may be to only deploy moorings at depth within fjords and supplement observations of the upper water column with repeat shipboard and/or helicopter-based

CTD surveys. As the resources required for such a study would be extensive, a pilot program in Godthåbsfjord could test its efficacy in a shallow-silled fjord, while remaining easily accessible from nearby Nuuk.

APPENDIX A

CHAPTER II: PARAMETER SWEEP, SENSITIVITY ANALYSIS, AND STEADY-STATE CRITERIA

A full sweep of realistic conductivity parameter space was conducted for each set of bed roughness parameters; however, our method for determining bed roughness parameters was closer to that of a sensitivity analysis (varying one parameter at a time). This choice was made because real physical constraints exist for conductivity parameters, while bed roughness parameters are theoretical quantities approximating general bed characteristics that only have indirect physical corollaries. A sensitivity analysis is thus more suitable for bed roughness parameters and allowed us to ease the complexity of sampling a four-dimensional parameter space. Results for each conductivity parameter sweep (in addition to Figure 2.4) are depicted in Figures A.1 – A.5.

Establishing steady-state criteria inherently involves defining a cutoff threshold for acceptable noise remaining in the model. For our pressure steady-state runs, effective pressure at each cell is allowed to fluctuate 0.5% of its value on average. This equates to an allowable fluctuation of roughly 1 kPa where effective pressure is lowest ($\sim$ 200 kPa) and 10 kPa where effective pressure is highest ($\sim$ 2000 kPa). For flux steady-state runs, meltwater production above each transect must equal the total discharge across the transect within 0.5%. Total melt production above the grounding line is roughly 155 m^{-1} s^{-1}, so our flux steady-state criteria require that we know the total grounding line discharge within 0.8 m^{-1} s^{-1}, which is orders of magnitude less than the uncertainty between data-compatible FSS runs.

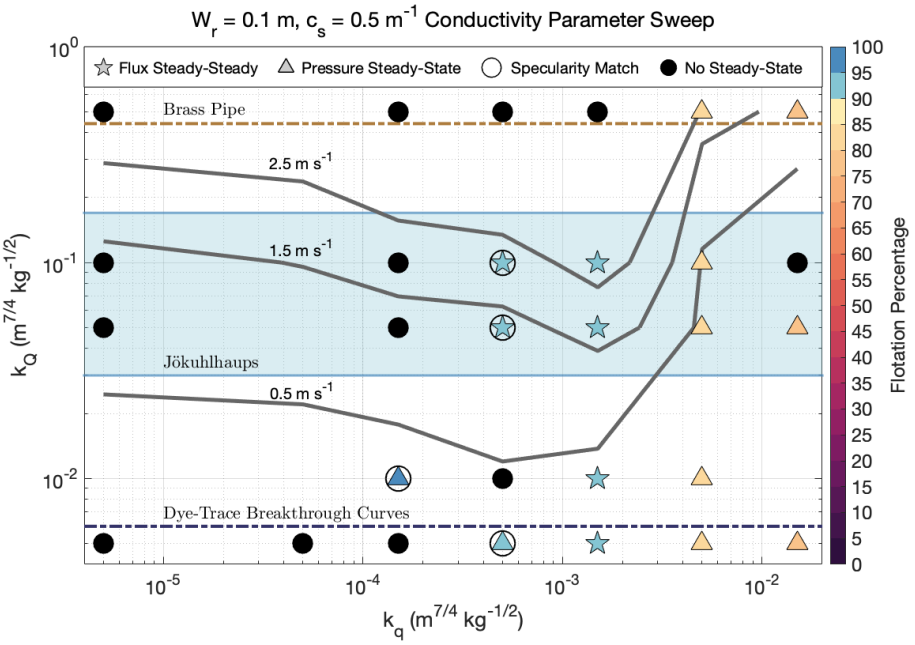

Figure A.1. Same as Figure 2.4, but for bed roughness parameters $W_r = 0.1$ m and $c_s = 0.5$ m^{-1}. Stars represent runs that reached flux (and pressure) steady-state, triangles symbolize pressure steady-state simulations, and filled black circles depict runs that did not reach either steady-state criterion. Symbols for steady-state runs are color-coded by the average flotation percentage of grounded ice. Circles around stars or triangles indicate runs that matched observed specularity content, and are considered data-compatible. Gray lines are 95^{th} percentile channel velocity contours for channels with $\vec{Q} > 5$ m^3 s^{-1}. k_Q limits determined from a brass pipe and dye-trace breakthrough curves are plotted as brown and dark-blue dashed lines, respectively, and the blue shaded area represents the typical observed Jökulhlaup k_Q range.

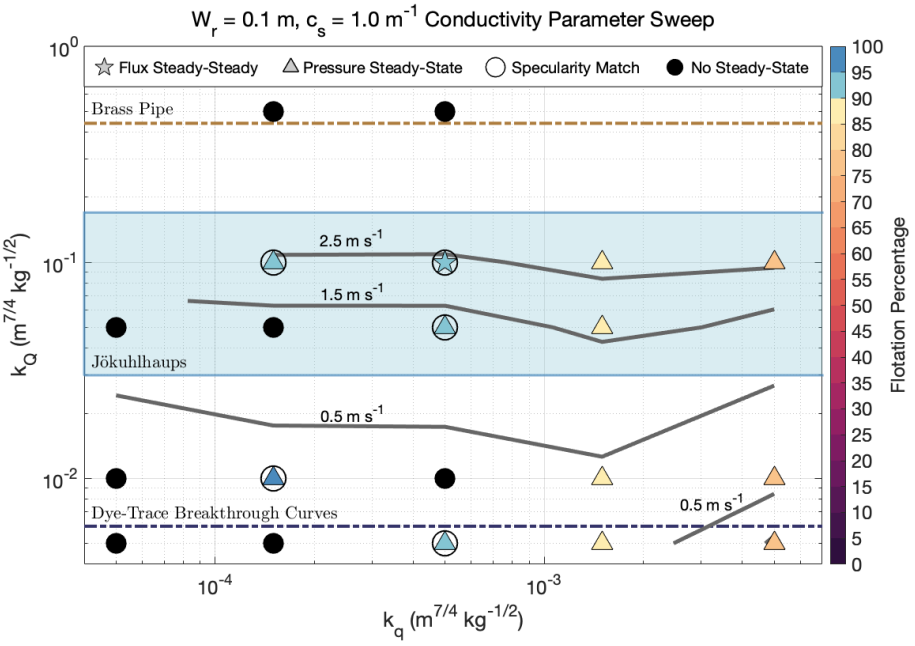

Figure A.2. Same as Figure 2.4, but for bed roughness parameters $W_r = 0.1$ m and $c_s = 1.0$ m^{-1}.

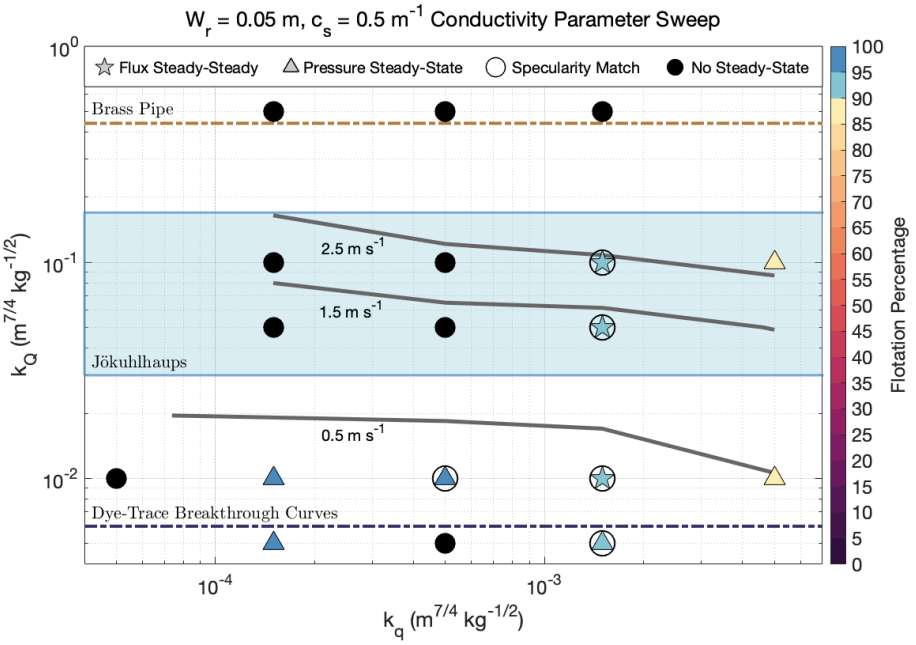

Figure A.3. Same as Figure 2.4, but for bed roughness parameters $W_r = 0.05$ m and $c_s = 0.5$ m^{-1}.

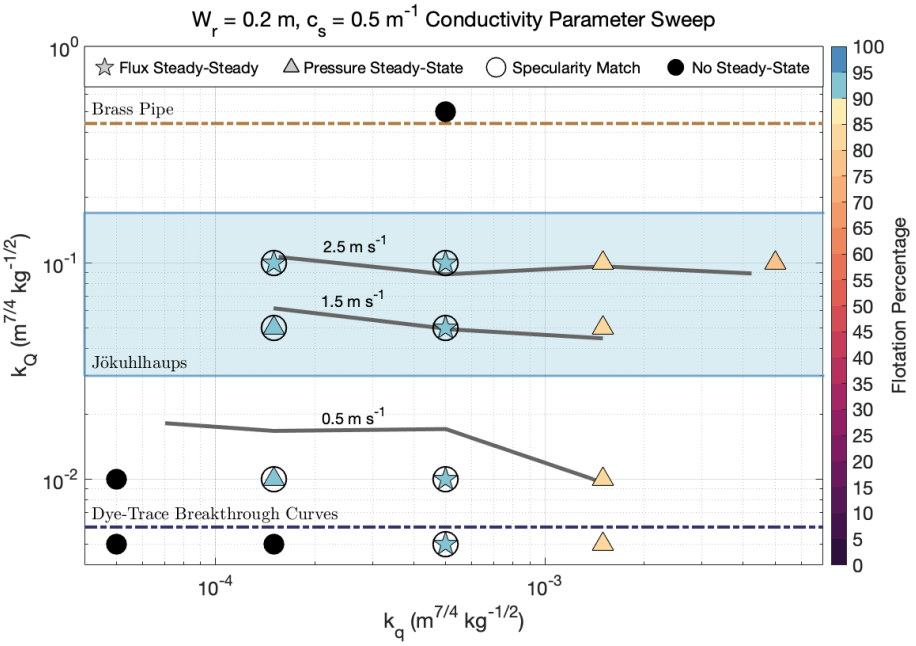

Figure A.4. Same as Figure 2.4, but for bed roughness parameters $W_r = 0.2$ m and $c_s = 0.5$ m^{-1}.

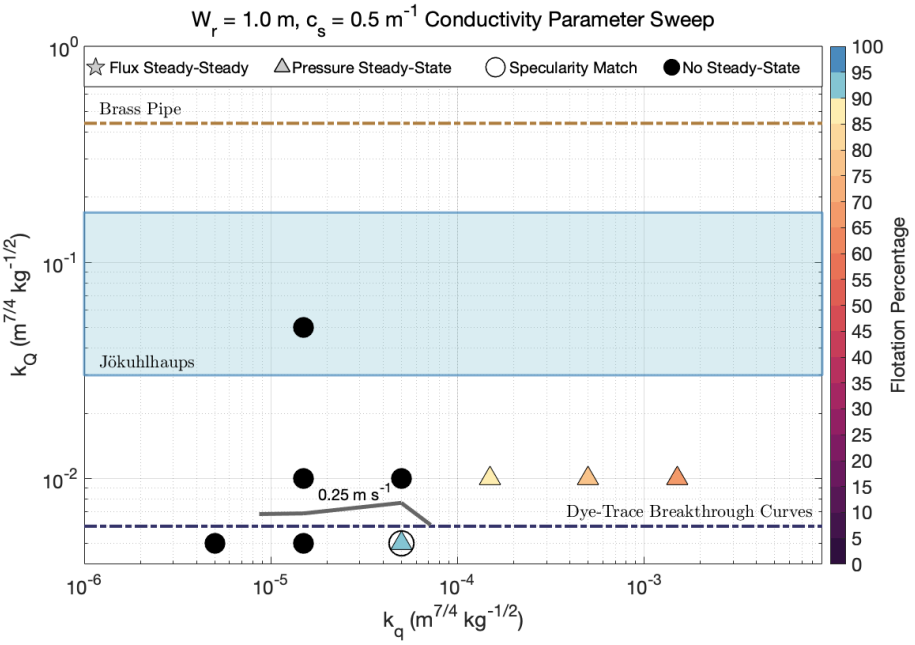

Figure A.5. Same as Figure 2.4, but for bed roughness parameters $W_r = 1.0$ m and $c_s = 0.5$ m^{-1}.

APPENDIX B

CHAPTER II: COMPARISON CRITERIA BETWEEN MODELED AND OBSERVED SPECULARITY CONTENT

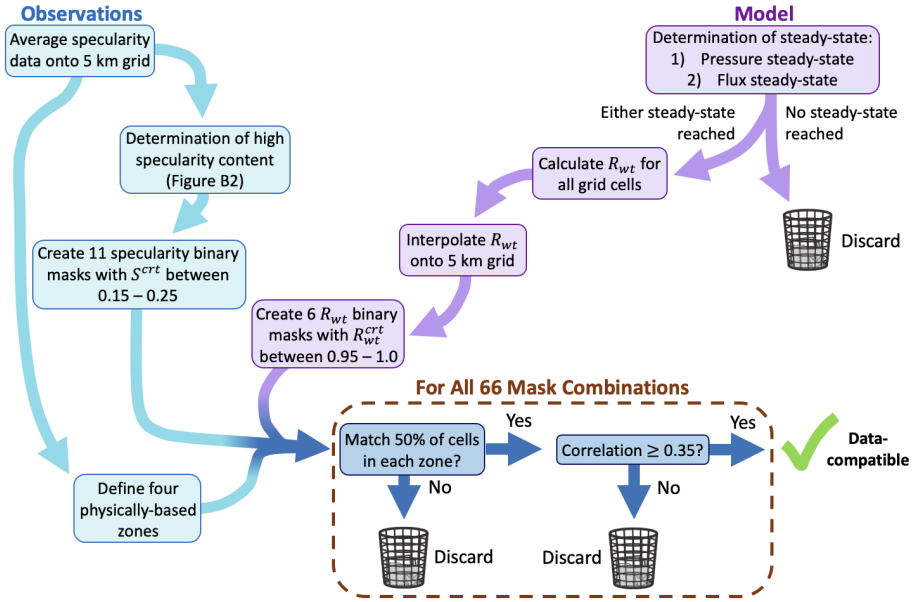

Figure B.1. Flow chart illustrating the step-by-step process for determining which model runs were compatible with observed specularity content.

Matching specularity and R_{wt} masks is a comparison between two spatial point patterns, which can be challenging as it requires a global statistic that can recognize local patterns of point clusters. Other comparisons of spatial point patterns have relied on segmenting the domain into areal units and determining an overall similarity statistic across all units (e.g., Andresen, 2009,1). The method developed in the current paper shares the concept of areal units by defining four physically-based zones within which we assess similarity between the two masks. These zones are intentionally chosen to loosely encompass regions of specularity or non-specularity, which allows for some spatial variability between masks and decreases the sensitivity to the zonal boundaries. We then require the two specularity and R_{wt} masks to match at 50% or more of grid points within

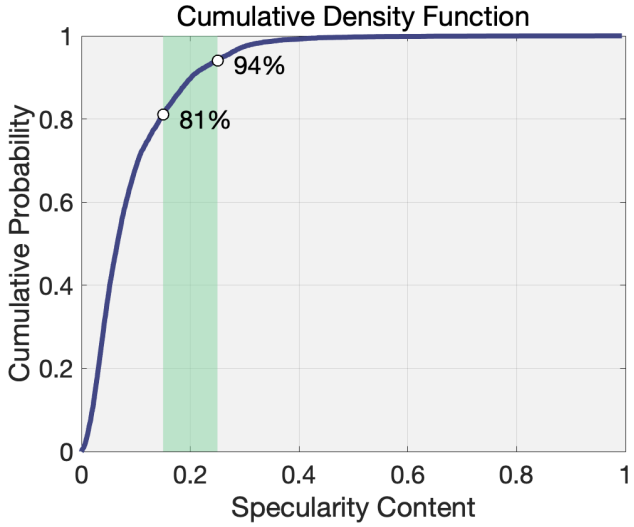

Figure B.2. Cumulative density function of observed specularity data from Schroeder et al. (2013). The green band highlights the range of specularity values used to create our 11 specularity masks, which are in the 81st to 94th percentile of our dataset.

each zone. As low specularity can occur for a variety of reasons, segmenting the domain into specularity-based zones does not predetermine a specific drainage style, but preserves the specular pattern of interest and allows us to test hypotheses concerning its formation.

While the first criterion does well by itself in selecting positive matches, it also selects many false positives. This occurs when the R_{wt} mask is almost entirely non-specular and over 50% of the cells in each zone is non-specular in the observed specularity mask (Figure B.3 h–i). It was therefore necessary to include a second criterion that can remove these false positives, which we do by requiring an overall correlation coefficient of $r \geq 0.35$. Correlations are calculated with:

$$r = \frac{\sum_m \sum_n (S_{mn} - \bar{S})(R_{mn} - \bar{R})}{\sqrt{(\sum_m \sum_n (S_{mn} - \bar{S})^2)(\sum_m \sum_n (R_{mn} - \bar{R})^2)}} \tag{B.1}$$

where S and R are the specularity and R_{wt} masks, respectively. Again, correlation by itself does a fair job at identifying positive matches, but it also identifies

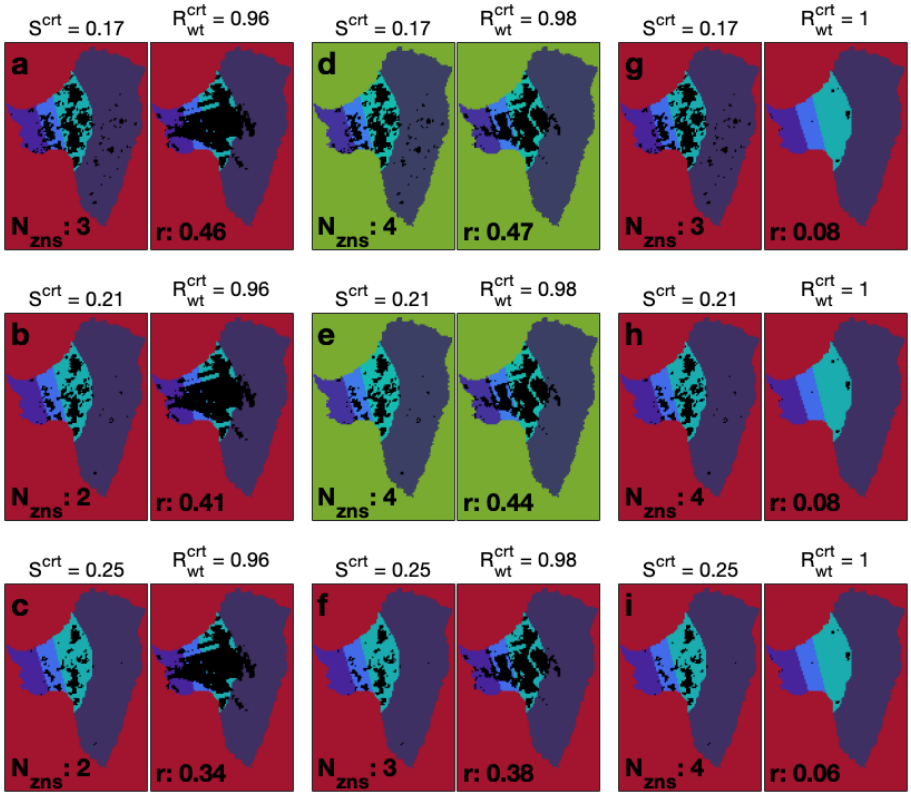

Figure B.3. Select S^{crt} (observed) and R^{crt}_{wt} (modeled) mask combinations from the $W_r = 0.1$ m, $c_s = 0.5$ m^{-1}, $k_q = 5 \times 10^{-2}$ m$^{7/4}$ kg$^{-1/2}$, $k_Q = 5 \times 10^{-4}$ m$^{7/4}$ kg$^{-1/2}$ model run, plotted over the four zones used for the first comparison criterion (also shown in Figures 2.3, 2.7). N_{zns} indicates the number of zones that meet Criterion 1, and r is the overall correlation between mask pairs. Background color indicates successful (green) and unsuccessful (red) matches. Values of S^{crt} and R^{crt}_{wt} used to make each mask are displayed above each plot.

false positives when the R_{wt} mask is overly specular (Figure B.3 a–b). As the two criteria fail for opposing reasons, they can check and balance each other if the thresholds are tuned appropriately (Figure B.3 d–e). We acknowledge this comparison method is sensitive to multiple choices of thresholds, so we attempt to make our criteria for selecting data-compatible runs as generous and inclusive as possible while still removing runs that clearly do a poor job at resembling observations. We empirically determined that requiring $\geq 50\%$ of cells in each zone

to agree and $r \geq 0.35$ works well at identifying positive matches and is sufficiently general to allow a reasonable variety of R_{wt} masks to pass this filtering process.

APPENDIX C

CHAPTER III: ADDITIONAL MODEL VALIDATION, TABLES, FIGURES, AND MOVIE CAPTIONS

C.1 Additional Model Validation

θ/S properties in MITgcm experiments showed a reasonable agreement to those observed for both winter and summer scenarios (Figures C.1 and C.2). Water properties from March/April 2016, our closest corollary to winter conditions, largely followed meltwater mixing lines, except for the thin surface layer, which included subglacial discharge. As we neglected subglacial discharge in winter experiments, modeled winter θ/S properties were what could be expected for late winter if no subglacial discharge and associated meltwater were present; however, this is unvalidated due to lack of proper winter observations. For summer experiments, the along-fjord range in water properties was well-aligned with observations, although pycnoclines were less prominent. In particular, the modeled 50 m pycnocline follows subglacial discharge mixing lines, while the starker observed pycnocline indicates mixing of additional submarine meltwater (Figure C.3). This suggests our model is neglecting a significant meltwater source.

The iceberg calving flux of LeConte Glacier is on the order of 4×10^6 m^3 d^{-1}, almost an order of magnitude less than subglacial discharge ($\sim 2 \times 10^7$ m^3 d^{-1}), but still greater than the submarine melt flux ($\sim 1.6 \times 10^6$ m^3 d^{-1}). Assuming most icebergs are too large to pass over S1 and thus completely melt before exited the fjord, iceberg meltwater would be expected to influence fjord conditions, and could therefore explain the discrepancies between our model and observations. It is possible other neglected freshwater sources, such as land runoff, could also influence any mismatch, although the total catchment size (150 km^2) of all streams emptying

into LeConte Bay is small compared to the LeConte Glacier catchment (535 km^2), so this effect is likely minimal.

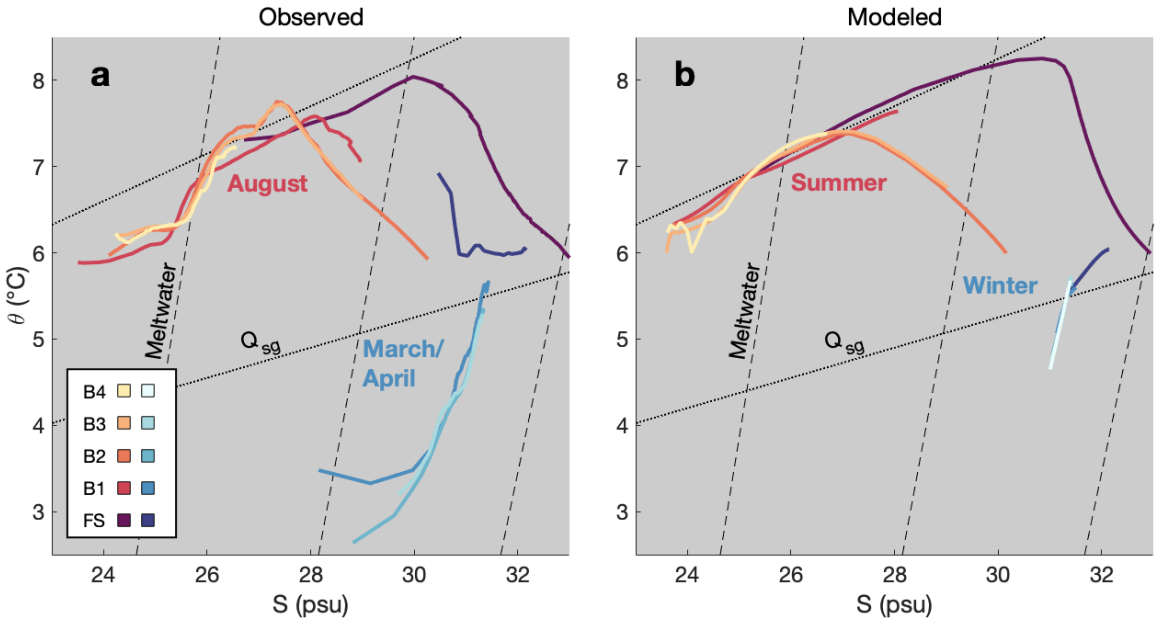

Figure C.1. **(a)** Average θ/S properties within each sub-basin and Frederick Sound for all CTD/VMP casts in August and March/April 2016, used to initialize MITgcm experiments. **(b)** Average steady-state θ/S properties from summer and winter MITgcm runs. Summer example is the neap tide, $Q_{sg} = 250$ m^3 s^{-1} experiment, which is most representative of forcing conditions during the August 2016 field survey. Dotted and dashed lines are subglacial discharge and submarine melt mixing lines. Note our winter formulation was initialized from springtime conditions when subglacial discharge was active, but was intended to resemble winter circulation when subglacial discharge was negligible. Thus, the drift from its initial condition is expected.

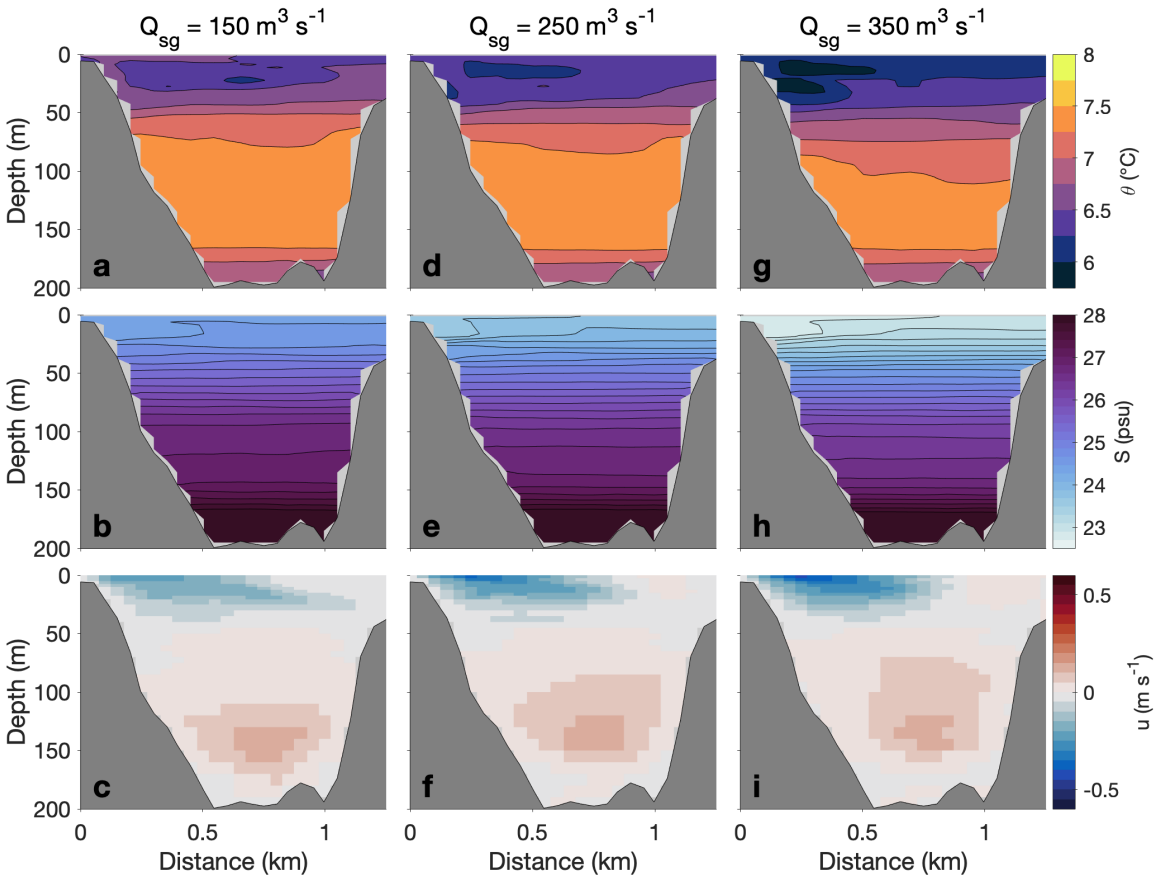

Figure C.2. Potential temperature, salinity, and glacierward velocity transects across S3 for neap tide summer MITgcm runs. For comparison with observations, transects are selected during the same tidal phase as Figure 7 d–f (neap ebb tide), and are plotted using the same color range and contour spacing. Subglacial discharge scenarios span the range present in Figure 7 d–f (175 – 320 m^3 s^{-1}).

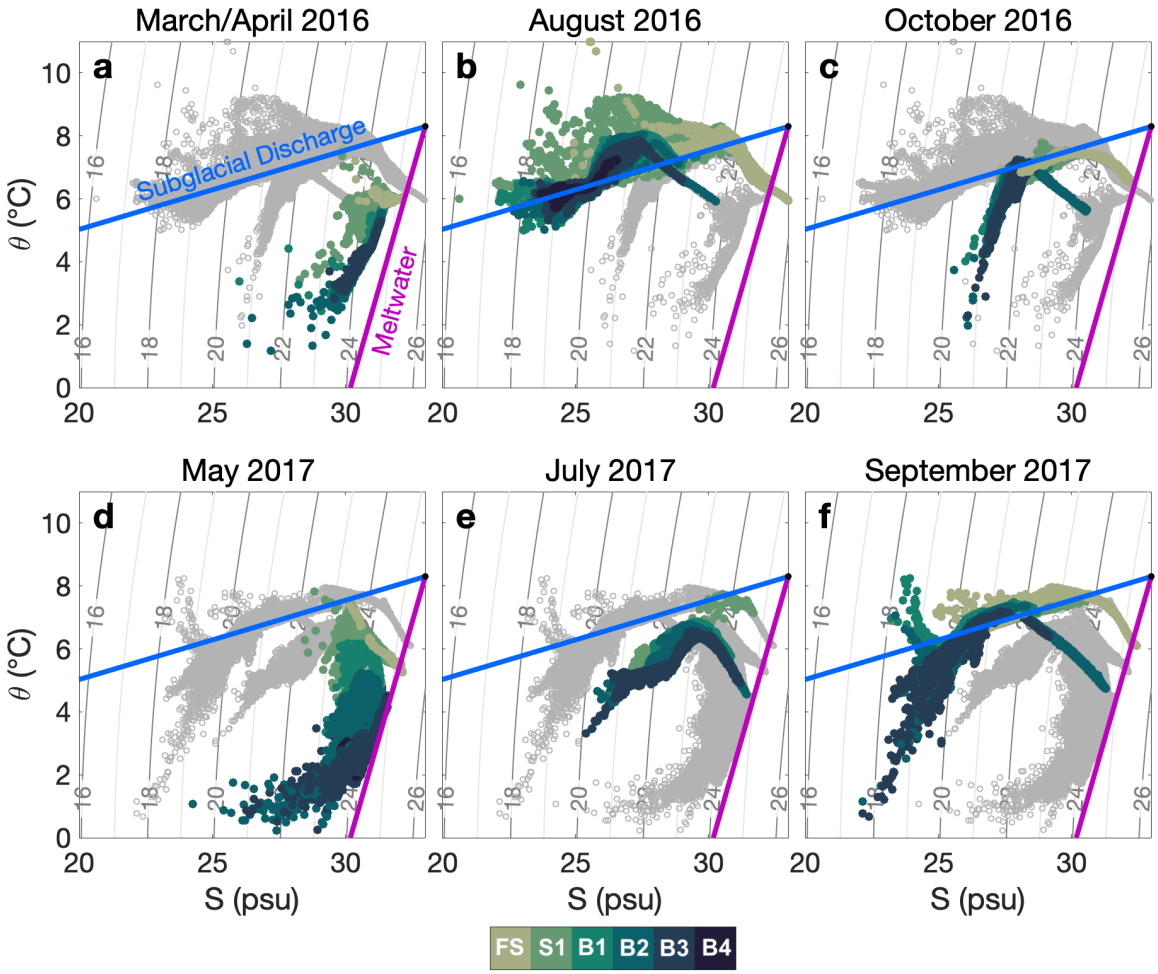

Figure C.3. θ/S data from all CTD casts from every survey, plotted with the general slopes of subglacial discharge and meltwater mixing lines. Casts are color-coded consistent with Figure 3. Gray circles are data from different surveys within the same year. Contours indicate the potential density anomaly.

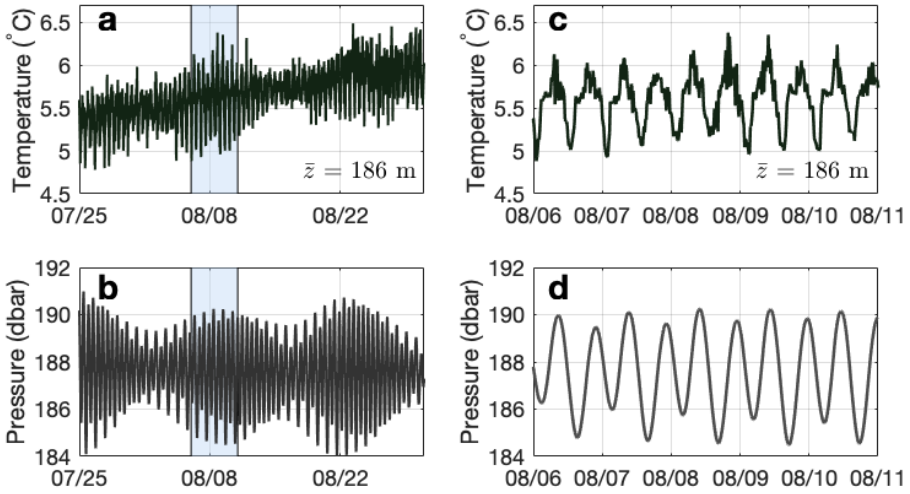

Figure C.4. Abridged time series from summer 2017 of **(a)** temperature and **(b)** pressure from the deepest Inner Mooring CTD, located at the base of the 165–185 pycnocline. **(c)** and **d)** are enlarged from the blue boxes in **a** and **b**, respectively. Plots show large semi-diurnal temperature fluctuations with amplitudes varying on spring-neap cycles, indicative of internal tides along the 165–185 m pycnocline.

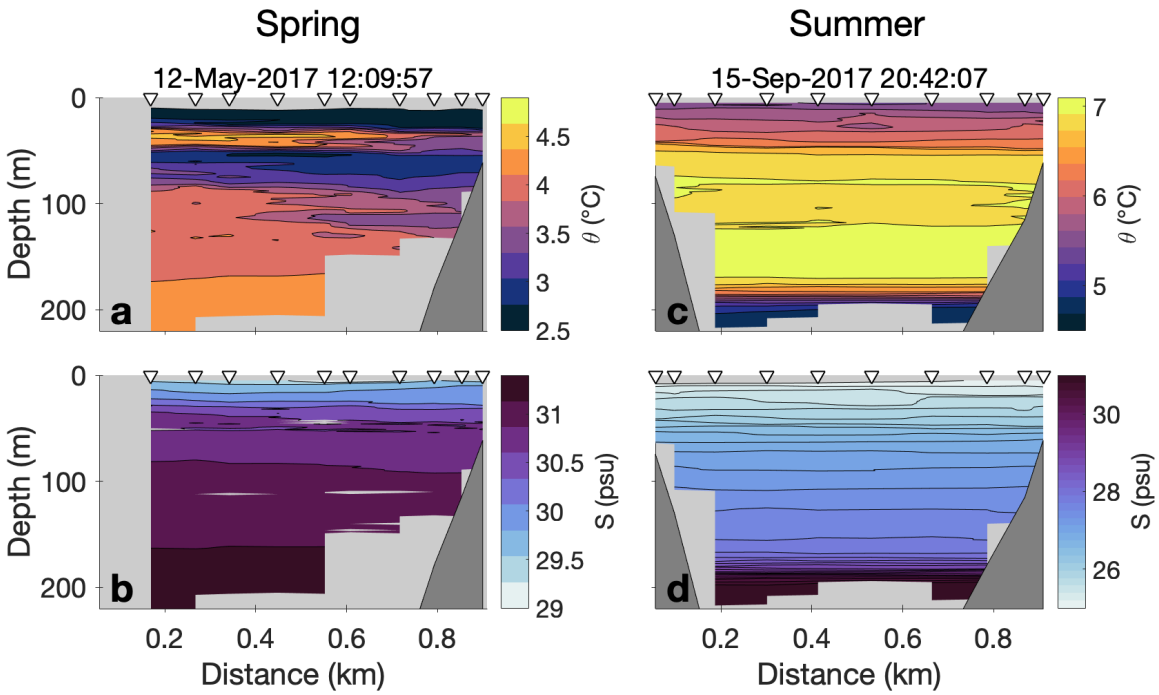

Figure C.5. Shipboard CTD surveys across B2 in **(a–b)** spring (May 2017) and **(c–d)** late summer (September 2017). The spring transect was measured during spring high tide, while the summer transect was during neap high tide (the median times for each transect are given). White triangles depict the locations of casts, also shown in Figure 1a. Note the differing color-scales between surveys. View is glacierward.

Table C.1. Subglacial discharge (Q_{sg}), reflux percent at S1 (α_{34}), reflux volume flux (Q_R), outflow volume flux (Q_{out}), inflow volume flux (Q_{in}), outflowing salinity (S_{out}), inflowing salinity (S_{in}), residence time (t_f), and area-weighted average temperature of glacier-adjacent cells (T_{gl}) for all MITgcm experiments. Reported fluxes and salinities are all calculated at the TEF transect glacierward of S1. All residence times account for reflux. Asterisks indicate runs that did not completely reach steady state.

Season	Tides	Q_{sg} (m^3 s^{-1})	α_{34} (%)	Q_R (m^3 s^{-1})	Q_{out} (m^3 s^{-1})	Q_{in} (m^3 s^{-1})	S_{out} (psu)	S_{in} (psu)	t_f (days)	T_{gl} (°C)
Summer	Neap	150	70	1,960	2,800	2,680	24.8	26.4	32.0	5.8
Summer	Neap	250	66.6	1,970	2,950	2,750	24.1	26.0	26.3	5.6
Summer	Neap	350	65.8	2,050	3,110	2,840	23.5	25.6	23.4	5.4
*Summer	Spring	150	58.4	2,070	3,540	3,430	25.7	27.7	13.1	6.0
Summer	Spring	250	57.0	2,140	3,750	3,570	25.1	27.4	12.1	5.9
Summer	Spring	350	57.0	2,250	3,950	3,680	24.6	27.0	11.6	5.8
*Winter	Neap	0	73.9	714	967	975	31.2	31.4	77.5	–

C.2 Supplementary Movie Captions

Movie S1 a and **b** depict thalweg Frederick Sound passive tracer concentrations for **(a)** the winter and **(b)** a summer (neap tides, $Q_{sg} = 250$ m^3 s^{-1}) MITgcm run (contour interval is 0.05%), along with the locations of the Outer (red) and Inner (green) moorings. **c** and **d** show the tidally-averaged passive tracer concentrations at select depths at the locations where the Outer (red color bar) and Inner (green color bar) moorings would be in our model. Notice the first and last 36 hours of the time series are removed due to the edge effects of the Godin filter.

Movie S2 (a) Subglacial discharge passive tracer concentration along the thalweg of the summer, neap tide, $Q_{sg} = 250$ m^3 s^{-1} MITgcm run (contour interval is 0.05%). **(b)** Tidally-averaged subglacial discharge passive tracer concentrations at select depths at the locations where the Outer (red color bar) and Inner (green color bar) moorings would be in our model. Notice the first and last 36 hours of the time series are removed due to the edge effects of the Godin filter. Locations of the Inner and Outer moorings are plotted as the green and red lines, respectively, in **a**.

APPENDIX D

CHAPTER IV: ADDITIONAL INFORMATION ON TEF AND EFFLUX/REFLUX THEORY, TABLES, AND FIGURES

D.1 TEF and Efflux/Reflux Theory

Efflux/reflux theory quantifies the net effect of mixing without the need to resolve individual mixing processes (Cokelet and Stewart, 1985). Effectively, efflux/reflux transports can be thought of as the vertical equivalent of the horizontal TEF budget (MacCready et al., 2021). In TEF terms, mass and volume conservation require:

$$\begin{aligned} \alpha^r_{in} Q^o_{in} + \alpha^e_{out} Q^g_{out} &= Q^o_{out} \\ \alpha^r_{in} S^o_{in} Q^o_{in} + \alpha^e_{out} S^g_{out} Q^g_{out} &= S^o_{out} Q^o_{out} \\ \alpha^e_{in} Q^o_{in} + \alpha^r_{out} Q^g_{out} &= Q^g_{in} \\ \alpha^e_{in} S^o_{in} Q^o_{in} + \alpha^r_{out} S^g_{out} Q^g_{out} &= S^g_{in} Q^g_{in} \end{aligned} \tag{D.1}$$

where superscripts o and g denote the TEF transports on the oceanward and glacierward sides of the mixing zone, respectively, and subscripts indicate whether the transport is inflowing (glacierward) or outflowing (oceanward). Superscripts on α signify the percent of the inflowing or outflowing layer that is refluxed ($\alpha^r_{in,out}$) or effluxed ($\alpha^e_{in,out}$) at the sill (Figure D.1). The solutions to Eq. D.1 are:

$$\begin{aligned} \alpha^r_{in} &= \frac{Q^o_{out}}{Q^o_{in}} \frac{S^o_{out} - S^g_{out}}{S^o_{in} - S^g_{out}} & \alpha^e_{out} &= \frac{Q^o_{out}}{Q^g_{out}} \frac{S^o_{in} - S^o_{out}}{S^o_{in} - S^g_{out}} \\ \alpha^e_{in} &= \frac{Q^g_{out}}{Q^o_{out}} \frac{S^g_{in} - S^g_{out}}{S^o_{in} - S^g_{out}} & \alpha^r_{out} &= \frac{Q^g_{in}}{Q^g_{out}} \frac{S^o_{in} - S^g_{in}}{S^o_{in} - S^g_{out}}. \end{aligned} \tag{D.2}$$

Mass and volume conservation also require:

$$\alpha^r_{in} + \alpha^e_{in} = 1$$
$$\alpha^r_{out} + \alpha^e_{out} = 1 \tag{D.3}$$

and

$$S^g_{out} \leq S^o_{out} < S^o_{in}$$
$$S^g_{out} < S^g_{in} \leq S^o_{in}. \tag{D.4}$$

TEF budgets are not exact and even at steady-state some drift still occurs within the mixing zone; therefore, we make minor adjustments to the TEF transports ensuring Eqs. D.1, D.3, and D.4 are satisfied before solving Eq. D.2 (e.g., Hager et al., 2022; MacCready et al., 2021), but the resultant error on α^r_{out} was $\leq 0.04\%$ of the reported value.

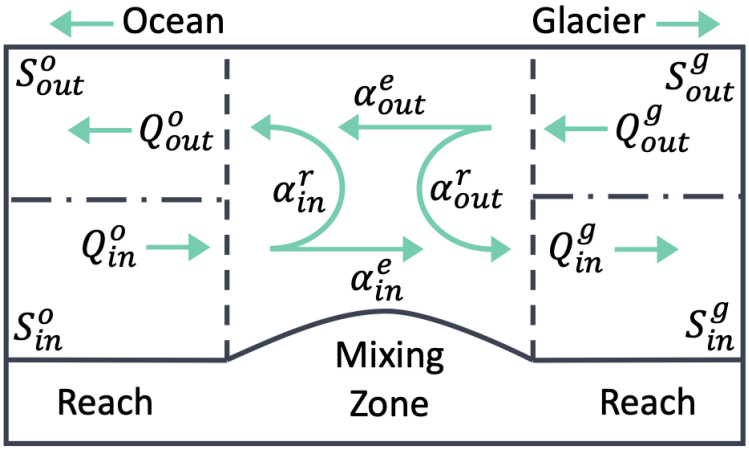

Figure D.1. Schematic illustrating each variable in efflux/reflux theory (Eq. D.1).

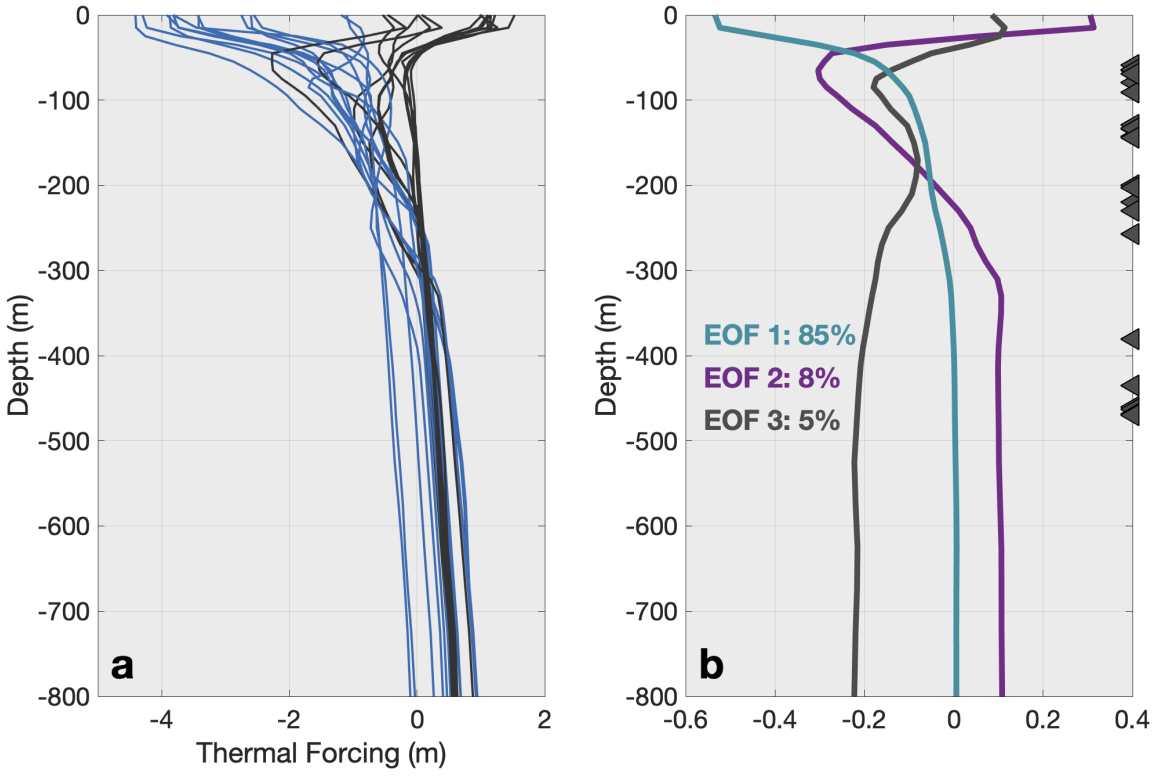

Figure D.2. **(a)** Near-glacier thermal forcing profiles from all iceberg (blue) and non-iceberg (gray) runs after removing the depth-average of each sill group. **(b)** The three dominant EOF modes with the percentage of variance they contribute, as calculated from the profiles in **a**. Gray triangles indicate terminal plume depths of all runs. The teal line represents variance from iceberg melting, the purple line indicates variance stemming from the boundary conditions, and the gray line signifies variance from subglacial discharge plumes.

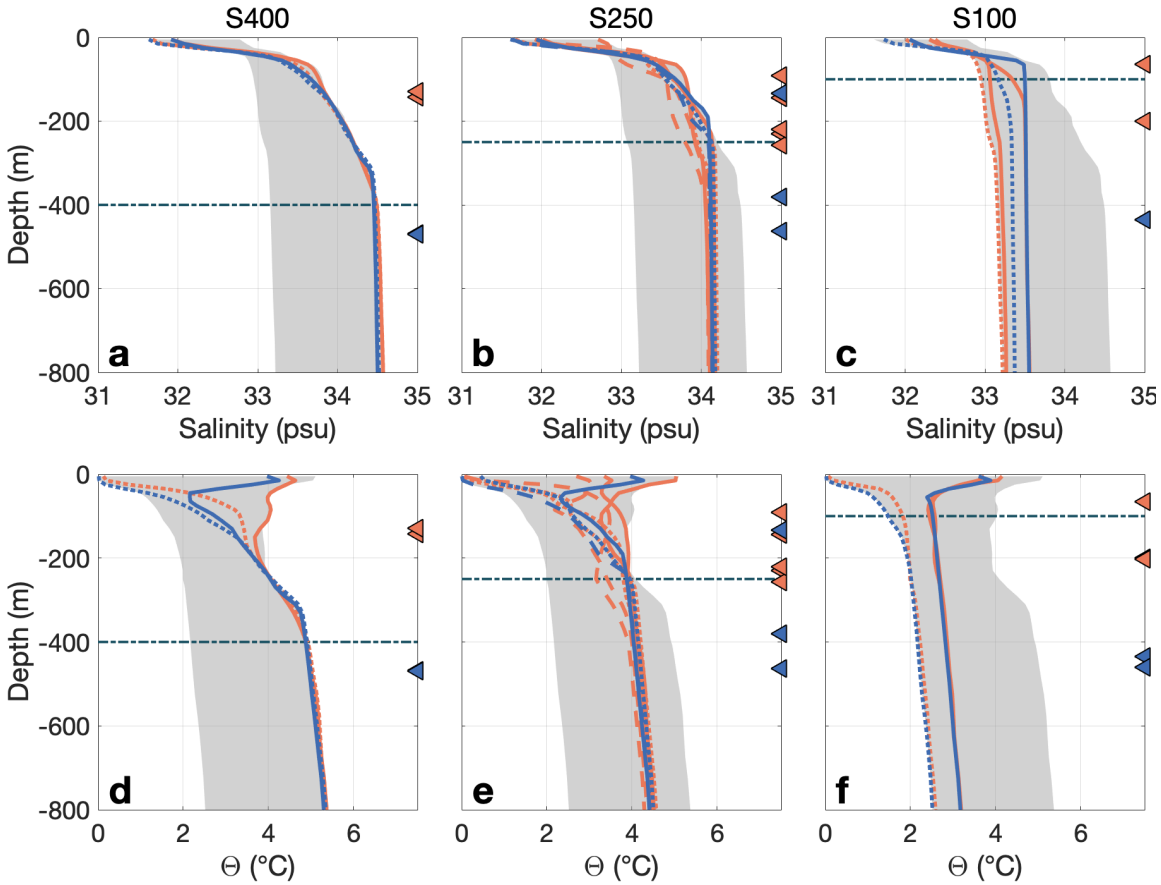

Figure D.3. Seasonal comparison of near-glacier **(a-c)** salinity and **(d-f)** thermal forcing profiles for select **(a,d)** S400, **(b,e)** S250, and **(c,f)** S100 runs. Orange lines depict summer profiles and blue lines depict winter profiles with otherwise equivalent forcing. Dotted lines represent iceberg runs, solid lines are non-iceberg runs, and dashed lines in **b** and **e** are profiles from a iceberg-choked, low resolution run. Triangles depict terminal plume depths for winter (blue) and summer (orange) runs. Gray shading depicts the range in salinity or thermal forcing across all runs. Dashed horizontal lines indicate sill depths.

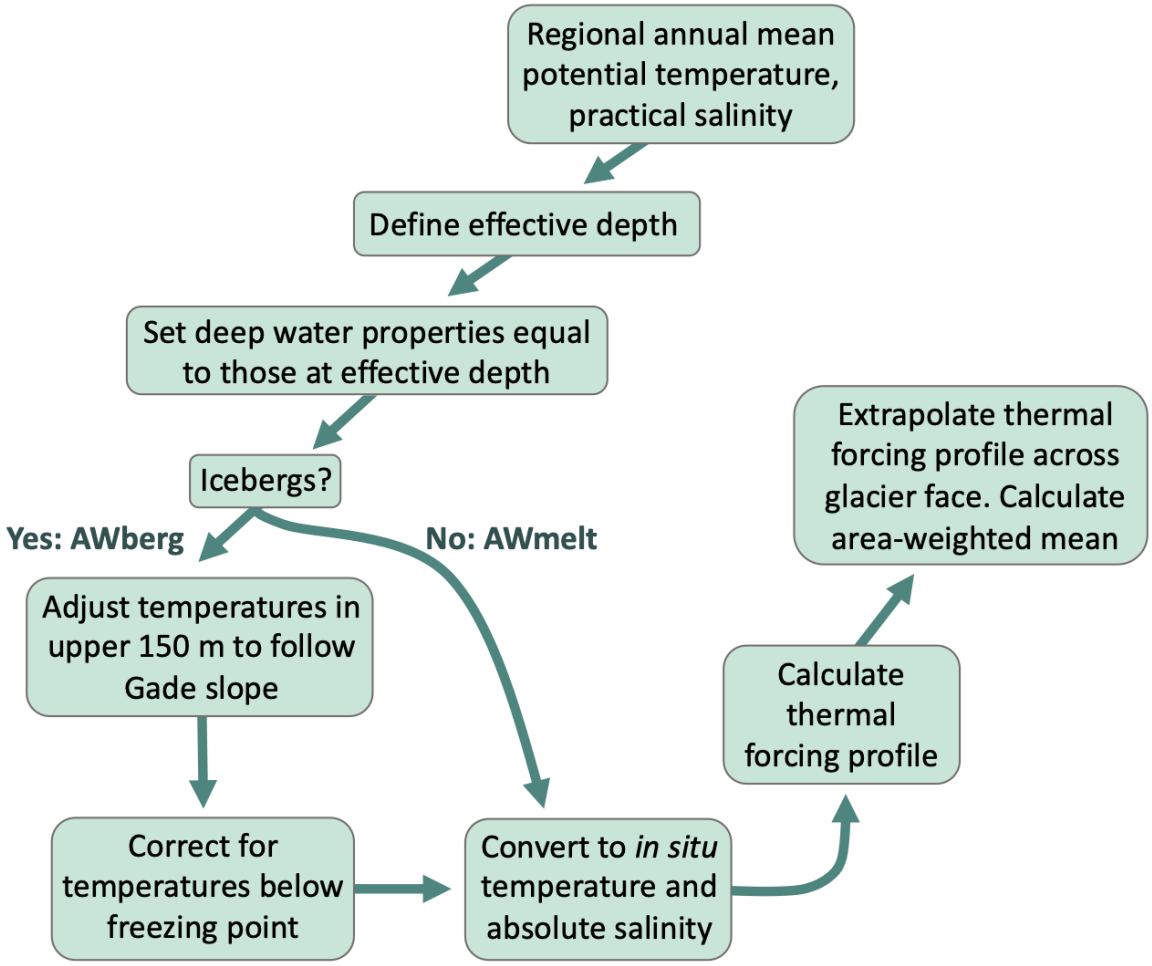

Figure D.4. Flow chart illustrating the step-by-step process for computing AWberg and AWmelt.

Table D.1. Fjord horizontal resolution (Res_H), maximum tidal velocity at the western open boundary (U_T), subglacial discharge (Q_{sg}) and plume type (L is line-plume; HC is half-conical plume), sill depth (Z_{sill}), maximum iceberg keel depth (Z_{berg}^{max}), maximum iceberg concentration (SA_{berg}^{max}), minimum iceberg concentration (SA_{berg}^{max}), area-weighted mean near-glacier thermal forcing ($\Theta_{\bar{A}}$), and reflux percent (α_{out}^{r}) for all runs.

Res_H (m)	U_T cm s^{-1}	Q_{sg} (m^3 s^{-1})	Z_{sill} (m)	Z_{berg}^{max} (m)	SA_{berg}^{max} (%)	SA_{berg}^{min} (%)	$\Theta_{\bar{A}}$ (°C)	α_{out}^{r} (%)
Summer	**Icebergs**							
200	0.5	300 (HC)	400	300	25	5	4.4	0.045
200	0.5	300 (HC)	400	300	75	5	4.4	0.12
200	0.5	300 (HC)	250	300	25	5	3.9	0.039
200	0.5	300 (HC)	250	300	75	5	3.8	0.024
200	0.5	300 (L)	250	300	75	5	3.8	24
200	0.5	300 (L)	100	300	75	5	2.1	70
200	0.5	300 (HC)	100	300	25	5	2.4	48
500	0.5	1000 (HC)	250	400	90	90	3.7	17
500	0.5	1000 (L)	250	400	90	90	3.7	24
Summer	**No Icebergs**							
200	0.5	300 (HC)	400				4.7	0.12
200	0.5	300 (HC)	250				4.1	16
200	0.5	300 (L)	250				4.1	41
200	0.7	300 (HC)	250				4.1	0.22
200	0.3	300 (HC)	250				4.1	8.8
200	0.5	300 (HC)	100				2.9	37
200	0.5	300 (L)	100				2.9	73
200	0.7	300 (HC)	100				2.9	37
200	0.3	300 (HC)	100				2.9	38
500	0.5	1000 (HC)	250				4	0.019
Winter	**Icebergs**							
200	0.5	10 (L)	400	300	75	5	4.2	26
200	0.5	10 (L)	250	300	75	5	3.8	0.024
200	0.5	10 (L)	100	300	75	5	2.0	68
500	0.5	10 (L)	250	400	90	90	3.6	16
Winter	**No Icebergs**							
200	0.5	10 (L)	400				4.4	46
200	0.5	10 (L)	250				3.9	66
200	0.5	10 (L)	100				2.9	75

Table D.2. Root mean square error of thermal forcing parameterizations for different groups of model runs.

Parameterization	Overall ($^\circ C$)	Icebergs ($^\circ C$)	No Icebergs ($^\circ C$)	S400 ($^\circ C$)	S250 ($^\circ C$)	S100 ($^\circ C$)
AWmelt	0.29	0.39	0.13	0.26	0.24	0.36
AWretreat	1.17	1.26	1.08	0.17	0.66	1.93
AWberg	0.26	0.17	0.34	0.15	0.19	0.39
AWconst	0.28	0.33	0.20	0.25	0.23	0.35
ISMIP6melt	0.74	0.90	0.53	1.12	0.69	0.44
ISMIP6retreat	1.31	1.40	1.22	0.31	0.83	2.1

REFERENCES CITED

Adusumilli, S., Fricker, H. A., Medley, B., Padman, L., and Siegfried, M. R. (2020). Interannual variations in meltwater input to the southern ocean from antarctic ice shelves. *Nature geoscience*, 13(9):616–620.

Alley, R. (1989). Water-pressure coupling of sliding and bed deformation: I. water system. *Journal of Glaciology*, 35(119):108–118.

Alley, R. B. (1996). Towards a hydrological model for computerized ice-sheet simulations. *Hydrological Processes*, 10(4):649–660.

Alley, R. B., Lawson, D. E., Evenson, E. B., Strasser, J. C., and Larson, G. J. (1998). Glaciohydraulic supercooling: a freeze-on mechanism to create stratified, debris-rich basal ice: Ii. theory. *Journal of Glaciology*, 44(148):563–569.

Amundson, J. M. and Carroll, D. (2018). Effect of topography on subglacial discharge and submarine melting during tidewater glacier retreat. *Journal of Geophysical Research: Earth Surface*, 123(1):66–79.

Amundson, J. M., Kienholz, C., Hager, A. O., Jackson, R. H., Motyka, R. J., Nash, J. D., and Sutherland, D. A. (2020). Formation, flow and break-up of ephemeral ice mélange at LeConte Glacier and Bay, Alaska. *Journal of Glaciology*, 66:577–590.

Andresen, M. A. (2009). Testing for similarity in area-based spatial patterns: A nonparametric monte carlo approach. *Applied Geography*, 29(3):333–345.

Andresen, M. A. (2016). An area-based nonparametric spatial point pattern test: The test, its applications, and the future. *Methodological Innovations*, 9:2059799116630659.

Andrews, L. C., Catania, G. A., Hoffman, M. J., Gulley, J. D., Lüthi, M. P., Ryser, C., Hawley, R. L., and Neumann, T. A. (2014). Direct observations of evolving subglacial drainage beneath the greenland ice sheet. *Nature*, 514(7520):80–83.

Asay-Davis, X. S., Cornford, S. L., Durand, G., Galton-Fenzi, B. K., Gladstone, R. M., Gudmundsson, G. H., Hattermann, T., Holland, D. M., Holland, D., Holland, P. R., et al. (2016). Experimental design for three interrelated marine ice sheet and ocean model intercomparison projects: Mismip v. 3 (mismip+), isomip v. 2 (isomip+) and misomip v. 1 (misomip1). *Geoscientific Model Development*, 9(7):2471–2497.

Asay-Davis, X. S., Jourdain, N. C., and Nakayama, Y. (2017). Developments in simulating and parameterizing interactions between the southern ocean and the antarctic ice sheet. *Current Climate Change Reports*, 3(4):316–329.

Bamber, J., Tedstone, A., King, M., Howat, I., Enderlin, E., Van Den Broeke, M., and Noel, B. (2018). Land ice freshwater budget of the Arctic and North Atlantic Oceans: 1. Data, methods, and results. *Journal of Geophysical Research: Oceans*, 123(3):1827–1837.

Bamber, J., Van Den Broeke, M., Ettema, J., Lenaerts, J., and Rignot, E. (2012). Recent large increases in freshwater fluxes from Greenland into the North Atlantic. *Geophysical Research Letters*, 39(19).

Bartholomaus, T. C., Stearns, L. A., Sutherland, D. A., Shroyer, E. L., Nash, J. D., Walker, R. T., Catania, G., Felikson, D., Carroll, D., Fried, M. J., et al. (2016). Contrasts in the response of adjacent fjords and glaciers to ice-sheet surface melt in West Greenland. *Annals of Glaciology*, 57(73):25–38.

Bevan, S. L., Luckman, A. J., Benn, D. I., Adusumilli, S., and Crawford, A. (2021). Brief communication: Thwaites glacier cavity evolution. *The Cryosphere Discussions*, pages 1–12.

Bevis, M., Harig, C., Khan, S. A., Brown, A., Simons, F. J., Willis, M., Fettweis, X., Van Den Broeke, M. R., Madsen, F. B., Kendrick, E., et al. (2019). Accelerating changes in ice mass within greenland, and the ice sheet's sensitivity to atmospheric forcing. *Proceedings of the National Academy of Sciences*, 116(6):1934–1939.

Bjornsson, H. (1992). Jokulhlaups in iceland: prediction, characteristics and simulation. *Annals of Glaciology*, 16:95–106.

Black, T. E. and Joughin, I. (2022). Multi-decadal retreat of marine-terminating outlet glaciers in northwest and central-west greenland. *The Cryosphere*, 16(3):807–824.

Brinkerhoff, D., Aschwanden, A., and Fahnestock, M. (2021). Constraining subglacial processes from surface velocity observations using surrogate-based bayesian inference. *Journal of Glaciology*, 67(263):385–403.

Brinkerhoff, D. J., Meyer, C. R., Bueler, E., Truffer, M., and Bartholomaus, T. C. (2016). Inversion of a glacier hydrology model. *Annals of Glaciology*, 57(72):84–95.

Bueler, E. and van Pelt, W. (2015). Mass-conserving subglacial hydrology in the parallel ice sheet model version 0.6. *Geoscientific Model Development*, 8:1613–1635.

Burchard, H., Bolding, K., Feistel, R., Gräwe, U., Klingbeil, K., MacCready, P., Mohrholz, V., Umlauf, L., and van der Lee, E. M. (2018). The Knudsen theorem and the Total Exchange Flow analysis framework applied to the Baltic Sea. *Progress in Oceanography*, 165:268–286.

Carroll, D., Sutherland, D. A., Curry, B., Nash, J. D., Shroyer, E. L., Catania, G. A., Stearns, L. A., Grist, J. P., Lee, C. M., and de Steur, L. (2018). Subannual and Seasonal Variability of Atlantic-Origin Waters in Two Adjacent West Greenland Fjords. *Journal of Geophysical Research: Oceans*, 123:6670–6687.

Carroll, D., Sutherland, D. A., Hudson, B., Moon, T., Catania, G. A., Shroyer, E. L., Nash, J. D., Bartholomaus, T. C., Felikson, D., Stearns, L. A., et al. (2016). The impact of glacier geometry on meltwater plume structure and submarine melt in Greenland fjords. *Geophysical Research Letters*, 43(18):9739–9748.

Carroll, D., Sutherland, D. A., Shroyer, E. L., Nash, J. D., Catania, G. A., and Stearns, L. A. (2015). Modeling turbulent subglacial meltwater plumes: Implications for fjord-scale buoyancy-driven circulation. *Journal of Physical Oceanography*, 45:2169–2185.

Carroll, D., Sutherland, D. A., Shroyer, E. L., Nash, J. D., Catania, G. A., and Stearns, L. A. (2017). Subglacial discharge-driven renewal of tidewater glacier fjords. *Journal of Geophysical Research: Oceans*, 122(8):6611–6629.

Carter, S. and Fricker, H. (2012). The supply of subglacial meltwater to the grounding line of the siple coast, west antarctica. *Annals of Glaciology*, 53(60):267–280.

Carter, S. P., Fricker, H. A., and Siegfried, M. R. (2017). Antarctic subglacial lakes drain through sediment-floored canals: theory and model testing on real and idealized domains. *The Cryosphere*, 11(1):381–405.

Chandler, D. M., Wadham, J. L., Lis, G. P., Cowton, T., a. Sole, Bartholomew, I., Telling, J., Nienow, P., Bagshaw, E. B., Mair, D., Vinen, S., and Hubbard, A. (2013). Evolution of the subglacial drainage system beneath the greenland ice sheet revealed by tracers. *Nature Geoscience*, 6:195–198.

Chow, V. T. (1959). *Open-channel hydraulics*. McGraw-Hill, New York.

Christensen, J. H., Kanikicharla, K. K., Aldrian, E., An, S. I., Cavalcanti, I. F. A., de Castro, M., Dong, W., Goswami, P., Hall, A., Kanyanga, J. K., et al. (2013). Climate phenomena and their relevance for future regional climate change. In *Climate change 2013 the physical science basis: Working group I contribution to the Fifth Assessment Report of the Intergovernmental Panel on Climate Change*, pages 1217–1308. Cambridge University Press.

Chu, W., Schroeder, D. M., Seroussi, H., Creyts, T. T., Palmer, S. J., and Bell, R. E. (2016). Extensive winter subglacial water storage beneath the greenland ice sheet. *Geophysical Research Letters*, 43(24):12–484.

Clarke, G. K. (1982). Glacier outburst floods from "hazard lake", yukon territory, and the problem of flood magnitude prediction. *Journal of Glaciology*, 28(98):3–21.

Clarke, G. K. (1987). Subglacial till: a physical framework for its properties and processes. *Journal of Geophysical Research: Solid Earth*, 92(B9):9023–9036.

Clarke, G. K. (2003). Hydraulics of subglacial outburst floods: new insights from the spring–hutter formulation. *Journal of Glaciology*, 49(165):299–313.

Cokelet, E. D. and Stewart, R. J. (1985). The Exchange of Water in Fjords: The Effiux/Reflux Theory of Advective Reaches Separated by Mixing Zones. *Journal of Geophysical Research*, 90:7287–7306.

Cook, S. J., Christoffersen, P., Todd, J., Slater, D., and Chauché, N. (2020). Coupled modelling of subglacial hydrology and calving-front melting at store glacier, west greenland. *The Cryosphere*, 14(3):905–924.

Cornford, S. L., Seroussi, H., Asay-Davis, X. S., Gudmundsson, G. H., Arthern, R., Borstad, C., Christmann, J., Dias dos Santos, T., Feldmann, J., Goldberg, D., et al. (2020). Results of the third marine ice sheet model intercomparison project (mismip+). *The Cryosphere*, 14(7):2283–2301.

Cowton, T., Slater, D., Sole, A., Goldberg, D., and Nienow, P. (2015). Modeling the impact of glacial runoff on fjord circulation and submarine melt rate using a new subgrid-scale parameterization for glacial plumes. *Journal of Geophysical Research: Oceans*, 120(2):796–812.

Cowton, T., Sole, A. J., Nienow, P. W., Slater, D. A., and Christoffersen, P. (2018). Linear response of east greenland's tidewater glaciers to ocean/atmosphere warming. *Proceedings of the National Academy of Sciences*, 115(31):7907–7912.

Davison, B. J., Cowton, T., Sole, A., Cottier, F., and Nienow, P. (2022). Modelling the effect of submarine iceberg melting on glacier-adjacent water properties. *The Cryosphere*, 16(4):1181–1196.

Davison, B. J., Cowton, T. R., Cottier, F. R., and Sole, A. J. (2020). Iceberg melting substantially modifies oceanic heat flux towards a major Greenlandic tidewater glacier. *Nature Communications*, 11.

de Fleurian, B., Werder, M. A., Beyer, S., Brinkerhoff, D. J., Delaney, I., Dow, C. F., Downs, J., Gagliardini, O., Hoffman, M. J., Hooke, R. L., et al. (2018). Shmip the subglacial hydrology model intercomparison project. *Journal of Glaciology*, 64(248):897–916.

Dieng, H.-B., Cazenave, A., Meyssignac, B., and Ablain, M. (2017). New estimate of the current rate of sea level rise from a sea level budget approach. *Geophysical Research Letters*, 44(8):3744–3751.

Dow, C., McCormack, F., Young, D., Greenbaum, J., Roberts, J., and Blankenship, D. (2020). Totten glacier subglacial hydrology determined from geophysics and modeling. *Earth and Planetary Science Letters*, 531:115961.

Dow, C. F., Kulessa, B., Rutt, I., Doyle, S., and Hubbard, A. (2014). Upper bounds on subglacial channel development for interior regions of the greenland ice sheet. *Journal of Glaciology*, 60:1044–1052.

Downs, J. Z., Johnson, J. V., Harper, J. T., Meierbachtol, T., and Werder, M. A. (2018). Dynamic hydraulic conductivity reconciles mismatch between modeled and observed winter subglacial water pressure. *Journal of Geophysical Research: Earth Surface*, 123:818–836.

Drews, R., Pattyn, F., Hewitt, I. J., Ng, F. S. L., Berger, S., Matsuoka, K., Helm, V., Bergeot, N., Favier, L., and Neckel, N. (2017). Actively evolving subglacial conduits and eskers initiate ice shelf channels at an antarctic grounding line. *Nature Communications*, 8:15228.

Ebbesmeyer, C. C. and Barnes, C. A. (1980). Control of a fjord basin's dynamics by tidal mixing in embracing sill zones. *Estuarine and Coastal Marine Science*, 11(3):311–330.

Echelmeyer, K. and Harrison, W. D. (1990). Jakobshavns Isbræ, West Greenland: Seasonal variations in velocity-or lack thereof. *Journal of Glaciology*, 36(122):82–88.

Eidam, E. F., Sutherland, D. A., Duncan, D., Kienholz, C., Amundson, J. M., and Motyka, R. J. (2020). Morainal Bank Evolution and Impact on Terminus Dynamics During a Tidewater Glacier Stillstand. *Journal of Geophysical Research: Earth Surface*, 125.

Enderlin, E. M., Hamilton, G. S., Straneo, F., and Sutherland, D. A. (2016). Iceberg meltwater fluxes dominate the freshwater budget in Greenland's iceberg-congested glacial fjords. *Geophysical Research Letters*, 43:11,287–11,294.

Enderlin, E. M., Howat, I. M., Jeong, S., Noh, M.-J., Van Angelen, J. H., and Van Den Broeke, M. R. (2014). An improved mass budget for the greenland ice sheet. *Geophysical Research Letters*, 41(3):866–872.

Engelhardt, H. and Kamb, B. (1997). Basal hydraulic system of a west antarctic ice stream: constraints from borehole observations. *Journal of Glaciology*, 43(144):207–230.

Fahrner, D., Lea, J. M., Brough, S., Mair, D. W., and Abermann, J. (2021). Linear response of the greenland ice sheet's tidewater glacier terminus positions to climate. *Journal of Glaciology*, 67(262):193–203.

Farmer, D. M. and Freeland, H. J. (1983). The Physical Oceanography of Fjords. *Progress in Oceanography*, 12:147–220.

Flowers, G. E. (2015). Modelling water flow under glaciers and ice sheets. *Proceedings of the Royal Society A: Mathematical, Physical and Engineering Sciences*, 471:20140907.

Flowers, G. E. and Clarke, G. K. (2002). A multicomponent coupled model of glacier hydrology 1. theory and synthetic examples. *Journal of Geophysical Research: Solid Earth*, 107(B11):ECV–9.

Fountain, A. G. and Walder, J. S. (1998). Water flow through temperate glaciers. *Reviews of Geophysics*, 36(3):299–328.

Fowler, A. (1987). Sliding with cavity formation. *Journal of Glaciology*, 33(115):255–267.

Fowler, A. (1999). Breaking the seal at grímsvötn, iceland. *Journal of Glaciology*, 45(151):506–516.

Gade, H. and Edwards, A. (1980). Deep water renewal in fjords. In *Fjord Oceanography*, pages 453–489. Springer.

Gade, H. G. (1979). Melting of ice in sea water: A primitive model with application to the antarctic ice shelf and icebergs. *Journal of Physical Oceanography*, 9(1):189–198.

Gardner, A. S., Moholdt, G., Cogley, J. G., Wouters, B., Arendt, A. A., Wahr, J., Berthier, E., Hock, R., Pfeffer, W. T., Kaser, G., et al. (2013). A reconciled estimate of glacier contributions to sea level rise: 2003 to 2009. *Science*, 340(6134):852–857.

Gardner, A. S., Moholdt, G., Scambos, T., Fahnstock, M., Ligtenberg, S., Broeke, M. v. d., and Nilsson, J. (2018). Increased west antarctic and unchanged east antarctic ice discharge over the last 7 years. *The Cryosphere*, 12(2):521–547.

Geyer, W. and Cannon, G. (1982). Sill processes related to deep water renewal in a fjord. *Journal of Geophysical Research*, 87:7985.

Geyer, W. and Ralston, D. (2011). The dynamics of strongly stratified estuaries. *Treatise on Estuarine and Coastal Science. Amsterdam: Elsevier*, pages 37–52.

Gillet-Chaulet, F., Durand, G., Gagliardini, O., Mosbeux, C., Mouginot, J., Rémy, F., and Ritz, C. (2016). Assimilation of surface velocities acquired between 1996 and 2010 to constrain the form of the basal friction law under pine island glacier. *Geophysical Research Letters*, 43(19):10–311.

Gillibrand, P. A., Inall, M. E., Portilla, E., and Tett, P. (2013). A box model of the seasonal exchange and mixing in regions of restricted exchange: application to two contrasting scottish inlets. *Environmental modelling & software*, 43:144–159.

Gillibrand, P. A., Turrell, W. R., and Elliott, A. J. (1995). Deep-water renewal in the upper basin of Loch Sunart, a Scottish fjord. *Journal of Physical Oceanography*, 25(6):1488–1503.

Gladish, C. V., Holland, D. M., Rosing-Asvid, A., Behrens, J. W., and Boje, J. (2015). Oceanic boundary conditions for jakobshavn glacier. part i: Variability and renewal of ilulissat icefjord waters, 2001–14. *Journal of Physical Oceanography*, 45(1):3–32.

Goelzer, H., Nowicki, S., Payne, A., Larour, E., Seroussi, H., Lipscomb, W. H., Gregory, J., Abe-Ouchi, A., Shepherd, A., Simon, E., et al. (2020). The future sea-level contribution of the greenland ice sheet: a multi-model ensemble study of ismip6. *The Cryosphere*, 14(9):3071–3096.

Golaz, J.-C., Caldwell, P. M., Van Roekel, L. P., Petersen, M. R., Tang, Q., Wolfe, J. D., Abeshu, G., Anantharaj, V., Asay-Davis, X. S., Bader, D. C., et al. (2019). The doe e3sm coupled model version 1: Overview and evaluation at standard resolution. *Journal of Advances in Modeling Earth Systems*, 11(7):2089–2129.

Gordon, S., Sharp, M., Hubbard, B., Smart, C., Ketterling, B., and Willis, I. (1998). Seasonal reorganization of subglacial drainage inferred from measurements in boreholes. *Hydrological Processes*, 12(1):105–133.

Gulley, J., Walthard, P., Martin, J., a.F. Banwell, Benn, D., and Catania, G. (2012). Conduit roughness and dye-trace breakthrough curves: why slow velocity and high dispersivity may not reflect flow in distributed systems. *Journal of Glaciology*, 58:915–925.

Hager, A. O., Sutherland, D. A., Amundson, J. M., Jackson, R. H., Kienholz, C., Motyka, R. J., and Nash, J. D. (2022). Subglacial discharge reflux and buoyancy forcing drive seasonality in a silled glacial fjord. *Journal of Geophysical Research: Oceans*, page e2021JC018355.

Harig, C. and Simons, F. J. (2015). Accelerated west antarctic ice mass loss continues to outpace east antarctic gains. *Earth and Planetary Science Letters*, 415:134–141.

Hasholt, B., Hansen, B. U., Humlum, O., and Mernild, S. H. (2004). Meteorological stations at the sermilik station, southeast greenland: Physical environment and meteorological observations 2002. *Geografisk Tidsskrift-Danish Journal of Geography*, 104(2):47–58.

Haynes, M. S., Chapin, E., and Schroeder, D. M. (2018). Geometric power fall-off in radar sounding. *IEEE Transactions on Geoscience and Remote Sensing*, 56(11):6571–6585.

Helm, V., Humbert, A., and Miller, H. (2014). Elevation and elevation change of greenland and antarctica derived from cryosat-2. *The Cryosphere*, 8(4):1539–1559.

Hewitt, I. (2013). Seasonal changes in ice sheet motion due to melt water lubrication. *Earth and Planetary Science Letters*, 371:16–25.

Hewitt, I. J. (2011). Modelling distributed and channelized subglacial drainage: the spacing of channels. *Journal of Glaciology*, 57:302–314.

Hock, R. (1999). A distributed temperature-index ice-and snowmelt including potential direct solar radiation. *Journal of Glaciology*, 45.

Hock, R. and Noetzli, C. (1997). Areal melt and discharge modelling of Storglaciären, Sweden. *Annals of Glaciology*, 24.

Hoffman, M. J., Andrews, L. C., Price, S. F., Catania, G. A., Neumann, T. A., Lüthi, M. P., Gulley, J., Ryser, C., Hawley, R. L., and Morriss, B. (2016). Greenland subglacial drainage evolution regulated by weakly connected regions of the bed. *Nature communications*, 7(1):1–12.

Hoffman, M. J., Asay-Davis, X., Price, S. F., Fyke, J., and Perego, M. (2019). Effect of Subshelf Melt Variability on Sea Level Rise Contribution From Thwaites Glacier, Antarctica. *Journal of Geophysical Research: Earth Surface*, 124(12):2798–2822.

Hoffman, M. J., Perego, M., Price, S. F., Lipscomb, W. H., Jacobsen, D., Tezaur, I., Salinger, A. G., Tuminaro, R., and Zhang, T. (2018). MPAS-Albany Land Ice (MALI): A variable resolution ice sheet model for Earth system modeling using Voronoi grids. *Geoscientific Model Development*, pages 1–47.

Hoffman, M. J. and Price, S. (2014). Feedbacks between coupled subglacial hydrology and glacier dynamics. *Journal of Geophysical Research: Earth Surface*, 119:1–23.

Hogan, K. A., Larter, R. D., Graham, A. G., Arthern, R., Kirkham, J. D., Totten Minzoni, R., Jordan, T. A., Clark, R., Fitzgerald, V., Wåhlin, A. K., et al. (2020). Revealing the former bed of thwaites glacier using sea-floor bathymetry: implications for warm-water routing and bed controls on ice flow and buttressing. *The Cryosphere*, 14(9):2883–2908.

Holland, D. M., Thomas, R. H., De Young, B., Ribergaard, M. H., and Lyberth, B. (2008). Acceleration of Jakobshavn Isbræ triggered by warm subsurface ocean waters. *Nature geoscience*, 1(10):659–664.

Holschuh, N., Christianson, K., Paden, J., Alley, R., and Anandakrishnan, S. (2020). Linking postglacial landscapes to glacier dynamics using swath radar at thwaites glacier, antarctica. *Geology*, 48(3):268–272.

Howard, S. and Padman, L. (2021). Gr1kmTM: Greeland 1 kilometer Tide Model. *Arctic Data Center*.

Iken, A. and Bindschadler, R. A. (1986). Combined measurements of subglacial water pressure and surface velocity of findelengletscher, switzerland: Conclusions about drainage system and sliding mechanism. *Journal of Glaciology*, 32(110):101–119.

Irarrazaval, I., Werder, M. A., Huss, M., Herman, F., and Mariethoz, G. (2021). Determining the evolution of an alpine glacier drainage system by solving inverse problems. *Journal of Glaciology*, 67(263):421–434.

Jackson, R. H., Nash, J. D., Kienholz, C., Sutherland, D. A., Amundson, J. M., Motyka, R. J., Winters, D., Skyllingstad, E., and Pettit, E. C. (2020). Meltwater Intrusions Reveal Mechanisms for Rapid Submarine Melt at a Tidewater Glacier. *Geophysical Research Letters*, 47.

Jackson, R. H., Shroyer, E. L., Nash, J. D., Sutherland, D. A., Carroll, D., Fried, M. J., Catania, G. A., Bartholomaus, T. C., and Stearns, L. A. (2017). Near-glacier surveying of a subglacial discharge plume: Implications for plume parameterizations. *Geophysical Research Letters*, 44:6886–6894.

Jackson, R. H. and Straneo, F. (2016). Heat, salt, and freshwater budgets for a glacial fjord in Greenland. *Journal of Physical Oceanography*, 46:2735–2768.

Jackson, R. H., Straneo, F., and Sutherland, D. A. (2014). Externally forced fluctuations in ocean temperature at Greenland glaciers in non-summer months. *Nature Geoscience*, 7(7):503–508.

Jakobsson, M., Mayer, L. A., Nilsson, J., Stranne, C., Calder, B., O'Regan, M., Farrell, J. W., Cronin, T. M., Brüchert, V., Chawarski, J., et al. (2020). Ryder glacier in northwest greenland is shielded from warm atlantic water by a bathymetric sill. *Communications Earth & Environment*, 1(1):1–10.

Jenkins, A. (2011). Convection-driven melting near the grounding lines of ice shelves and tidewater glaciers. *Journal of Physical Oceanography*, 41(12):2279–2294.

Joughin, I., Alley, R. B., and Holland, D. M. (2012). Ice-sheet response to oceanic forcing. *Science*, 338(6111):1172–1176.

Joughin, I., Smith, B. E., and Medley, B. (2014). Marine ice sheet collapse potentially underway for the thwaites glacier basin, west antarctica. *Science*, 344:735–738.

Joughin, I., Smith, B. E., and Schoof, C. G. (2019). Regularized coulomb friction laws for ice sheet sliding: Application to pine island glacier, antarctica. *Geophysical Research Letters*, 46:4764–4771.

Joughin, I., Tulaczyk, S., Bamber, J. L., Blankenship, D., Holt, J. W., Scambos, T., and Vaughan, D. G. (2009). Basal conditions for pine island and thwaites glaciers, west antarctica, determined using satellite and airborne data. *Journal of Glaciology*, 55:245–257.

Jourdain, N. C., Asay-Davis, X., Hattermann, T., Straneo, F., Seroussi, H., Little, C. M., and Nowicki, S. (2020). A protocol for calculating basal melt rates in the ismip6 antarctic ice sheet projections. *The Cryosphere*, 14(9):3111–3134.

Kajanto, K., Straneo, F., and Nisancioglu, K. (2022). Impact of icebergs on the seasonal submarine melt of sermeq kujalleq. *The Cryosphere Discussions*, pages 1–26.

Kamb, B. (1987). Glacier surge mechanism based on linked cavity configuration of the basal water conduit system. *Journal of Geophysical Research: Solid Earth*, 92(B9):9083–9100.

Kamb, B., Raymond, C., Harrison, W., Engelhardt, H., Echelmeyer, K., Humphrey, N., Brugman, M., and Pfeffer, T. (1985). Glacier surge mechanism: 1982-1983 surge of variegated glacier, alaska. *Science*, 227(4686):469–479.

Khazendar, A., Fenty, I. G., Carroll, D., Gardner, A., Lee, C. M., Fukumori, I., Wang, O., Zhang, H., Seroussi, H., Moller, D., et al. (2019). Interruption of two decades of Jakobshavn Isbrae acceleration and thinning as regional ocean cools. *Nature Geoscience*, 12(4):277–283.

Kienholz, C., Amundson, J. M., Motyka, R. J., Jackson, R. H., Mickett, J. B., Sutherland, D. A., Nash, J. D., Winters, D. S., Dryer, W. P., and Truffer, M. (2019). Tracking icebergs with time-lapse photography and sparse optical flow, LeConte Bay, Alaska, 2016-2017. *Journal of Glaciology*, 65:195–211.

Knudsen, M. (1900). Ein hydrographischer lehrsatz. *Annalen der Hydrographie und Maritimen Meteorologie*, 28(7):316–320.

Koziol, C. P. and Arnold, N. (2017). Incorporating modelled subglacial hydrology into inversions for basal drag. *The Cryosphere*, 11(6):2783–2797.

Kyrke-Smith, T. and Fowler, A. C. (2014). Subglacial swamps. *Proceedings of the Royal Society A: Mathematical, Physical and Engineering Sciences*, 470(2171):20140340.

Kyrke-Smith, T., Katz, R., and Fowler, A. (2014). Subglacial hydrology and the formation of ice streams. *Proceedings of the Royal Society A: Mathematical, Physical and Engineering Sciences*, 470(2161):20130494.

Large, W. G., McWilliams, J. C., and Doney, S. C. (1994). Oceanic vertical mixing: A review and a model with a nonlocal boundary layer parameterization. *Reviews of Geophysics*, 32(4):363–403.

Le Brocq, A. M., Payne, A., Siegert, M., and Alley, R. (2009). A subglacial water-flow model for west antarctica. *Journal of Glaciology*, 55(193):879–888.

Le Brocq, A. M., Ross, N., Griggs, J. A., Bingham, R. G., Corr, H. F., Ferraccioli, F., Jenkins, A., Jordan, T. A., Payne, A. J., Rippin, D. M., et al. (2013). Evidence from ice shelves for channelized meltwater flow beneath the antarctic ice sheet. *Nature Geoscience*, 6(11):945–948.

Leguy, G., Asay-Davis, X., and Lipscomb, W. (2014). Parameterization of basal friction near grounding lines in a one-dimensional ice sheet model. *The Cryosphere*, 8(4):1239–1259.

Livingstone, S., Clark, C., Woodward, J., and Kingslake, J. (2013). Potential subglacial lakes and meltwater drainage pathways beneath the antarctic and greenland ice sheets. *The Cryosphere*, 7:1721–1740.

Lorenz, M., Klingbeil, K., MacCready, P., and Burchard, H. (2019). Numerical issues of the Total Exchange Flow (TEF) analysis framework for quantifying estuarine circulation. *Ocean Science*, 15:601–614.

Luckman, A., Benn, D. I., Cottier, F., Bevan, S., Nilsen, F., and Inall, M. (2015). Calving rates at tidewater glaciers vary strongly with ocean temperature. *Nature Communications*, 6(1):1–7.

MacCready, P. (2011). Calculating estuarine exchange flow using isohaline coordinates. *Journal of Physical Oceanography*, 41:1116–1124.

MacCready, P., Geyer, W. R., and Burchard, H. (2018). Estuarine exchange flow is related to mixing through the salinity variance budget. *Journal of Physical Oceanography*, 48:1375–1384.

MacCready, P., McCabe, R. M., Siedlecki, S. A., Lorenz, M., Giddings, S. N., Bos, J., Albertson, S., Banas, N. S., and Garnier, S. (2021). Estuarine Circulation, Mixing, and Residence Times in the Salish Sea. *Journal of Geophysical Research: Oceans*, 126.

Magnusson, E., Rott, H., Bjornsson, H., and Palsson, F. (2007). The impact of jokulhlaups on basal sliding observed by sar interferometry on vatnajokull, iceland. *Journal of Glaciology*, 53:232–240.

Magorrian, S. J. and Wells, A. J. (2016). Turbulent plumes from a glacier terminus melting in a stratified ocean. *Journal of Geophysical Research: Oceans*, 121(7):4670–4696.

Marsh, O. J., Fricker, H. A., Siegfried, M. R., Christianson, K., Nicholls, K. W., Corr, H. F., and Catania, G. (2016). High basal melting forming a channel at the grounding line of ross ice shelf, antarctica. *Geophysical Research Letters*, 43(1):250–255.

Marshall, J., Adcroft, A., Hill, C., Perelman, L., and Heisey, C. (1997). A finite-volume, incompressible Navier Stokes model for studies of the ocean on parallel computers. *Journal of Geophysical Research C: Oceans*, 102:5753–5766.

Martos, Y. M., Catalán, M., Jordan, T. A., Golynsky, A., Golynsky, D., Eagles, G., and Vaughan, D. G. (2017). Heat Flux Distribution of Antarctica Unveiled. *Geophysical Research Letters*, 44(22):11,417–11,426.

Masson-Delmotte, V., Zhai, P., Pirani, A., Connors, S. L., Péan, C., Berger, S., Caud, N., Chen, Y., Goldfarb, L., Gomis, M., et al. (2021). Climate change 2021: the physical science basis. *Contribution of working group I to the sixth assessment report of the intergovernmental panel on climate change*, 2.

Matthews, J. (1981). The seasonal circulation of the Glacier Bay, Alaska fjord system. *Estuarine, Coastal and Shelf Science*, 12(6):679–700.

McDougall, T. and Barker, P. (2011). Getting started with TEOS-10 and the Gibbs Seawater (GSW) Oceanographic Toolbox.

McNabb, R. W., Hock, R., and Huss, M. (2015). Variations in Alaska tidewater glacier frontal ablation, 1985–2013. *Journal of Geophysical Research: Earth Surface*, 120(1):120–136.

Meierbachtol, T., Harper, J., and Humphrey, N. (2013). Basal drainage system response to increasing surface melt on the greenland ice sheet. *Science*, 341(6147):777–779.

Milillo, P., Rignot, E., Rizzoli, P., Scheuchl, B., Mouginot, J., Bueso-Bello, J., and Prats-Iraola, P. (2019). Heterogeneous retreat and ice melt of thwaites glacier, west antarctica. *Science Advances*, 5:eaau3433.

Moffat, C. (2014). Wind-driven modulation of warm water supply to a proglacial fjord, Jorge Montt Glacier, Patagonia. *Geophysical Research Letters*, 41(11):3943–3950.

Moffat, C., Tapia, F. J., Nittrouer, C. A., Hallet, B., Bown, F., Boldt Love, K., and Iturra, C. (2018). Seasonal evolution of ocean heat supply and freshwater discharge from a rapidly retreating tidewater glacier: Jorge Montt, Patagonia. *Journal of Geophysical Research: Oceans*, 123(6):4200–4223.

Mojica, J. F., Djoumna, G., Holland, D. M., and Holland, D. (2021). Interannual summer mixing processes in the ilulissat icefjord, greenland. *Journal of Marine Systems*, 214:103476.

Moon, T., Sutherland, D. A., Carroll, D., Felikson, D., Kehrl, L., and Straneo, F. (2018). Subsurface iceberg melt key to Greenland fjord freshwater budget. *Nature Geoscience*, 11:49–54.

Morlighem, M., Rignot, E., Binder, T., Blankenship, D., Drews, R., Eagles, G., Eisen, O., Ferraccioli, F., Forsberg, R., Fretwell, P., Goel, V., Greenbaum, J. S., Gudmundsson, H., Guo, J., Helm, V., Hofstede, C., Howat, I., Humbert, A., Jokat, W., Karlsson, N. B., Lee, W. S., Matsuoka, K., Millan, R., Mouginot, J., Paden, J., Pattyn, F., Roberts, J., Rosier, S., Ruppel, A., Seroussi, H., Smith, E. C., Steinhage, D., Sun, B., den Broeke, M. R., Ommen, T. D., van Wessem, M., and Young, D. A. (2020). Deep glacial troughs and stabilizing ridges unveiled beneath the margins of the Antarctic ice sheet. *Nature Geoscience*, 13(2):132–137.

Morlighem, M., Williams, C. N., Rignot, E., An, L., Arndt, J. E., Bamber, J. L., Catania, G., Chauché, N., Dowdeswell, J. A., Dorschel, B., et al. (2017). Bedmachine v3: Complete bed topography and ocean bathymetry mapping of greenland from multibeam echo sounding combined with mass conservation. *Geophysical research letters*, 44(21):11–051.

Mortensen, J., Bendtsen, J., Lennert, K., and Rysgaard, S. (2014). Seasonal variability of the circulation system in a west greenland tidewater outlet glacier fjord, godthåbsfjord (64 n). *Journal of Geophysical Research: Earth Surface*, 119(12):2591–2603.

Mortensen, J., Bendtsen, J., Motyka, R. J., Lennert, K., Truffer, M., Fahnestock, M., and Rysgaard, S. (2013). On the seasonal freshwater stratification in the proximity of fast-flowing tidewater outlet glaciers in a sub-arctic sill fjord. *Journal of Geophysical Research: Oceans*, 118:1382–1395.

Mortensen, J., Lennert, K., Bendtsen, J., and Rysgaard, S. (2011). Heat sources for glacial melt in a sub-Arctic fjord (Godthåbsfjord) in contact with the Greenland Ice Sheet. *Journal of Geophysical Research: Oceans*, 116.

Motyka, R. J., Dryer, W. P., Amundson, J., Truffer, M., and Fahnestock, M. (2013). Rapid submarine melting driven by subglacial discharge, LeConte Glacier, Alaska. *Geophysical Research Letters*, 40:5153–5158.

Motyka, R. J., Hunter, L., Echelmeyer, K. A., and Connor, C. (2003). Submarine melting at the terminus of a temperate tidewater glacier, LeConte Glacier, Alaska, USA. *Annals of Glaciology*, 36:57–65.

Motyka, R. J., Truffer, M., Fahnestock, M., Mortensen, J., Rysgaard, S., and Howat, I. (2011). Submarine melting of the 1985 Jakobshavn Isbræ floating tongue and the triggering of the current retreat. *Journal of Geophysical Research: Earth Surface*, 116(F1).

Mouginot, J., Rignot, E., Bjørk, A. A., Van den Broeke, M., Millan, R., Morlighem, M., Noël, B., Scheuchl, B., and Wood, M. (2019). Forty-six years of greenland ice sheet mass balance from 1972 to 2018. *Proceedings of the national academy of sciences*, 116(19):9239–9244.

Mouginot, J., Rignot, E., and Scheuchl, B. (2014). Sustained increase in ice discharge from the amundsen sea embayment, west antarctica, from 1973 to 2013. *Geophysical Research Letters*, 41:1576–1584.

Muench, R. and Heggie, D. (1978). Deep water exchange in Alaskan subarctic fjords. In Kjerfve, B., editor, *Estuarine Transport Processes*, pages 239–267. University of South Carolina Press, Columbia, South Carolina.

Murray, T. and Clarke, G. K. (1995). Black-box modeling of the subglacial water system. *Journal of Geophysical Research: Solid Earth*, 100(B6):10231–10245.

Murray, T., Scharrer, K., James, T., Dye, S., Hanna, E., Booth, A., Selmes, N., Luckman, A., Hughes, A., Cook, S., et al. (2010). Ocean regulation hypothesis for glacier dynamics in southeast Greenland and implications for ice sheet mass changes. *Journal of Geophysical Research: Earth Surface*, 115(F3).

Muto, A., Alley, R. B., Parizek, B. R., and Anandakrishnan, S. (2019a). Bed-type variability and till (dis)continuity beneath thwaites glacier, west antarctica. *Annals of Glaciology*, pages 1–9.

Muto, A., Anandakrishnan, S., Alley, R. B., Horgan, H. J., Parizek, B. R., Koellner, S., Christianson, K., and Holschuh, N. (2019b). Relating bed character and subglacial morphology using seismic data from thwaites glacier, west antarctica. *Earth and Planetary Science Letters*, 507:199–206.

Nakayama, Y., Cai, C., and Seroussi, H. (2021). Impact of subglacial freshwater discharge on pine island ice shelf. *Geophysical Research Letters*.

Nakayama, Y., Manucharyan, G., Zhang, H., Dutrieux, P., Torres, H. S., Klein, P., Seroussi, H., Schodlok, M., Rignot, E., and Menemenlis, D. (2019). Pathways of ocean heat towards pine island and thwaites grounding lines. *Scientific reports*, 9(1):1–9.

Nias, I., Cornford, S., and Payne, A. (2018). New mass-conserving bedrock topography for pine island glacier impacts simulated decadal rates of mass loss. *Geophysical Research Letters*, 45(7):3173–3181.

Nick, F. M., Vieli, A., Howat, I. M., and Joughin, I. (2009). Large-scale changes in Greenland outlet glacier dynamics triggered at the terminus. *Nature Geoscience*, 2(2):110–114.

Nowicki, S. M., Payne, A., Larour, E., Seroussi, H., Goelzer, H., Lipscomb, W., Gregory, J., Abe-Ouchi, A., and Shepherd, A. (2016). Ice sheet model intercomparison project (ismip6) contribution to cmip6. *Geoscientific model development*, 9(12):4521–4545.

Nye, J. F. (1976). Water flow in glaciers: Jökulhlaups, tunnels and veins. *Journal of Glaciology*, 17(76):181–207.

O'Neel, S., Echelmeyer, K., and Motyka, R. (2001). Short-term flow dynamics of a retreating tidewater glacier: LeConte Glacier, Alaska, USA. *Journal of Glaciology*, 47(159):567–578.

Perego, M., Price, S., and Stadler, G. (2014). Optimal initial conditions for coupling ice sheet models to Earth system models. *Journal of Geophysical Research Earth Surface*, 119:1–24.

Pritchard, H. D., Arthern, R. J., Vaughan, D. G., and Edwards, L. A. (2009). Extensive dynamic thinning on the margins of the greenland and antarctic ice sheets. *Nature*, 461(7266):971–975.

Rada, C. and Schoof, C. (2018). Subglacial drainage characterization from eight years of continuous borehole data on a small glacier in the yukon territory , canada. *The Cryosphere*, pages 1–42.

Rignot, E., Mouginot, J., Morlighem, M., Seroussi, H., and Scheuchl, B. (2014). Widespread, rapid grounding line retreat of pine island, thwaites, smith, and kohler glaciers, west antarctica, from 1992 to 2011. *Geophysical Research Letters*, 41:3502–3509.

Rignot, E., Mouginot, J., Scheuchl, B., Van Den Broeke, M., Van Wessem, M. J., and Morlighem, M. (2019). Four decades of antarctic ice sheet mass balance from 1979–2017. *Proceedings of the National Academy of Sciences*, 116(4):1095–1103.

Rignot, E., Velicogna, I., van den Broeke, M. R., Monaghan, A., and Lenaerts, J. (2011). Acceleration of the contribution of the greenland and antarctic ice sheets to sea level rise. *Geophysical Research Letters*, 38(5).

Rignot, E., Xu, Y., Menemenlis, D., Mouginot, J., Scheuchl, B., Li, X., Morlighem, M., Seroussi, H., den Broeke, M. v., Fenty, I., et al. (2016). Modeling of ocean-induced ice melt rates of five west greenland glaciers over the past two decades. *Geophysical Research Letters*, 43(12):6374–6382.

Röthlisberger, H. (1972). Water pressure in intra-and subglacial channels. *Journal of Glaciology*, 11(62):177–203.

Sanchez, R., Straneo, F., and Slater, D. (2022). Seasonal top-down stratification of a west greenland fjord by ice sheet meltwater.

Sanford, L. P., Boicourt, W. C., and Rives, S. R. (1992). Model for estimating tidal flushing of small embayments. *Journal of Waterway, Port, Coastal, and Ocean Engineering*, 118(6):635–654.

Schaffer, J., Kanzow, T., von Appen, W.-J., von Albedyll, L., Arndt, J. E., and Roberts, D. H. (2020). Bathymetry constrains ocean heat supply to Greenland's largest glacier tongue. *Nature Geoscience*, 13(3):227–231.

Schild, K. M., Sutherland, D. A., Elosegui, P., and Duncan, D. (2021). Measurements of iceberg melt rates using high-resolution gps and iceberg surface scans. *Geophysical Research Letters*, 48.

Schoof, C. (2005). The effect of cavitation on glacier sliding. *Proceedings of the Royal Society A: Mathematical, Physical and Engineering Sciences*, 461(2055):609–627.

Schoof, C. (2010). Ice-sheet acceleration driven by melt supply variability. *Nature*, 468:803–806.

Schoof, C., Hewitt, I. J., and Werder, M. A. (2012). Flotation and free surface flow in a model for subglacial drainage. part 1. distributed drainage. *Journal of Fluid Mechanics*, 702:126–156.

Schroeder, D. M., Blankenship, D. D., Raney, R. K., and Grima, C. (2015). Estimating subglacial water geometry using radar bed echo specularity: application to thwaites glacier, west antarctica. *IEEE Geoscience and Remote Sensing Letters*, 12(3):443–447.

Schroeder, D. M., Blankenship, D. D., and Young, D. A. (2013). Evidence for a water system transition beneath thwaites glacier, west antarctica. *Proceedings of the National Academy of Sciences of the United States of America*, 110:12225–8.

Sciascia, R., Straneo, F., Cenedese, C., and Heimbach, P. (2013). Seasonal variability of submarine melt rate and circulation in an East Greenland fjord. *Journal of Geophysical Research: Oceans*, 118(5):2492–2506.

Seo, K.-W., Wilson, C. R., Scambos, T., Kim, B.-M., Waliser, D. E., Tian, B., Kim, B.-H., and Eom, J. (2015). Surface mass balance contributions to acceleration of antarctic ice mass loss during 2003–2013. *Journal of Geophysical Research: Solid Earth*, 120(5):3617–3627.

Seroussi, H., Nakayama, Y., Larour, E., Menemenlis, D., Morlighem, M., Rignot, E., and Khazendar, A. (2017). Continued retreat of thwaites glacier, west antarctica, controlled by bed topography and ocean circulation. *Geophysical Research Letters*, pages 1–9.

Seroussi, H., Nowicki, S., Payne, A. J., Goelzer, H., Lipscomb, W. H., Abe-Ouchi, A., Agosta, C., Albrecht, T., Asay-Davis, X., Barthel, A., et al. (2020). Ismip6 antarctica: a multi-model ensemble of the antarctic ice sheet evolution over the 21st century. *The Cryosphere*, 14(9):3033–3070.

Shankar, S., Stearns, L., Bray, I., and van der Veen, C. (2021). Iceberg distributions along greenland fjords, 2017-2020.

Slater, D., Nienow, P., Cowton, T., Goldberg, D., and Sole, A. (2015). Effect of near-terminus subglacial hydrology on tidewater glacier submarine melt rates. *Geophysical Research Letters*, 42(8):2861–2868.

Slater, D. and Straneo, F. (2022). Submarine melting of glaciers in greenland amplified by atmospheric warming. *Nature Geoscience*, pages 1–6.

Slater, D., Straneo, F., Das, S., Richards, C., Wagner, T., and Nienow, P. (2018). Localized plumes drive front-wide ocean melting of a Greenlandic tidewater glacier. *Geophysical Research Letters*, 45(22):12–350.

Slater, D. A., Felikson, D., Straneo, F., Goelzer, H., Little, C. M., Morlighem, M., Fettweis, X., and Nowicki, S. (2020). Twenty-first century ocean forcing of the Greenland ice sheet for modelling of sea level contribution. *Cryosphere*, 14:985–1008.

Slater, D. A., Straneo, F., Felikson, D., Little, C. M., Goelzer, H., Fettweis, X., and Holte, J. (2019). Estimating greenland tidewater glacier retreat driven by submarine melting. *The Cryosphere*, 13(9):2489–2509.

Smagorinsky, J. (1963). General Circulation experiments with the primitive equations: I. The basic experiment. *Monthly Weather Review*, 91(3):99 – 164.

Smith, B., Fricker, H. A., Gardner, A. S., Medley, B., Nilsson, J., Paolo, F. S., Holschuh, N., Adusumilli, S., Brunt, K., Csatho, B., et al. (2020). Pervasive ice sheet mass loss reflects competing ocean and atmosphere processes. *Science*, 368(6496):1239–1242.

Smith, B. E., Gourmelen, N., Huth, A., and Joughin, I. (2017). Connected subglacial lake drainage beneath thwaites glacier, west antarctica. *The Cryosphere*, 11:451–467.

Stearns, L. A., Smith, B. E., and Hamilton, G. S. (2008). Increased flow speed on a large east antarctic outlet glacier caused by subglacial floods. *Nature Geoscience*, 1(12):827–831.

Stigebrandt, A. (1977). On the effect of barotropic current fluctuations on the two-layer transport capacity of a constriction. *Journal of Physical Oceanography*, 7(1):118–122.

Stigebrandt, A. (1981). A mechanism governing the estuarine circulation in deep, strongly stratified fjords. *Estuarine, Coastal and Shelf Science*, 13(2):197–211.

Stommel, H. and Farmer, H. G. (1953). Control of salinity in an estuary by a transition. *Journal of Marine Research*, 12(1):13–20.

Straneo, F. and Cenedese, C. (2015). The dynamics of Greenland's glacial fjords and their role in climate. *Annual Review of Marine Science*, 7:89–112.

Straneo, F., Curry, R. G., Sutherland, D. A., Hamilton, G. S., Cenedese, C., Våge, K., and Stearns, L. A. (2011). Impact of fjord dynamics and glacial runoff on the circulation near Helheim Glacier. *Nature Geoscience*, 4:322–327.

Straneo, F. and Heimbach, P. (2013). North Atlantic warming and the retreat of Greenland's outlet glaciers. *Nature*, 504(7478):36–43.

Straneo, F., Sutherland, D. A., Holland, D., Gladish, C., Hamilton, G. S., Johnson, H. L., Rignot, E., Xu, Y., and Koppes, M. (2012). Characteristics of ocean waters reaching greenland's glaciers. *Annals of Glaciology*, 53(60):202–210.

Sulak, D. J., Sutherland, D. A., Enderlin, E. M., Stearns, L. A., and Hamilton, G. S. (2017). Iceberg properties and distributions in three Greenlandic fjords using satellite imagery. *Annals of Glaciology*, 58:92–106.

Sutherland, D., Jackson, R. H., Kienholz, C., Amundson, J. M., Dryer, W., Duncan, D., Eidam, E., Motyka, R., and Nash, J. (2019). Direct observations of submarine melt and subsurface geometry at a tidewater glacier. *Science*, 365(6451):369–374.

The IMBIE Team (2019). Mass balance of the greenland ice sheet from 1992 to 2018. *Nature*, 579(7798):233–239.

Van den Broeke, M. R., Enderlin, E. M., Howat, I. M., Kuipers Munneke, P., Noël, B. P., Van De Berg, W. J., Van Meijgaard, E., and Wouters, B. (2016). On the recent contribution of the greenland ice sheet to sea level change. *The Cryosphere*, 10(5):1933–1946.

Velicogna, I., Sutterley, T. C., and van den Broeke, M. R. (2014). Regional acceleration in ice mass loss from greenland and antarctica using grace time-variable gravity data. *Geophysical Research Letters*, 41(22):8130–8137.

Walder, J. S. (1986). Hydraulics of subglacial cavities. *Journal of Glaciology*, 32(112):439–445.

Walder, J. S. and Fowler, A. (1994). Channelized subglacial drainage over a deformable bed. *Journal of glaciology*, 40(134):3–15.

Walters, R. A., Josberger, E. G., and Driedger, C. L. (1988). Columbia Bay, Alaska: an 'Upside Down' Estuary. *Estuarine, Coastal and Shelf Science*, 26:607–617.

Watanabe, M., Suzuki, T., O'ishi, R., Komuro, Y., Watanabe, S., Emori, S., Takemura, T., Chikira, M., Ogura, T., Sekiguchi, M., et al. (2010). Improved climate simulation by miroc5: mean states, variability, and climate sensitivity. *Journal of Climate*, 23(23):6312–6335.

Weertman, J. (1972). General theory of water flow at the base of a glacier or ice sheet. *Reviews of Geophysics*, 10(1):287–333.

Wei, W., Blankenship, D. D., Greenbaum, J. S., Gourmelen, N., Dow, C. F., Richter, T. G., Greene, C. A., Young, D. A., Lee, S.-H., Kim, T.-W., Lee, W. S., Wåhlin, A., and Assmann, K. M. (2020). Getz ice shelf melt enhanced by freshwater discharge from beneath the west antarctic ice sheet. *The Cryosphere Discussions*, pages 1–16.

Werder, M. A. (2016). The hydrology of subglacial overdeepenings: A new supercooling threshold formula. *Geophysical Research Letters*, 43:2045–2052.

Werder, M. A. and Funk, M. (2009). Dye tracing a jokulhlaup: Ii. testing a jokulhlaup model against flow speeds inferred from measurements. *J. Glaciol.*, 55(193):899–908.

Werder, M. A., Hewitt, I. J., Schoof, C. G., and Flowers, G. E. (2013). Modeling channelized and distributed subglacial drainage in two dimensions. *Journal of Geophysical Research: Earth Surface*, 118.

Wood, M., Rignot, E., Fenty, I., Menemenlis, D., Millan, R., Morlighem, M., Mouginot, J., and Seroussi, H. (2018). Ocean-induced melt triggers glacier retreat in Northwest Greenland. *Geophysical Research Letters*, 45(16):8334–8342.

Xu, Y., Rignot, E., Menemenlis, D., and Koppes, M. (2012). Numerical experiments on subaqueous melting of Greenland tidewater glaciers in response to ocean warming and enhanced subglacial discharge. *Annals of Glaciology*, 53(60):229–234.

Young, D., Roberts, J. L., Ritz, C., Frezzotti, M., Quartini, E., Cavitte, M. G., Tozer, C. R., Steinhage, D., Urbini, S., Corr, H. F., et al. (2017). High-resolution boundary conditions of an old ice target near dome c, antarctica. *The Cryosphere*.

Young, D., Schroeder, D., Blankenship, D., Kempf, S. D., and Quartini, E. (2016). The distribution of basal water between antarctic subglacial lakes from radar sounding. *Philosophical Transactions of the Royal Society A: Mathematical, Physical and Engineering Sciences*, 374(2059):20140297.

Yu, H., Rignot, E., Seroussi, H., and Morlighem, M. (2018). Retreat of thwaites glacier, west antarctica, over the next 100 years using various ice flow models, ice shelf melt scenarios and basal friction laws. *The Cryosphere*, 12:3861–3876.

Zhao, K. X., Stewart, A. L., and McWilliams, J. C. (2021). Geometric constraints on glacial fjord–shelf exchange. *Journal of Physical Oceanography*, 51(4):1223–1246.